

AN ABSTRACT OF THE DISSERTATION OF

Xianfei Wen for the degree of Doctor of Philosophy in Nuclear Engineering presented on March 2, 2016.

Title: An Active Interrogation Technique Based on Photofission for Non-destructive Assay of Used Nuclear Fuel.

Abstract approved:

Haori Yang

High-energy delayed γ -rays from photofission were demonstrated to be signatures for detection and identification of special nuclear materials. Such γ -rays were measured in between linac pulses using independent data acquisition systems. A list-mode system was developed to measure low-energy delayed γ -rays after irradiation. Photofission product yields of ^{238}U and ^{239}Pu were determined based on the measured delayed γ -ray spectra. The differential yields of delayed γ -rays were also proven to be able to discriminate nuclear and non-nuclear materials. The measurement outcomes were compared with Monte Carlo simulation results. It was demonstrated that the current available code has capabilities and limitations in the simulation of photofission process.

A two-fold approach was used to address the high-rate challenge in used nuclear fuel assay based on photofission technique. First, a standard HPGe preamplifier was modified

to improve its capabilities in high-rate pulsed photofission environment. Second, advanced pulse processing algorithms including template-matching and de-randomization methods were shown to greatly improve throughput rate without large sacrifice in energy resolution at ultra-high input count rate.

©Copyright by Xianfei Wen
March 2, 2016
All Rights Reserved

An Active Interrogation Technique Based on Photofission for Non-destructive Assay of
Used Nuclear Fuel

by
Xianfei Wen

A DISSERTATION

submitted to

Oregon State University

in partial fulfillment of
the requirements for the
degree of

Doctor of Philosophy

Presented March 2, 2016
Commencement June 2016

Doctor of Philosophy dissertation of Xianfei Wen presented on March 2, 2016.

APPROVED:

Major Professor, representing Nuclear Engineering

Head of the School of Nuclear Science and Engineering

Dean of the Graduate School

I understand that my dissertation will become part of the permanent collection of Oregon State University libraries. My signature below authorizes release of my dissertation to any reader upon request.

Xianfei Wen, Author

ACKNOWLEDGEMENTS

My graduate study over the past four years has been an intense, challenging, and rewarding journey. The time I spent at Oregon State University was truly unforgettable. Here I would like to thank all people who helped me go through it.

First and foremost, I would like to thank my advisor, Dr. Haori Yang, for his mentorship, support, and encouragement throughout the course of my study. Through working on the photofission project under his advising, I have gained strong experience in radiation detection and measurement, nuclear instrumentation, digital pulse processing, and Monte Carlo simulation. For example, I had much more understanding on advanced pulse processing algorithms for high-resolution high-throughput gamma spectroscopy systems after he introduced me to the high-rate challenges. His door was always open for me to discuss any problems encountered in research projects. His insight about photofission techniques for used nuclear fuel assay provided invaluable guidance for my research work. This also brought me to an exciting field, nuclear safeguards. Without his advice or support, my dissertation work could not be possible. I feel so fortunate to have Dr. Yang as my advisor and cannot appreciate more for what he has done for me.

I also would like to thank Dr. Alan Hunt from Idaho Accelerator Center for providing the script to analyze the data measured using the FAST ComTec list-mode system. Thanks are also given to Dr. Paul Scoullar from Southern Innovation for sharing with me the high-rate SDD data and discussing the model-based pulse processing algorithm. I also

want to express my gratitude to Dr. David Hamby, Dr. Abi Farsoni, Dr. Steven Reese, and Dr. Burkan Isgor for serving on my committee.

Finally, I would like to appreciate the support from my parents. They make what I have done more meaningful.

CONTRIBUTION OF AUTHORS

For the second paper, John Kavouras assisted with data collection. Dante Nakazawa was involved in experimental design. As to the third paper, Dante Nakazawa contributed to LTSpice simulation. Mat Kastner and Jason Pavlick helped move the feedback resistor and capacitor to warm side to make modifications feasible in practice.

TABLE OF CONTENTS

	<u>Page</u>
1 General Introduction	1
1.1 Passive and Active Non-destructive Techniques	2
1.2 Challenges in the Photofission Techniques.....	5
1.2.1 Photofission Product Yields	5
1.2.2 Monte Carlo Simulation of Photofission Process.....	6
1.2.3 High-rate in Pulsed Photofission Environment	12
2 First Manuscript.....	22
2.1 Introduction	23
2.2 Experimental Setup	27
2.3 Results and Discussion.....	30
2.3.1 Photofission Product Yields of ^{238}U Measured in between Linac Pulses.....	30
2.3.2 Photofission Product Yields of ^{239}Pu and ^{238}U Measured after Irradiation	34
2.4 Conclusions and Future Work.....	39
3 Second Manuscript.....	43
3.1 Introduction	45
3.2 Experimental Setup	48
3.3 Description of the MCNPX Simulation	54
3.4 Results and Discussion.....	57
3.4.1 Differential Yields of Delayed γ -rays.....	57
3.4.2 Delayed Fission γ -rays Energy Spectra	60

TABLE OF CONTENTS (Continued)

	<u>Page</u>
3.5 Conclusion.....	66
4 Third Manuscript	71
4.1 Introduction	74
4.2 Modifications to the Preamplifier	77
4.2.1 Modification to the Feedback Resistor.....	79
4.2.2 Modification to the Tail Time	82
4.3 Evaluation of Energy Resolution after the Modifications.....	85
4.4 Conclusions	89
5 Fourth Manuscript.....	93
5.1 Introduction	95
5.2 Discussion of the Algorithm	96
5.3 Results and Discussion.....	98
5.3.1 Implementation on Signals from a NaI Detector.....	98
5.3.2 Implementation on Signals from a Silicon Drift Detector.....	100
5.3.3 Implementation on Signals from a HPGe Detector	103
5.4 Conclusion.....	106
6 General Conclusion.....	110
Bibliography	113
Appendices.....	120
A MCNPX Simulation of Delayed γ -rays from Photofission.....	120

TABLE OF CONTENTS (Continued)

	<u>Page</u>
B De-randomization Technique	135
C Monte Carlo Simulation Codes	146
D Publications and Presentations	152

LIST OF FIGURES

<u>Figure</u>	<u>Page</u>
Figure 1.1 Principal γ -ray signatures of nuclear materials of interest [14].....	3
Figure 1.2 Natural uranium measurement (top) and MCNP6.1 simulation (bottom), 0.1-0.8 MeV [26].....	7
Figure 1.3 Examples of tally tagging in MCNPX 2.7.0 [28].....	11
Figure 1.4 Illustration of the Kalman filtering (prediction and correction).....	16
Figure 1.5 Trapezoidal filtering using different rise times (ICR=300 kcps).	18
Figure 1.6 Energy spectra reconstructed using the traditional and time-variant trapezoidal filtering methods at input count rate of 1.03×10^6 cps [1].	18
Figure 2.1 A picture of the experimental setup for the measurement of delayed γ -rays from photofission. (b) Schematic drawing of the experimental setup.	28
Figure 2.2 The uranium and plutonium samples used in the photofission experiments...	29
Figure 2.3 (a) Measurement of delayed γ -rays from photofission of ^{238}U in between linac pulses; (b) Measurement of delayed γ -rays from photofission of ^{238}U and ^{239}Pu after irradiation.	31
Figure 2.4 Measured high-energy delayed γ -rays from photofission of ^{238}U (3.9-4.5 MeV).	32
Figure 2.5 Measured delayed γ -rays from photofission of ^{239}Pu using the list-mode system (0.9-1.5 MeV).	36
Figure 3.1 (a) A picture of the experimental setup. The left detector assembly is completed, the right one is partially disassembled showing the lead shielding inside. (b) A drawing of the experimental setup.....	50
Figure 3.2 The block diagrams of the three data-acquisition systems (a. FAST ComTec list mode system; b. Customized system; c. Canberra LYNX multi-channel analyzer)...	51
Figure 3.3 Signals from the HPGe detector; the original, fast-, and slow-channel signals are shown.	53

LIST OF FIGURES (Continued)

<u>Figure</u>	<u>Page</u>
Figure 3.4 Comparison of measured spectra using the customized spectroscopy system (dots) and the commercial MCA (solid line).	53
Figure 3.5 The model of the MCNPX simulation.....	55
Figure 3.6 Illustration of the threshold line selection. The time width for each sample point is 10 ns.	58
Figure 3.7 The differential yields of delayed γ -rays for DU, ^{232}Th , and lead.....	59
Figure 3.8 Simulated differential yields of delayed γ -rays from the DU, ^{232}Th , and lead samples.....	60
Figure 3.9 The output signal from an HPGe detector between two successive pulses.....	61
Figure 3.10 Time (>10ms) integrated delayed-fission γ -ray spectra from the DU sample measured with a Canberra LYNX system and a Fast ComTec list mode system.....	62
Figure 3.11 Time (>20ms) integrated delayed-fission γ -ray spectra from the ^{239}Pu sample measured with a Canberra LYNX system and a Fast ComTec list mode system.....	62
Figure 3.12 Time (>10ms) integrated delayed-fission γ -ray spectra from the ^{232}Th sample measured with a Fast ComTec list mode system and a customized spectroscopy system.	63
Figure 3.13 Time integrated delayed-fission γ -rays from various samples measured with a Fast ComTec list mode system (Note: data from the first 10 ms after each linac pulse was disregarded).....	64
Figure 3.14 Comparison of measured and simulated delayed-fission γ -ray spectra above 3 MeV for DU sample.....	65
Figure 3.15 Comparison of measured and simulated delayed-fission γ -ray spectra from 2.5 MeV to 3 MeV for DU sample.	66
Figure 4.1 Illustration of the components of a standard preamplifier to be modified.	78
Figure 4.2 A block diagram of the functionality of a typical RC-feedback commercial preamplifier unit.....	78

LIST OF FIGURES (Continued)

<u>Figure</u>	<u>Page</u>
Figure 4.3 A schematic drawing of a preamplifier with RC-feedback.	78
Figure 4.4 A schematic drawing of the experimental setup for testing of the effect of feedback resistor on saturation time.	80
Figure 4.5 Measured signals from the preamplifiers in the photofission environment. ...	81
Figure 4.6 Comparison between the simulated signals from the modified preamplifier with complete and incomplete P/Z cancellations.....	82
Figure 4.7 Comparison between signal waveforms measured with NI PXIe-5122.....	84
Figure 4.8 The effect of reduced tail time on baseline shift simulated in LTSpice.....	85
Figure 4.9 Illustration of the time and energy signal shaped in parallel in the trapezoidal filtering.....	87
Figure 4.10 Distribution of charge collection time at input count rate of 20 kcps.	88
Figure 4.11 Energy resolution versus rise time in the trapezoidal filtering (flat top time was fixed at 0.8 μ s).	88
Figure 4.12 Energy spectra reconstructed at optimal rise times (flat top time was fixed at 0.8 μ s).	89
Figure 5.1 The application of the template-matching algorithm to recover simulated piled-up pulses.	98
Figure 5.2 The anode output signal and the template.	99
Figure 5.3 Comparison between energy spectra measured with a Canberra Lynx system and reconstructed with the template-matching algorithm.....	100
Figure 5.4 Energy spectra at different Input Count Rates (ICR) with the template-matching algorithm.	102
Figure 5.5 Comparison between the template-matching algorithm and the trapezoidal filter (Output Count Rate vs Input Count Rate).....	102

LIST OF FIGURES (Continued)

<u>Figure</u>	<u>Page</u>
Figure 5.6 Comparison between the template-matching algorithm and the trapezoidal filter (FWHM vs Input Count Rate).....	103
Figure 5.7 Verification of the reconstructed signal from preamplifier.....	105
Figure 5.8 Energy spectra reconstructed with the template-matching algorithm.	105
Figure 6.1 Comparison between the measured delayed gamma spectra and simulated results (2.6-3.5 MeV, ^{238}U).	122
Figure 6.2 Comparison between the measured delayed gamma spectra and simulated results (3.5-5.0 MeV, ^{238}U).	123
Figure 6.3 Comparison between the delayed γ -ray spectra measured using the list-mode system and simulation results (0.6-0.9 MeV, ^{238}U).	124
Figure 6.4 Comparison between the delayed γ -ray spectra measured using the list-mode system and simulation results (0.9-1.2 MeV, ^{238}U).	125
Figure 6.5 Comparison between the delayed γ -ray spectra measured using the list-mode system and simulation results (1.2-1.5 MeV, ^{238}U).	125
Figure 6.6 Comparison between the delayed γ -ray spectra measured using the list-mode system and simulation results (1.5-1.8 MeV, ^{238}U).	126
Figure 6.7 Comparison between the delayed γ -ray spectra measured using the list-mode system and simulation results (1.8-2.1 MeV, ^{238}U).	126
Figure 6.8 Comparison between the delayed γ -ray spectra measured using the list-mode system and simulation results (2.1-2.6 MeV, ^{238}U).	127
Figure 6.9 Comparison between the delayed γ -ray spectra measured using the list-mode system and simulation results (2.6-3.1 MeV, ^{238}U).	127
Figure 6.10 Comparison between the delayed γ -ray spectra measured using the list-mode system and simulation results (3.1-3.6 MeV, ^{238}U).	128
Figure 6.11 Comparison between the delayed γ -ray spectra measured using the list-mode system and simulation results (3.6-4.5 MeV, ^{238}U).	128

LIST OF FIGURES (Continued)

<u>Figure</u>	<u>Page</u>
Figure 6.12 Comparison between the delayed γ -ray spectra measured using the list-mode system and simulation results (0.6-0.9 MeV, ^{239}Pu).....	129
Figure 6.13 Comparison between the delayed γ -ray spectra measured using the list-mode system and simulation results (0.9-1.2 MeV, ^{239}Pu).....	129
Figure 6.14 Comparison between the delayed γ -ray spectra measured using the list-mode system and simulation results (1.2-1.5 MeV, ^{239}Pu).....	130
Figure 6.15 Comparison between the delayed γ -ray spectra measured using the list-mode system and simulation results (1.5-1.8 MeV, ^{239}Pu).....	130
Figure 6.16 Comparison between the delayed γ -ray spectra measured using the list-mode system and simulation results (1.8-2.1 MeV, ^{239}Pu).....	131
Figure 6.17 Comparison between the delayed γ -ray spectra measured using the list-mode system and simulation results (2.1-2.7 MeV, ^{239}Pu).....	131
Figure 6.18 Comparison between the delayed γ -ray spectra published by P. Sibczynski et al. and simulation results (0.3-0.9 MeV, HEU).....	132
Figure 6.19 Comparison between the delayed γ -ray spectra published by P. Sibczynski et al. and simulation results (0.9-1.5 MeV, HEU).....	132
Figure 6.20 Comparison between the delayed γ -ray spectra published by P. Sibczynski et al. and simulation results (1.5-2.1 MeV, HEU).....	133
Figure 6.21 Comparison between the delayed γ -ray spectra published by P. Sibczynski et al. and simulation results (2.1-2.7 MeV, HEU).....	133
Figure 6.22 Comparison between the delayed γ -ray spectra published by P. Sibczynski et al. and simulation results (2.7-3.3 MeV, HEU).....	134
Figure 6.23 Comparison between the delayed γ -ray spectra published by P. Sibczynski et al. and simulation results (3.3-4.2 MeV, HEU).....	134
Figure 6.24 A block diagram of the functionality of a typical RC-feedback commercial preamplifier unit.....	136
Figure 6.25 A schematic drawing of a preamplifier with RC-feedback.....	136

LIST OF FIGURES (Continued)

<u>Figure</u>	<u>Page</u>
Figure 6.26 An equivalent presentation of the preamplifier.	136
Figure 6.27 The deconvolution of pulses from an HPGe preamplifier.....	138
Figure 6.28 Digital synthesis of exponential pulses from the detector current signals. .	140
Figure 6.29 Energy spectrum reconstructed using the algorithm based on the de-randomization method (ICR=100 kcps).....	145
Figure 6.30 Energy spectrum reconstructed using the de-randomization method (ICR=300 kcps).....	145

LIST OF TABLES

<u>Table</u>	<u>Page</u>
Table 2.1 Measured photofission product yields of ^{238}U based on high-energy delayed γ -rays.....	34
Table 2.2 Examples of calculated half-lives of nuclides produced in photofission reactions.	37
Table 2.3 Measured photofission product yields of ^{239}Pu using the list-mode system.	38
Table 2.4 Measured photofission product yields of ^{238}U using the list-mode system.	39
Table 3.1 Key parameters of PXIe-5122 digitizer.	52
Table 3.2 Key parameters of the EJ-339A liquid scintillator	54
Table 5.1 Comparison between the template-matching algorithm and the trapezoidal filter (HPGe data).....	106
Table 6.1 Efficiency corrected intensities relative to the 3287.6 keV peak.	123

1 General Introduction

In some scenarios, such as used nuclear fuel assay, it is quite challenging to use passive non-destructive techniques to identify and quantify nuclear materials. The reason is that the signals of interest are buried in large background dominated by long-lived fission products, such as ^{137}Cs [1]. Photofission based active non-destructive techniques are being actively investigated and have been identified as a promising approach to address the issues encountered in passive techniques [2-6]. The three major challenges existing in the photofission techniques for used nuclear fuel assay include: 1) Published data on photofission product yields of nuclides of interest (e.g. ^{232}Th , ^{235}U , ^{238}U , ^{239}Pu , ^{240}Pu) is scarce; 2) Although simulation of delayed γ -rays has been validated for neutron-induced fission, simulated delayed γ -rays from photofission haven't been compared with measurement results for code validation purpose; 3) The input γ -rays count rate could reach 1×10^6 or even higher counts per second (cps) after cooling for a few years and the measurement electronic systems could be completely saturated due to the large energy injection from the pulsed linac. How to perform high-resolution high-throughput spectroscopy measurement at such high input rate is challenging. In my work, the photofission product yields of ^{238}U and ^{239}Pu were determined based on high-resolution spectroscopy measurement of delayed γ -rays. The measured photofission product yields are presented in the first paper [7]. The measured delayed γ -ray energy spectra were also used to compare with Monte Carlo simulation results to demonstrate the capabilities and limitations of current package in the simulation of photofission process. The second paper presents the measured energy spectra and the

comparison between measurement outcome and simulation data [8]. Due to the high-rate challenge in the measurement of delayed γ -rays from photofission, modifications to a standard High-purity Germanium (HPGe) preamplifier and development of advanced pulse processing algorithms were investigated to improve the measurement sensitivity and accuracy. The third paper describes the work on the modifications [9]. The advanced pulse processing algorithm development is illustrated in the fourth paper [10]. In the following sections of this Chapter, passive and active non-destructive techniques in homeland security and nuclear safeguards are first introduced. Then the challenges identified above are described in detail. The papers are attached in Chapters 2-5. A general conclusion is made in Chapter 6.

1.1 Passive and Active Non-destructive Techniques

In nuclear safeguards applications, effective approaches to protect people and environment from the theft or diversion of nuclear materials and technologies that could be used to proliferate are in urgent need by International Atomic Energy Agency (IAEA). Non-destructive techniques to detect, identify, and quantify special nuclear materials are of great interest to both domestic and international nuclear safeguards communities [11-13]. They can be categorized into passive and active techniques. The passive techniques are based on detection and measurement of the radiation (e.g. γ -rays, neutron) naturally emitted from nuclear materials themselves. Figure 1.1 shows the principal γ -ray signatures of nuclear materials of interest [14]. However, the intensities of such spontaneous radiation are normally low and the energies of the γ -rays are also low. For

lightly shielded nuclear materials, the relative intensity of the 186 keV and 1001 keV peaks can be used to indicate HEU. When the nuclear materials are heavily shielded, identification of HEU cannot be made based on the relative intensity since most low-energy γ -rays will be absorbed or scattered by the shielding materials. Furthermore, in homeland security applications, it is prudent to assume that the nuclear materials are intentionally shielded to make the detection more challenging. Although the passive techniques are easy to implement and no interrogation source is required, accurate detection and quantification of heavily shielded nuclear materials based on passive techniques is almost impossible.

Isotope	Energy keV	Activity γ /g-s	Mean Free Path	
			High-Z, ρ	Low-Z, ρ
^{234}U	120.9	9.35×10^4	0.23	69
^{235}U	143.8	8.40×10^3	0.36	73
^{238}U	185.7	4.32×10^4	0.69	80
	766.4	2.57×10^1	10.0	139
^{238}Pu	1001.0	7.34×10^1	13.3	159
	152.7	5.90×10^6	0.40	75
^{239}Pu	766.4	1.387×10^5	9.5	139
	129.3	1.436×10^5	0.27	71
^{240}Pu	413.7	3.416×10^4	3.7	106
	45.2	3.80×10^6	0.07	25
	160.3	3.37×10^4	0.45	76
^{241}Pu	642.5	1.044×10^3	7.4	127
	148.6	7.15×10^6	0.37	74
	208.0	2.041×10^7	0.86	83
^{241}Am	59.5	4.54×10^{10}	0.14	38
	125.3	5.16×10^6	0.26	70

Figure 1.1 Principal γ -ray signatures of nuclear materials of interest [14].

Active interrogation techniques based on measurement of high-energy γ -rays or neutrons have been identified as an effective approach to address the issues encountered

in the passive techniques [6]. Both neutrons and high-energy photons can be used to induce fission reactions in the nuclear materials. There are four types of unique signatures following induced fission: prompt neutrons, prompt γ -rays, delayed neutrons, delayed γ -rays [15]. Each signature can serve as the basis for detection, identification, and quantification of nuclear materials. On average, there are two fission fragments produced in each fission reaction. Two to three prompt neutrons and approximately eight prompt γ -rays are emitted within 10^{-15} s from the time of fission. Since the fission products are usually generated in excited states and have excess neutrons, they will de-excite to stable states and produce another six to seven γ -rays and approximately 0.01 to 0.02 neutrons per fission in the de-excitation process. Although intensities of prompt signatures (prompt neutron, prompt γ -rays) are much stronger than the delayed signatures (delayed neutron, delayed γ -rays), most active interrogation techniques utilize the delayed signals to avoid large interference from the interrogation source. Delayed neutrons emitted by neutron-rich fission fragments are a well-established, reliable, and unique signature of nuclear materials [16-18]. However, they can be easily shielded by hydrogenous materials like water and their yield is fairly low. In addition to delayed neutrons, delayed γ -rays are emitted during the β -decay of the excited fission fragments. Measurements of delayed γ -rays have some advantages over the delayed neutron. First, the intensity of high-energy delayed γ -rays ($E_\gamma > 3$ MeV) is much stronger than that of delayed neutrons, which significantly improves the measurement sensitivity. Second, high-energy γ -rays are highly penetrating. They typically undergo 10-100 times less attenuation than delayed neutrons in hydrogenous materials. Third, energy spectrum of the high-energy delayed γ -

rays is unique for each nuclide. This feature can be potentially used to directly determine Pu content and isotope composition in used nuclear fuel.

1.2 Challenges in the Photofission Techniques

1.2.1 Photofission Product Yields

System design based on the active non-destructive techniques is largely dependent on nuclear data, such as fission product yields. Although yields for neutron-induced fission of most nuclear materials (e.g. ^{232}Th , ^{235}U , ^{238}U , ^{239}Pu) were well studied and have already been verified and available in various nuclear databases, such as the Evaluated Nuclear Data File (ENDF), published experimental results on photofission product yields are rare. This poses a great challenge in the application of photofission techniques to nuclear safeguards, such as used nuclear fuel assay. Non-exhaustive examples of the photofission yields measurement are listed here. Meason et al. reported photofission yields of ^{238}U using monoenergetic γ -rays [19]. The γ -rays (17.5 MeV) were produced through the $^7\text{Li} (p, \gamma) ^4\text{He}$ reaction. Low-level β counting techniques were used to determine the yields because the available γ -ray flux was rather low. Photofission yields of ^{235}U and ^{238}U were published by Jacobs et al. using 12-, 15-, 20-, 30-, and 70-MeV bremsstrahlung [20-21]. The photofission product mass distribution for the photofission of ^{235}U using bremsstrahlung with end-point energy ranging from 12 MeV to 70 MeV was shown to have a doubly peaked shape without fine structure. In their ^{238}U photofission studies, they observed a strong increase of the symmetric mass yield with

increasing bremsstrahlung energy and a near independence of the asymmetric mass yields on the excitation energy. Photofission yields of ^{238}U were also measured by Wehe et al. using 9-MeV bremsstrahlung [22]. The photon source was produced from x-ray radiography units for cargo inspection. The delayed γ -rays were measured using HPGe and NaI(Tl) detectors after probing a sample. Cumulative yields of some major photofission products (^{93}Sr , ^{132}Sb , $^{132\text{m}}\text{Sb}$, ^{89}Rb , ^{133}Sb) were reported. In their effort to characterize nuclear waste package using photon activation analysis techniques, several measurement campaigns were performed by a group from CEA to determine the yields of various photofission products to optimize system design. Results on photofission yields of ^{235}U and ^{238}U induced by 16.3-MeV or 19.4-MeV bremsstrahlung were recently published by Carrel et al. [23]. To the best of our knowledge, no published data concerning the photofission yields of ^{239}Pu is available. In this work, photofission product yields of ^{239}Pu and ^{238}U induced by 22-MeV bremsstrahlung were determined based on high-resolution spectroscopy measurement of delayed γ -rays using a HPGe detector. The results could contribute to photofission data library. They can also provide valuable information on system design based on photofission techniques for nuclear safeguards applications. The results are presented in the first paper.

1.2.2 Monte Carlo Simulation of Photofission Process

It is highly desired to accurately simulate delayed γ -rays from fission reactions of nuclear materials of interest in nuclear safeguards and homeland security applications.

Although simulation of delayed γ -rays has been validated against measurement results for neutron-induced fission [24-26], the simulated delayed γ -rays from photofission have not been compared with measurement outcome for code validation purpose. Figure 1.2 shows an example of comparison of energy spectra measured and simulated from neutron-induced fission reactions. It can be seen that the simulation predicted some peaks that were not observed in measurements or over-predicted. In this work, it was my intention to demonstrate the capabilities and limitations of a general purpose Monte Carlo radiation transport code (MCNPX 2.7.0) in the simulation of photofission process. The measured delayed γ -ray spectra and comparison between measurement results and simulation data were presented in the second paper.

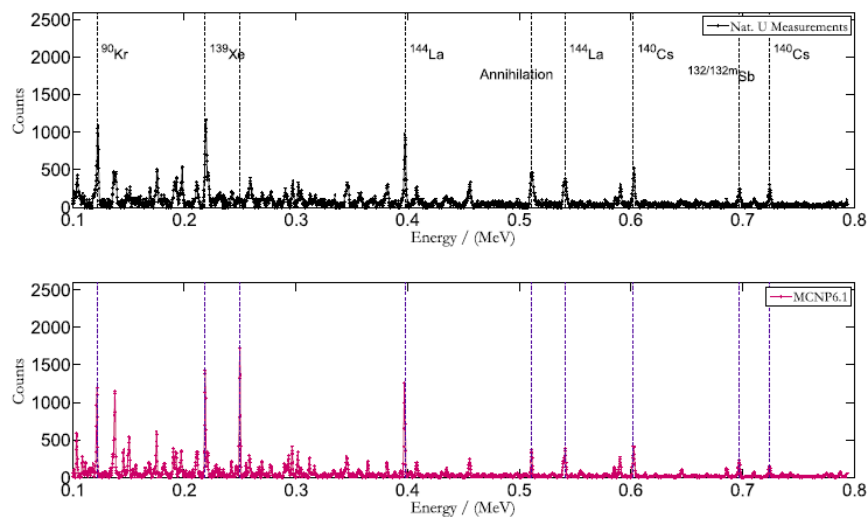


Figure 1.2 Natural uranium measurement (top) and MCNP6.1 simulation (bottom), 0.1-0.8 MeV [26].

Comparing with MCNPX 2.6.0, there are many new features in MCNPX 2.7.0 [27]. Three of the features including embedded source, tall tagging, and LCA play important roles in the simulation of photofission process. These features are described below in detail.

a. Embedded sources

MCNPX 2.7.0 has the capability to allow source distributions to be embedded within each other. The embedded source feature was used to model the linac pulses. The format of specifying an embedded source is $sdef\ tme = (d11 < d12)$. Distributions $d11$ and $d12$ are both for the time variable. Distribution $d11$ covers a small time range. This range is repeated to exactly fill the larger time range of distribution $d12$. The parentheses on the definition of the embedded source are optional, which means $sdef\ tme = (d11 < d12)$ is equivalent to $sdef\ tme = d11 < d12$. For the embedded source $sdef\ tme = (d11 < d12)$, the embedded distributions including $d11$ and $d12$ must start at time zero or a fatal error message is issued. If there are three or more distributions defined in the embedded source, such as $sdef\ tme = (d11 < d12 < d13)$, the starting time of distributions $d11$ and $d12$ must be zero. However, distribution $d13$ can have any time range. The embedded distributions should also fit within each other exactly. A fatal error message, “*embedded distribution has improper range*” will appear in the output file of a MCNP run if they don’t. An example of defining an embedded source is shown below.

Example:

```
sdef  tme= d11<d12<d13
```

```
si11 0 1 2
```

```
sp11 0 1 0
```

```
si12 0 200 300
```

```
sp12 0 1 0
```

```
si13 0 900
```

```
sp13 0 1
```

In this example, there are three distributions defined in the embedded source, *d11*, *d12*, and *d13*. The distribution *d11* defines a micro pulse in time range between 0 and 2 shakes. It is embedded in the distribution *d12*. The time range of the distribution *d12* is from 0 to 300 shakes. The distribution *d12* is then repeated to fill the distribution *d13*. The total time period of the embedded sources as defined in the distribution *d13* is from 0 to 900 shakes.

b. Tally tagging

Tally tagging is also a new feature in MCNPX 2.7.0. It provides the ability to separate a tally into components based on how and where the scoring particle is produced. However, this feature is only implemented for neutron, photon, and electron tallies. The new keyword, *tag*, is used to specify the tally tagging. The keyword is associated with the parameter, *a*, on the *FTn* tally special treatment card. The *FTn* card is associated with a standard *Fn* tally. The format of the *FTn* card is *FTn tag a*, where *n* is the neutron, electron, or photon tally number, and *a* specifies how scatter is to be treated. There are

three choices for the value of the parameter a . If $a=1$, all collided particles will lose their tag and that bremsstrahlung and annihilation photons will be included in the bin of collided particles; If $a=2$, all collided particles will lose their tag, but that bremsstrahlung and annihilation photons will be given special tags that allow them to be segregated. If $a=3$, all collided particles will retain their production tag. The *FU* special tally card must be used to provide binning specifications for the tagged tally. Three distinct pieces of tagging information are given on each bin. First, a cell of interest where particles are produced should be known; second, a target nuclide from which the particle is emitted also needed to be provided; third, a reaction of interest should also be given.

The format of the *FU* card when used in association with the tagging treatment is *FUn bin1 bin2 ... binN*, where each tagging bin_i has the form *CCCCZZAAA.RRRRR*. *CCCC* is the cell number of interest. *ZZAAA* designates a five-digit isotope identifier for a target nuclide, where *ZZ* represents the atomic number and *AAA* the atomic mass number. The reaction identifier for library interactions is specified by *RRRRR*. Delayed particles from fission of *ZZAAA* in all cells are specified by *ZZAAA.99999*. A cell number can be added to only tally delayed particles produced in that cell. Figure 1.3 shows examples of tally tagging in MCNPX 2.7.0.

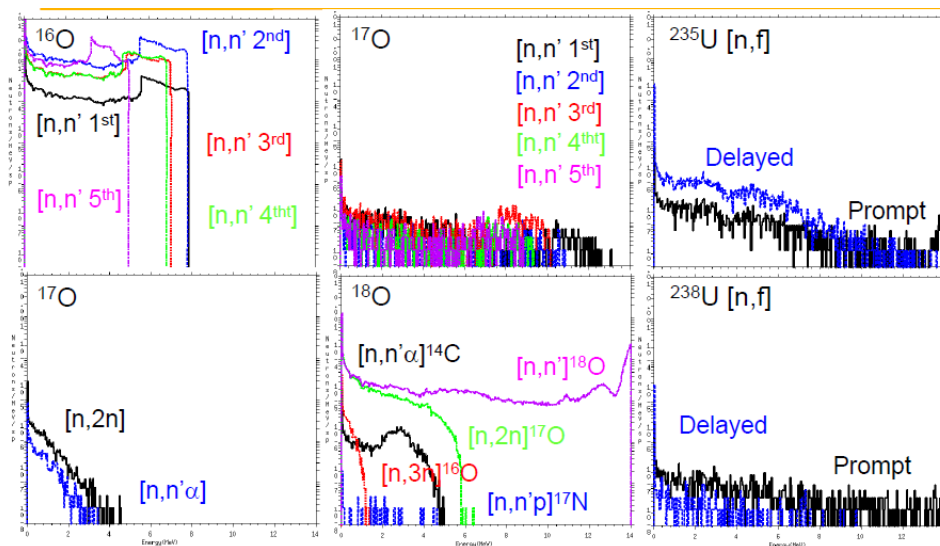


Figure 1.3 Examples of tally tagging in MCNPX 2.7.0 [28].

c. LCA

LCA is used to select the Bertini, ISABEL, CEM03, or INCL4 model. The parameters used in Bertini and ISABEL can also be set by *LCA*. The form of *LCA* is *lca ielas ipreq iexisa ichoic jcoul nexite npidk noact icem ilaq*. The eighth entry on the *LCA* card was set at -2. All other entries on this card were kept at default values. The *LCA* card used in the simulation was *lca 7j -2*. If *noact*=-2 on the *lca* card, table physics is used whenever possible to get the differential data. If it is desired to only get differential data with models, table data can be turned off by setting the *tabl* parameters on the *phys:n* or *phys:h* cards.

1.2.3 High-rate in Pulsed Photofission Environment

In used nuclear fuel assay based on photofission techniques, the energy injection from the pulsed linac is such high that measurement electronic systems will be completely saturated for tens of milliseconds after each pulse. The saturation makes measurement of delayed γ -rays emitted from short-lives photofission fragments impossible, which will lose valuable information about nuclear fuel assemblies. It is well known that the energy rate limit of a commercial RC-feedback preamplifier is a function of the feedback resistor value and the dynamic range of the output voltage from the integrator. Recently, a group from Pacific Northwest National Laboratory (PNNL) demonstrated improved energy rate by changing the output voltage limit from -24 V to -100 V [1].

On the other hand, the input γ -rays count rate can reach 10^6 cps or higher even after cooling for a few years. There is a great demand to develop gamma spectroscopy systems with high-rate capability. Many efforts were concentrated on developing high-resolution high-throughput gamma spectroscopy systems for such high-rate measurements [1, 29]. The ADONIS system developed by CEA was designed to balance the trade-off between energy resolution and throughput rate using a bimodal Kalman smoother [30-31]. The highlight was the introduction of a hidden semi-Markov indicator variable r_k . It is equal to one during charge collection in a detector and zero otherwise. All quantities, such as dead time, throughput rate, and pile-up recovery, depend on an accurate estimation of this variable. Another important concept in the ADONIS system is the representation of

preamplifier output by a state space model whose parameters rely on the indicator variable. This representation is a special case of jump linear Markov systems. The preamplifier output was first used to obtain noisy current signal denoted by y_k . This was achieved by performing convolution of the measured signal with the preamplifier impulse response function. The current signal corrupted with noise was then used as the observation in the state space model. The noise was assumed to be blue with power spectral density $N(\omega) \propto \left(1 + \left(\frac{\omega}{\omega_c}\right)^2\right)$. The blue noise n_k can be treated as a white noise w_k^n with variance Q_n after passing through a digital filter with system function $H(z) = 1 - \alpha z^{-1}$, where α can be expressed as $e^{-T\omega_c}$, T was the sampling rate. A baseline noise b_k was also considered in the state space model to account for potential baseline shift. It was modeled as the integral of a white noise w_k^b with variance Q_b . The ideal detector current was represented by a state p_k , which should be zero without charge migration in a detector and any positive value otherwise. It was modeled as a white noise w_k^p with variance Q_p when the indicator variable was equal to one. The variance Q_p was fixed at a large value. According to the above descriptions, the jump linear Markov system is summarized as follows:

$$\begin{cases} p_{k+1} = r_k w_k^p \\ b_{k+1} = b_k + w_k^b \\ n_{k+1} = -\alpha w_{k-1}^n + w_k^n \\ y_k = p_k + b_k + n_k \end{cases}$$

With the introduction of state vector $X_k = (p_k \ b_k \ n_k \ v_k)^T$ and $W_k = (w_k^p \ w_k^b \ w_k^n)^T$, where v_k is equal to w_{k-1}^n , the above jump linear Markov system can be described as a state space model as follows:

$$\begin{cases} X_{k+1} = F \cdot X_k + B \cdot W_k \\ y_k = H \cdot X_k \end{cases}$$

Where

$$F = \begin{pmatrix} 0 & 0 & 0 & 0 \\ 0 & 1 & 0 & 0 \\ 0 & 0 & 0 & -\alpha \\ 0 & 0 & 0 & 0 \end{pmatrix}, \quad B = \begin{pmatrix} r_k & 0 & 0 \\ 0 & 1 & 0 \\ 0 & 0 & 1 \\ 0 & 0 & 1 \end{pmatrix}, \quad H = (1 \quad 1 \quad 1 \quad 0).$$

The state vector $X_k = (p_k \ b_k \ n_k \ v_k)^T$ was estimated using the Kalman filtering approach. It addresses the general problem of trying to estimate the state x of a discrete-time controlled process [32]. The process is governed by the linear stochastic difference equation as shown below.

$$x_k = A_k x_{k-1} + B_k u_k + w_k$$

Where x_k is the state at time k and represented by a vector of real numbers; usually, the state cannot be directly observed; A_k is the state transition matrix; B_k is the control matrix; w_k is the process noise which is assumed to have a Gaussian distribution with zero mean and covariance Q_k , $w_k \sim N(0, Q_k)$;

A measurement z of the state x at time k is made according to the equation below.

$$z_k = H_k x_k + v_k$$

Where H_k is the observation matrix which maps the state space into the observed space; v_k is the measurement noise which is assumed to be a white noise with covariance R_k , $v_k \sim N(0, R_k)$. The Kalman filter is based on linear dynamic systems in discrete time domain. They are modeled on a Markov chain. There are two steps in the Kalman filtering, prediction and correction. In the prediction step, the Kalman filter predicts priori estimate for the next time step from current state variables along with their error covariance. This estimate is updated to obtain an improved posteriori estimate when a new measurement is available. The update is performed using a weighted average. More weight is given to a priori estimate with higher certainty. Because of the recursive property of this filter, only the present measurement, previous state estimate and its uncertainty matrix are necessary to obtain the posteriori estimate for the next state variables. History of observations or estimates is not required, which can greatly reduce source utilization in hardware and/or software. A schematic view of Kalman filtering is shown in Figure 1.4. The time update predicts the next state using the current state estimate, while the measurement update corrects the estimate using the new available measurement at that time.

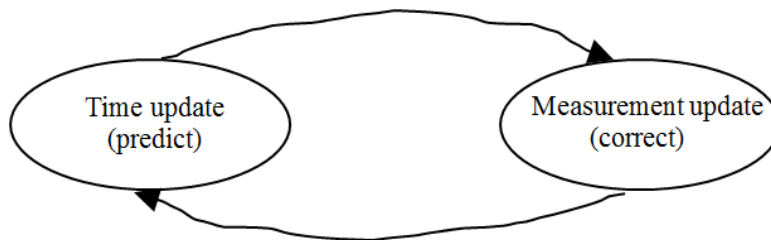


Figure 1.4 Illustration of the Kalman filtering (prediction and correction).

The popular equations for the time and measurement updates are shown below in details [32].

1. Predict

A prior state estimate $x_{k|k-1} = A_k x_{k-1|k-1} + B_k u_k$

A prior error covariance estimate $P_{k|k-1} = A_k P_{k-1|k-1} A_k^T + Q_k$

2. Correct

Kalman gain $K_k = P_{k|k-1} H_k^T (H_k P_{k|k-1} H_k^T + R_k)^{-1}$

A posterior state estimate $x_{k|k} = x_{k|k-1} + K_k (z_k - H_k x_{k|k-1})$

A posterior error covariance estimate $P_{k|k} = (I - K_k H_k) P_{k|k-1}$

As shown in the equations for time update, only the current state and covariance estimates are necessary to produce a prior estimate for the next state. A_k and B_k are the matrixes in the process equation at time k , Q_k is the covariance of the process noise. During the measurement update, the first step is to compute the Kalman gain at time k ,

K_k . Then a posteriori state estimate is generated by incorporating the latest measurement data. The final step is to obtain a posteriori error covariance estimate. This process is repeated when each time and measurement update is complete. This recursive property makes the Kalman filter more appealing compared with the Wiener filter, which is designed to obtain an estimate directly from all of the data instead of the current measurement.

Another example of the efforts to develop gamma spectroscopy systems with high-rate capabilities was based on time-variant trapezoidal filtering concept [1]. In the traditional trapezoidal filtering, especially at high count rate, pile-up phenomenon is a major challenge in high-resolution high-throughput spectroscopy measurement. To obtain good energy resolution piled-up events are rejected at the expense of detection efficiency. It is highly desired to achieve high throughput rate while maintaining good energy resolution. In the time-variant trapezoidal filtering, several traditional time-invariant trapezoidal filters were implemented in parallel, as shown in Figure 1.5. For the best trade-off between energy resolution and throughput, the filters with the longest rise time without causing pile-up were used for energy measurement. A team from PNNL demonstrated that relatively good energy resolution (~ 8 keV at 662 keV) and high throughput (39%) could be achieved at an input count rate as high as 1.03×10^6 cps [1]. Figure 1.6 shows the comparison between energy spectra reconstructed using the traditional trapezoidal filtering method and time-variant trapezoidal filtering approach.

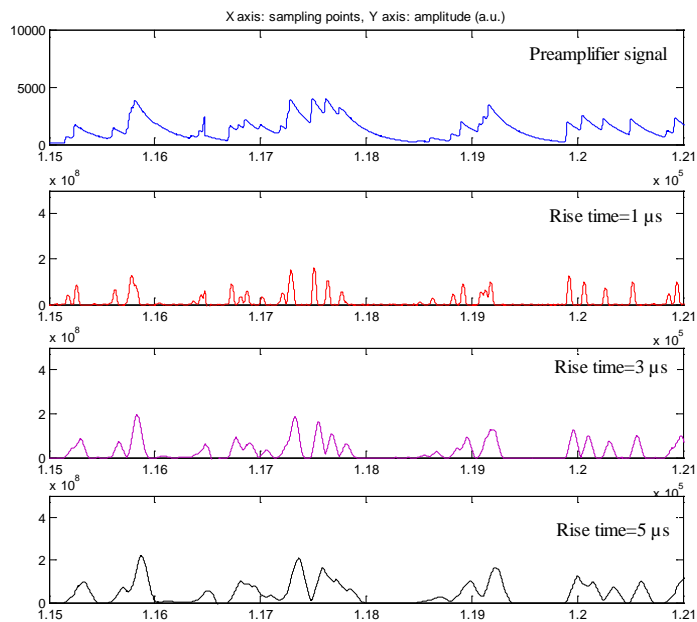


Figure 1.5 Trapezoidal filtering using different rise times (ICR=300 kcps).

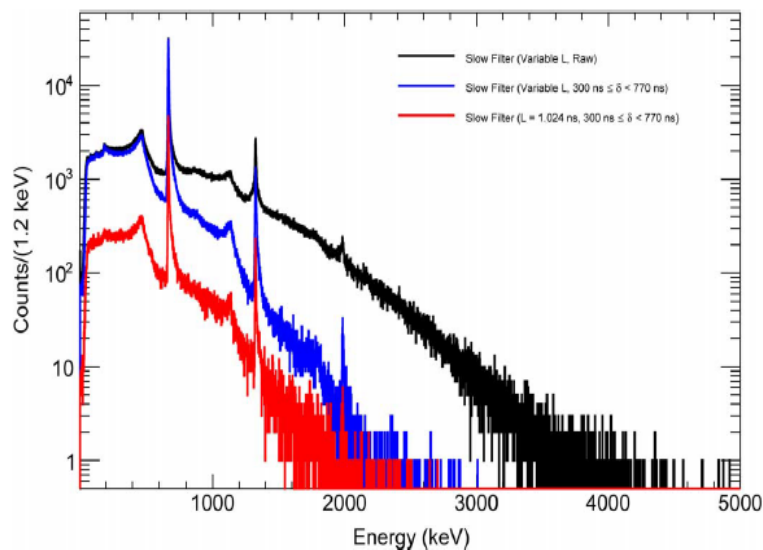


Figure 1.6 Energy spectra reconstructed using the traditional and time-variant trapezoidal filtering methods at input count rate of 1.03×10^6 cps [1].

In this work, a standard HPGe preamplifier was modified to reduce the saturation time due to large energy injection from linac and force the preamplifier signal to return to baseline in a timely manner. The energy resolution after the modifications was evaluated using the trapezoidal filtering method. Also, two advanced pulse processing algorithms including template-matching method and de-randomization technique were investigated to improve the throughput rate with large sacrifice in energy resolution at ultra-high input count rate. The performances of the algorithms in terms of energy resolution and throughput rate were compared with the traditional trapezoidal filtering method. The results on the modifications and the pulse processing algorithms development were published in the third and fourth papers, respectively.

References

1. B. VanDevender, et al., "High-purity germanium spectroscopy at rates in excess of 10^6 events/s," *IEEE Trans. Nucl. Sci.*, vol. 61, pp. 2619-2627, 2014.
2. J. Jones, et al., "Photonuclear-based, nuclear material detection system for cargo containers," *Nucl. Instr. Meth. Phys. Res. B*, vol. 241, pp. 770-776, 2005.
3. E. Reedy, et al., "The detection of delayed gamma-rays between intense bremsstrahlung pulses for discriminating fissionable from non-fissionable materials," *Nucl. Instr. Meth. Phys. Res. A*, vol. 606, pp. 811-815, 2009.
4. J. Stevenson, et al., "Linac based photofission inspection system employing novel detection concepts," *Nucl. Instr. Meth. Phys. Res. A*, vol. 652, pp. 124-128, 2011.
5. D. Norman, et al., "Time-dependent delayed signatures from energetic photon interrogations," *Nucl. Instr. Meth. Phys. Res. B*, vol. 261, pp. 316-320, 2007.
6. R. Runkle, et al., "Rattling nucleons: New developments in active interrogation of special nuclear material," *Nucl. Instr. Meth. Phys. Res. A*, vol. 663, pp. 75-95, 2012.

7. X. Wen, et al., Photofission product yields of ^{238}U and ^{239}Pu with 22-MeV bremsstrahlung, *Nucl. Instr. Meth. Phys. Res. A*, 2016, (in revision).
8. X. Wen, et al., Simulation and measurement of delayed γ -rays after photon-induced fission, *Nucl. Instr. Meth. Phys. Res. A*, vol. 729, pp. 781-787, 2013.
9. X. Wen, et al., Evaluation of a modified HPGe preamplifier for high-rate spectroscopy measurements in a pulsed photonuclear environment, *Nucl. Tech.*, vol. 194, 2016.
10. X. Wen, et al., Study on a digital pulse processing algorithm based on template-matching for high-throughput spectroscopy, *Nucl. Instr. Meth. Phys. Res. A*, vol. 784, pp. 269-273, 2015.
11. Nuclear nonproliferation, United States Government Accountability Office, 2005.
12. K. Murakami, "Nuclear safeguards concepts, requirements, and principles applicable to nuclear security," 2012.
13. K. Davenport, et al., "Assessing progress on nuclear nonproliferation and disarmament," 2013.
14. <http://www.lanl.gov/orgs/n/n1/panda/11.%20Nuclear%20Data%20for%20NDA.pdf>
15. T. Gozani, "Fission signatures for nuclear material detection," *IEEE Trans. Nucl. Sci.*, vol. 56, pp. 736-741, 2006.
16. K. Jordan, et al., "Detection of ^{235}U in hydrogenous cargo with differential die-away analysis and optimized neutron detectors," *Nucl. Instr. Meth. Phys. Res. A*, vol. 579, pp. 388-390, 2007.
17. D. Dore, et al., "Delayed neutron and delayed photon characteristics from photofission of ^{232}Th , $^{235,238}\text{U}$ and ^{237}Np with endpoint bremsstrahlung photons in the giant dipole resonance region," *International Workshop on Nuclear Fission and Fission-Product Spectroscopy*, 2009.
18. W. Hage, et al., "Nondestructive fissile material assay by induced fission neutron correlation," *Nucl. Instr. Meth. Phys. Res. A*, vol. 551, pp. 396-419, 2005.
19. J. Meason et al., "Photofission of ^{238}U induced by 17.5-MeV monoenergetic gamma rays," *Phys. Rev.* 142, 1966.

20. E. Jacobs et al., "Product yields for the photofission of ^{238}U with 12-, 15-, 20-, 30-, and 70-MeV bremsstrahlung," *Phys. Rev. C*, 19, 1979.
21. E. Jacobs et al., "Product yields for the photofission of ^{235}U with 12-, 15-, 20-, 30-, and 70-MeV bremsstrahlung," *Phys. Rev. C*, 21, 1980.
22. D. Wehe et al., "Observation of ^{238}U photofission products," *IEEE Trans. Nucl. Sci.*, vol. 53, pp. 1430-1434, 2006.
23. F. Carrel, et al., "New experimental results on the cumulative yields from thermal fission of ^{235}U and ^{239}Pu and from photofission of ^{235}U and ^{238}U induced by bremsstrahlung," *IEEE Trans. Nucl. Sci.*, vol. 58, pp. 2064-2072, 2011.
24. J. Durkee, et al., "Delayed-gamma simulation using MCNPX," *Nucl. Tech.*, vol. 168, pp. 761-764, 2009.
25. J. Durkee, et al., "Delayed-gamma signature calculation for neutron-induced fission and activation using MCNPX. Part II: Simulations," *Progress in Nuclear Energy*, vol. 51, pp. 828-836, 2009.
26. M. Andrews, et al., "MCNP6 simulations of gamma line emissions from fission products and their comparisons to plutonium and uranium measurements," *Progress in Nuclear Energy*, vol. 79, pp. 87-95, 2015.
27. D. Pelowitz, et al., "MCNPX 2.7.E extensions," LA-UR-11-01502, 2011.
28. M. James, "MCNPX 2.7.X - new features being developed," *IEEE/NSS*, Orlando, FL, 2009.
29. E. Barat, et al., "ADONIS: a new system for high count rate HPGe spectrometry," *IEEE Nuclear Science Symposium Conference Record*, N30-6, 2006.
30. E. Barat, et al., "A bimodal Kalman smoother for nuclear spectrometry," *Nucl. Instr. Meth. Phys. Res. A*, vol. 567, pp. 350-352, 2006.
31. E. Barat, et al., "ADONIS: A new concept of x/gamma pulse analyzer," *ANIMMA Conference Record*, N210, 2009.
32. G. Welch, et al., *An introduction to the Kalman filter*, 2006.

2 First Manuscript

Photofission product yields of ^{238}U and ^{239}Pu with 22-MeV bremsstrahlung

Xianfei Wen¹, Haori Yang^{1*}

¹*School of Nuclear Science and Engineering, Oregon State University, Corvallis, OR*

97331, USA

Abstract

In homeland security and nuclear safeguards applications, non-destructive techniques to identify and quantify special nuclear materials are in great demand. Although nuclear materials naturally emit characteristic radiation (e.g. neutrons, γ -rays), their intensity and energy are normally low. Furthermore, such radiation could be intentionally shielded with ease or buried in high-level background. Active interrogation techniques based on photofission have been identified as effective assay approaches to address this issue. In designing such assay systems, nuclear data, like photofission product yields, plays a crucial role. Although fission yields for neutron-induced reactions have been well studied and readily available in various nuclear databases, data on photofission product yields is rather scarce. This poses a great challenge to the application of photofission techniques. In this work, short-lived high-energy delayed γ -rays from photofission of ^{238}U were measured in between linac pulses. In addition, a list-mode system was developed to measure relatively long-lived delayed γ -rays from photofission of ^{238}U and ^{239}Pu after the

irradiation. Time and energy information of each γ -ray event were simultaneously recorded by this system. Photofission product yields were then determined using the measured delayed γ -ray spectra.

Keywords: photofission; delayed γ -rays; product yields; list-mode

*Corresponding author.

Address: School of Nuclear Science and Engineering, Oregon State University, Corvallis, OR 97331, USA.

E-mail: haori.yang@oregonstate.edu (H. Yang).

2.1 Introduction

It is crucial to accurately and efficiently characterize special nuclear materials in homeland security and nuclear safeguards applications. Non-destructive evaluation techniques for this purpose are of great interest in related communities. These techniques fall into two categories, depending on whether or not an interrogating source is used to induce new reactions during the assay. Passive nondestructive assay is challenging in many scenarios. Although nuclear materials naturally emit characteristic radiation (e.g. neutrons, γ -rays), the intensity and energy of such radiation are normally low. For example, a well-known passive approach to determine uranium enrichment is to measure the relative intensity of characteristic γ -rays at 186 keV and 1001 keV. This approach is

not effective when the sample is heavily shielded by high-Z materials, such as lead. Active interrogation based on measurement of high-energy γ -rays and/or neutrons from induced nuclear fission reactions has been identified as an effective approach to address such challenges [1-11]. When high-energy photons are used as the interrogation source, photofission reactions could be induced in nuclear materials. Two to three prompt neutrons and about seven prompt γ -rays are produced within 10^{-15} s after a photofission reaction [12]. On average, two fission products are created. These products are usually produced in unstable states and possess excessive neutrons. Delayed neutrons and delayed γ -rays are subsequently emitted during the relaxation of fission products to more stable levels. Approximately 0.01 to 0.03 delayed neutrons and seven delayed γ -rays are produced per fission [12].

It is challenging to measure the energies of prompt γ -rays in active interrogation, due to the high radiation background. For example, in our measurements at Idaho Accelerator Center (IAC), the spectroscopy systems were completely saturated for several milliseconds following each linac pulse due to large energy injection from the interrogation source [11]. Spectroscopy measurement of delayed γ -rays has some advantages over delayed neutron counting. First, unique delayed γ -ray spectra exist for each nuclide and can serve as the basis to determine isotopic composition of the sample [7, 9, 13-14]. Secondly, since the overall intensity of delayed γ -rays is much higher than that of delayed neutrons, detection sensitivity and accuracy could be improved in case that the total counts are of interest. Thirdly, high-energy γ -rays are more penetrating than

neutrons in hydrogenous materials. This is greatly beneficial to detection of nuclear materials hidden in hydrogenous environment. Nevertheless, compared with measurements of delayed neutrons, a much higher background level exists in the delayed γ -rays measurements. At ultra-high input rate (e.g. 10^6 cps), how to perform high-resolution high-throughput gamma spectroscopy measurement is challenging.

Design and development of active assay systems based on photofission technique largely rely on the availability of nuclear data, especially photofission product yields. While yields for neutron-induced fission of most nuclear materials (e.g. ^{232}Th , ^{235}U , ^{238}U , ^{239}Pu) have been well studied, verified and made available in various nuclear databases (e.g. the Evaluated Nuclear Data File), results on photofission product yields are relatively scarce. Non-exhaustive examples of the photofission yields measurement are summarized here. Meason et al. reported photofission yields of ^{238}U back in 1965 [15]. In their study, monoenergetic γ -rays (17.5 MeV) were produced through the $^7\text{Li}(\text{p}, \gamma)^8\text{Be}$ reaction. Low-level β counting techniques were used to determine the yields. Photofission yields of ^{235}U and ^{238}U were measured by Jacobs et al. with 12-, 15-, 20-, 30- and 70- MeV bremsstrahlung photon sources [16-17]. The fission product mass distribution for ^{235}U at different bremsstrahlung beam energies was shown to have a doubly peaked shape without fine structure. The authors also observed a strong dependence of the symmetric mass yields and near independence of the asymmetric yields on the end-point energy of the bremsstrahlung source. Photofission yields of ^{238}U were also determined by Wehe et al. using a 9-MeV bremsstrahlung beam [18]. Delayed

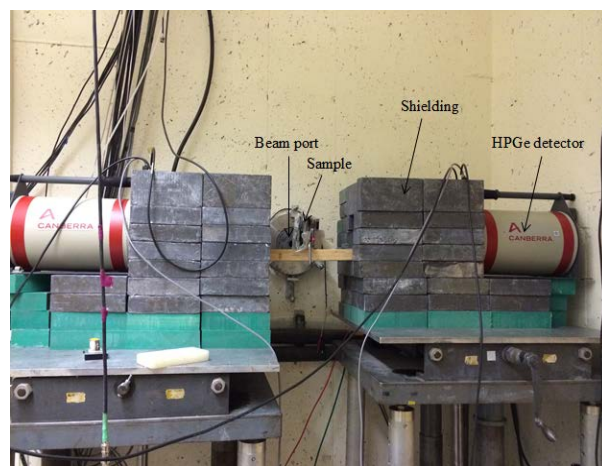
γ -rays were measured using High-purity Germanium (HPGe) and NaI (Tl) detectors after photon irradiation of a ^{238}U sample. Cumulative yields of photofission products (e.g. ^{93}Sr , ^{132}Sb , $^{132\text{m}}\text{Sb}$, ^{89}Rb , and ^{133}Sb) were reported. In the effort to characterize nuclear waste packages using photon activation analysis techniques, several measurement campaigns were performed by Carrel et al. to determine the photofission yields for optimizing the system design. Photofission yields of ^{235}U and ^{238}U induced by 16.3-MeV and 19.4-MeV bremsstrahlung x-rays were recently published by this group [19]. To the best of the authors' knowledge, no data concerning the photofission yields of ^{239}Pu is previously available.

In this work, a linac was used to generate high-energy interrogating bremsstrahlung x-rays. The maximum energy of the x-rays was approximately 22 MeV. To perform high-resolution spectroscopy measurements, HPGe detectors were used. The data acquisition system used was a Canberra Lynx Multi Channel Analyzer (MCA) controlled via Genie2K or ProSpect software. Half-lives of high-energy delayed γ -rays ($E_\gamma > 2.7$ MeV) emitters from photofission of ^{238}U are much shorter compared with the total irradiation time (i.e. seconds vs tens of minutes). As a result, most of these high-energy γ -rays were not observable after the irradiation and could be only measured in between linac pulses. On the other hand, the photofission products producing low-energy delayed γ -rays usually have half-lives ranging from minutes to hours, such γ -rays can be measured after a sample cooling period. A list-mode system was developed to measure such low-energy delayed γ -rays from photofission of ^{238}U and ^{239}Pu after irradiation. Both time and energy

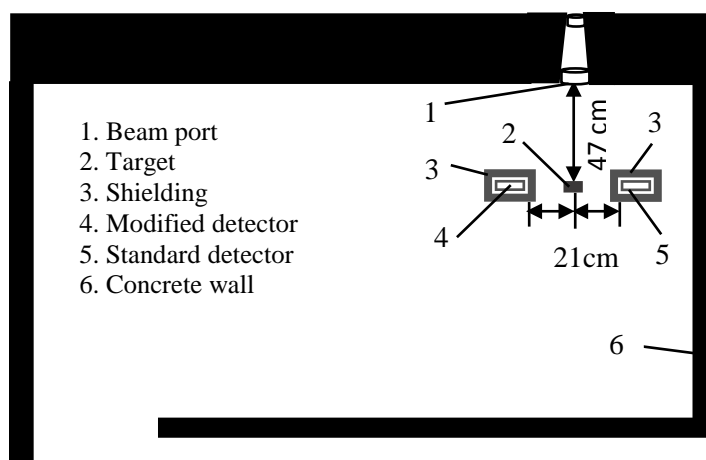
information of each γ -ray event were recorded. The measured delayed γ -ray spectra were then used to determine the photofission product yields of ^{238}U and ^{239}Pu .

2.2 Experimental Setup

Delayed γ -rays from photofission of ^{238}U and ^{239}Pu were measured in our experiments at IAC. A picture of the experimental setup and its schematic drawing are shown in Figure 2.1. The pulsed high-energy x-ray beam was generated when high-energy electrons from a linac impinged a tungsten radiator. The repetition frequency of the linac was set at 10 Hz. The width of each linac pulse was 4 μs . Therefore, the total time available for measurement between two adjacent pulses was around 100 milliseconds. The amount of charge carried by each electron pulse was approximately 86 nC. The acceleration potential of the linac was set to 22 MV. The linac was separated from the measurement cell by a 1.8 m thick concrete wall. Two lead collimators were used at the end of the beam path. The first collimator was 61 cm away from the x-ray converter. It was followed by the second collimator and the distance between them was 1.79 m. The thickness of the collimators was 15.24 cm. The diameter of the entrance and exit beam opening was 1.27 cm and 3.81 cm, respectively. The beam diameter at the sample position was approximately 7.5 cm. The targets (see Figure 2.2) used in the measurements were an 18.9 g/cm^2 uranium plate and a 3 gram plutonium sample. The isotopic composition of the plutonium sample was 95 a/o ^{239}Pu and 5 a/o ^{240}Pu . They were placed on the centerline of the x-ray beam during the following experiments. The distance from the beam port to the target location was around 47 cm.



(a)



(b)

Figure 2.1 A picture of the experimental setup for the measurement of delayed γ -rays from photofission. (b) Schematic drawing of the experimental setup.



Figure 2.2 The uranium and plutonium samples used in the photofission experiments.

Two n-type coaxial HPGe detectors were used to perform high-resolution spectroscopy measurements. The model number of both detectors was GC4020. The relative efficiency was 40%. The crystal size was roughly 2.4" diameter by 2.3" height. The centerline of the detector was perpendicular to the beam line. The distance between the target and the front surface of the shielding was 13 cm. The size of the front opening was 12 cm \times 12 cm. The entrance window of the detectors was collimated down to 8 cm with lead bricks to reduce incoming count rate. These two detectors were identical except that the preamplifier on one of the detectors was modified to handle higher count rate. Compared with the standard preamplifier, the modified one had a slightly worse energy resolution (e.g. 2.4 keV vs 2.2 keV @ 662 keV) and a smaller saturation time (e.g. 2.5 ms vs 5.7 ms). The detector choices did not have an impact on the results. For more details on this modified preamplifier, the reader is referred to our previous publication [20]. The degradation of energy resolution was deemed to be trivial, and delayed γ -ray spectra measured using both detectors were used to determine photofission product yields. In

measurements of short-lived high-energy delayed γ -rays in between linac pulses, the detector coupled with the standard preamplifier was used. It was also used to measure delayed γ -rays from photofission of ^{239}Pu after irradiation. The long-lived delayed γ -rays from photofission of ^{238}U after cooling were measured using the detector with the modified preamplifier.

2.3 Results and Discussion

2.3.1 Photofission Product Yields of ^{238}U Measured in between Linac Pulses

The signals from the preamplifiers were sent to the Canberra Lynx MCA. It was located in a control room separated from the measurement cell. The MCA was controlled by the Genie2K software. Due to large interference (e.g. neutron-capture γ -rays, scattered photons), signals immediately following each linac pulse were gated out to obtain clean delayed γ -ray spectra. An arbitrary-function generator (model number: Agilent AFG3021C) was used to generate the gate signal. It was triggered by each linac pulse and stayed closed for 10 ms. The total measurement time was 45 minutes. Thus, there were 2.7×10^4 irradiation cycles in total and the live counting time was 40.5 minutes. Figure 2.3 shows the irradiation, cooling, and measurement windows in the measurements after irradiation and in between linac pulses.

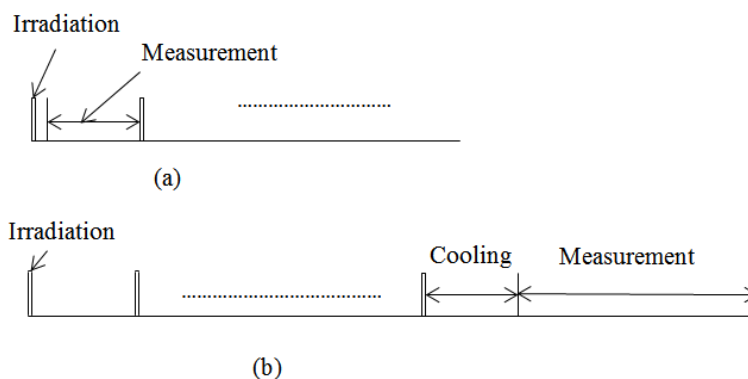


Figure 2.3 (a) Measurement of delayed γ -rays from photofission of ^{238}U in between linac pulses; (b) Measurement of delayed γ -rays from photofission of ^{238}U and ^{239}Pu after irradiation.

Delayed γ -rays with energy above 3 MeV uniquely indicate the presence of special nuclear materials [11, 21]. In our previous study, high-energy delayed γ -rays were detected, but individual photopeak was not quantitatively analyzed due to the small counts under the peak. In current work, high-energy delayed γ -rays ($E_{\gamma} \sim 3 - 4.5$ MeV) from photofission of ^{238}U were not only observed but also quantitatively analyzed in between linac pulses. As an example, the delayed γ -ray spectrum between 3.9 MeV and 4.5 MeV is shown in Figure 2.4. Each prominent photopeak was assigned to a parent nuclide based on the nuclear database published by Firestone et al. [22]. This database was also used to obtain the half-lives of the identified parent nuclides. Table 2.1 summarizes the energies of the identified γ -rays, parent nuclides and their half-lives. As shown in Table 2.1, high-energy delayed γ -rays are most likely emitted by short-lived nuclides such as ^{98}Y , ^{97}Y , $^{90\text{m}}\text{Rb}$, ^{90}Rb , ^{93}Rb , ^{91}Rb , ^{88}Br , ^{89}Br , and ^{87}Br . The half-lives of these photofission products range from 0.5 to 258 seconds.

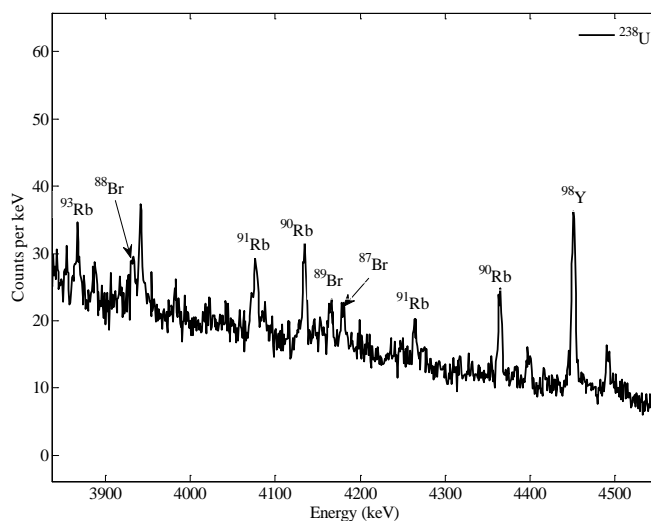


Figure 2.4 Measured high-energy delayed γ -rays from photofission of ^{238}U (3.9-4.5 MeV).

To determine the yields of the identified photofission products, counts under each photopeak were first calculated. It was obtained using the add-on package (Interactive Peak Fit) within the Genie2K software. VMS Standard Peak Search Fit was selected as the fitting algorithm. The peak locate portion of this algorithm utilizes the 2nd order difference method. The peak analysis portion implements the Gaussian fit method. The number of background channels was set to 4. This parameter specified the number of continuum channels used for background estimation on either side of the region of interest. The background counts were derived from the continuum using a step function. The Vary FWHM option was enabled to allow variation of FWHM in the fitting region. In addition to peak energy and peak area, uncertainty on the peak area was also reported and considered to be the most significant source of uncertainty in the calculation of photofission product yields. Since the half-lives of these products are relatively short

compared to the measurement time (tens of seconds vs 45 minutes), it is reasonable to assume that they decay away by the end of the last irradiation cycle. There was not any correction to apply due to the fact that the measurement was started 10 ms after the end of the irradiation. The reason was that the gate time (10ms) was much shorter than the half-lives of the parent nuclides (ms vs seconds) such that the probability of decaying away of a parent nuclide within the gate time was very small. Due to the difficulty of determining the absolute number of total photofission events occurred in nuclear samples, only the relative yields were reported here. The yield was calculated using the formula, $N = FY\varepsilon\eta$, where N was the count under a photopeak, F was the number of photofission events, Y was the photofission yield, ε was the absolute photopeak efficiency of the HPGe detectors; η was the branching ratio of the peak. Table 1 shows the photofission product yields of ^{238}U . As shown in Table 2.1, although large uncertainties exist for some photofission products, including ^{93}Rb (3867.6 keV), ^{89}Br (4166.3 keV) and ^{87}Br (4180.5 keV), most of the uncertainties are in the range from 3% to 15%. The yield of a photofission product calculated based on delayed γ -rays at different energies was comparable. For example, for nuclide ^{97}Y , the relative yield was determined based on photopeaks at 3287.6 keV, 3401.3 keV and 3549.5 keV. The results were fairly consistent, being 0.070 ($\pm 3\%$), 0.078 ($\pm 4\%$) and 0.072 ($\pm 16\%$), respectively.

Table 2.1 Measured photofission product yields of ^{238}U based on high-energy delayed γ -rays.

Nuclide	Half-life (seconds)	Energy (keV)	Relative yield	Uncertainty (%)
^{87}Br	55.6	4180.5	0.029	18
^{88}Br	16.3	3932.4	0.055	11
^{89}Br	4.3	4166.3	0.027	20
^{90}Rb	158	3534.2	0.043	13
		4135.5	0.041	13
		4365.9	0.043	7
$^{90\text{m}}\text{Rb}$	258	3317.0	0.019	10
^{91}Rb	58.4	3599.7	0.072	4
		4078.3	0.073	8
^{93}Rb	5.8	3458.2	0.050	14
		3867.6	0.059	26
^{95}Sr	23.9	2717.3	0.102	12
		2933.1	0.116	7
^{97}Y	3.8	3287.6	0.070	3
		3401.3	0.078	4
		3549.5	0.072	16
^{98}Y	0.5	2941.3	0.076	4
		3310.0	0.076	7
		4450.2	0.079	4
^{106}Tc	35.6	2789.3	0.094	16
^{136}I	83.4	2868.9	0.160	7

2.3.2 Photofission Product Yields of ^{239}Pu and ^{238}U Measured after Irradiation

As discussed above, some photofission products have relatively long half-lives, allowing measurement of delayed fission γ -rays long after the irradiation. In these

measurements, the settings for the linac were not changed in the plutonium experiment. The detector used here was the HPGe detector coupled with the standard preamplifier. The irradiation time was 69 minutes. The measurement started after a cooling period of 15 minutes. The total data acquisition time was 1.5 hours. For the uranium measurement, the linac repetition frequency was changed from 10 Hz to 15 Hz. The amount of charge carried in each linac pulse was increased to 113 nC. The HPGe detector coupled with the modified preamplifier was used in this measurement. The sample was an 18.9 g/cm^2 ^{238}U plate. The data collection started after cooling for 15 minutes following a 2-hour irradiation. The total counting time was 3 hours.

To record time and energy information of each γ -ray event, a list-mode system was developed. It consisted of the Canberra Lynx MCA, the ProSpect software and a customized post-processing script. The ProSpect software is an application that can be used to control, collect and analyze gamma spectroscopy data. The parameters of the MCA and the settings of the data acquisition process are easily accessible via a graphical user interface. Measurement data can be exported in the format of a Text, Excel, PDF or CAM file. Acquisition modes include digital oscilloscope (for viewing the raw and shaped signals), SCA, PHA, and LIST. The LIST mode was selected in our measurements to simultaneously record time and energy information of each γ -ray event. The spectroscopy data was transferred to a host PC through an Ethernet cable and stored for offline processing using the customized script. Figure 2.5 shows delayed γ -ray spectra measured in different time windows using this list-mode approach. Change of photopeak

count rate with time was then used to estimate half-lives of photofission products. Table 2.2 shows examples of calculated half-lives. These results provided valuable information to identify the parent nuclides despite difference between the estimated half-lives and those reported in standard nuclear databases. Due to the small size of the plutonium sample and short half-lives of photofission products emitting high-energy γ -rays, there were not enough counts to determine the yields of photofission products based on delayed γ -rays above 1.5 MeV for ^{239}Pu . Only peaks from 640 keV to 1436 keV were used to calculate ^{239}Pu photofission product yields. For the ^{238}U sample, most of the high-energy delayed γ -rays ($E_\gamma > 3 \text{ MeV}$) were not observed in the list-mode measurement due to the short half-lives of their emitters. The photofission yields were thus only determined using peaks under 3 MeV.

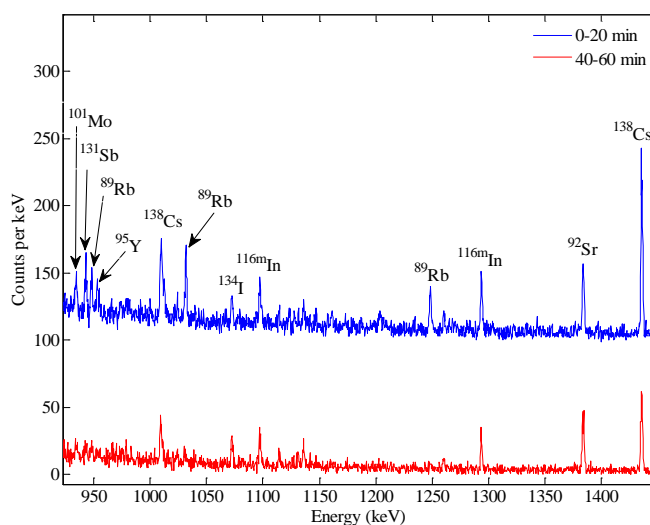


Figure 2.5 Measured delayed γ -rays from photofission of ^{239}Pu using the list-mode system (0.9-1.5 MeV).

Table 2.2 Examples of calculated half-lives of nuclides produced in photofission reactions.

Energy (keV)	Nuclide	Calculated $T_{1/2}$ (min)	Database $T_{1/2}$ (min) [22]
1031.9	⁸⁹ Rb	11.6	15.2
918.7	⁹⁴ Y	14.3	18.7
1612.4	¹⁰⁴ Tc	21.9	18.3
1293.6	^{116m} In	60.9	54.3
839.5	¹³⁰ Sb	34.2	39.5
847.0	¹³⁴ I	57.8	52.5
2218.0	¹³⁸ Cs	36.5	33.4
1524.6	¹⁴² La	86.6	91.1

To calculate peak area, the same approach described in Section 2.3.1 was applied here as well. The photofission product yields were derived using the formula below. An assumption made during the derivation was that photofission events occurred only at the beginning of each linac pulse. It is a reasonable assumption since the pulse width was extremely narrow compared with the time duration between adjacent linac pulses (i.e. 4 μ s vs 0.1~ 0.066 s). The number of net counts under a peak from the decay of photofission products formed due to the n th pulse can be calculated as follows:

$$N_n = FY\varepsilon\eta e^{-\lambda(T_i - (n-1)\tau)} e^{-\lambda T_c} (1 - e^{-\lambda T_m}) \quad (1)$$

where F was the number of photofission events occurred in a single pulse; Y was defined as the photofission yield; ε was the absolute photopeak efficiency of the HPGe detectors; η was the branching ratio of the peak; λ was the decay constant; T_i was the time period between the beginning of the first pulse and the ending of the last pulse; T_c was the length

of cooling time; T_m was the total data acquisition time. The total net counts were obtained by taking the sum of N_n over all the pulses.

$$N = \sum_{n=1}^{n=T_i/\tau} N_n = FY\epsilon\eta \frac{(e^{-\lambda T_i} - 1)e^{-\lambda T_c}(1 - e^{-\lambda T_m})}{1 - e^{-\lambda \tau}} \quad (2)$$

The calculated photofission product yields of ^{239}Pu and ^{238}U are summarized in Tables 2.3 and 2.4, respectively. As shown in these tables, uncertainties for most photofission products were acceptable ($< 15\%$). For the following products, $^{98\text{m}}\text{Nb}$ (787.4 keV), ^{131}Sb (943.4 keV), ^{95}Y (954.0 keV), ^{89}Rb (1248.2 keV) and ^{138}Xe (2015.8 keV), the uncertainties are relatively large due to the low counts under these peaks. The uncertainties could be reduced by increasing the sample size or measurement time.

Table 2.3 Measured photofission product yields of ^{239}Pu using the list-mode system.

Nuclide	Half-life	Energy (keV)	Relative yield	Uncertainty (%)
^{89}Rb	15.2 m	1031.9	0.033	12
		1248.2	0.036	13
^{92}Sr	2.7 h	1383.9	0.040	5
^{94}Y	18.7 m	918.7	0.046	7
^{95}Y	10.3 m	954.0	0.172	22
$^{98\text{m}}\text{Nb}$	51.3 m	787.4	0.009	18
$^{116\text{m}}\text{In}$	54.3 m	1097.3	0.019	10
		1293.6	0.016	6
^{130}Sb	39.5 m	793.5	0.014	9
		839.5	0.011	10
^{131}Sb	23.0 m	943.4	0.021	16
$^{133\text{m}}\text{Te}$	55.4 m	912.7	0.028	8
^{134}Te	41.8 m	742.6	0.116	7
^{134}I	52.5 m	847.0	0.060	2

		884.1	0.058	3
^{138}Cs	33.4 m	1009.8	0.050	8
		1435.8	0.060	3
^{142}La	91.1 m	641.3	0.049	6

Table 2.4 Measured photofission product yields of ^{238}U using the list-mode system.

Nuclide	Half-life	Energy (keV)	Relative yield	Uncertainty (%)
^{87}Kr	76.3 m	2554.8	0.010	6
^{88}Kr	2.8 h	2392.1	0.010	3
^{89}Rb	15.2 m	1031.9	0.015	15
		1248.2	0.013	24
^{92}Sr	2.7 h	1383.9	0.017	1
$^{116\text{m}}\text{In}$	54.3 m	1293.6	0.003	9
$^{133\text{m}}\text{Te}$	55.4 m	2005.3	0.038	11
^{134}I	52.5 m	1072.6	0.031	6
^{135}I	6.6 h	1260.4	0.026	6
^{138}Xe	14.1 m	2015.8	0.018	23
^{138}Cs	33.4 m	2218.0	0.026	4
		2639.6	0.025	4
^{142}La	91.1 m	2187.2	0.019	11
		2397.8	0.015	4

2.4 Conclusions and Future Work

In this work, high-energy bremsstrahlung x-rays generated by a pulsed linac were used as the excitation source to induce photofission reactions in the ^{238}U and ^{239}Pu samples. High-resolution spectroscopy measurements of delayed γ -rays were performed using HPGe detectors. An advanced pulse processing unit served as the data acquisition system. Short-lived high-energy (> 2.7 MeV) delayed γ -rays were measured in between linac pulses. A list-mode system was developed to measure relatively long-lived delayed γ -rays after sample cooling. The measured spectra were then used to determine the photofission

product yields of ^{238}U and ^{239}Pu . To the best of the author's knowledge, although product yields for neutron-induced fission of nuclides of interest (e.g. ^{232}Th , ^{235}U , ^{238}U , ^{239}Pu) were well studied and are available in various nuclear databases, published photofission product yields are rather scarce. Photofission product yields of ^{238}U and ^{239}Pu determined in this work could contribute to photofission data library. They can also provide valuable information for designing assay systems based on photonuclear techniques in homeland security and nuclear safeguards applications. In our future work, the measurement outcomes will be compared with Monte Carlo simulation results to demonstrate the capabilities and limitations of currently available package (e.g. MCNP) regarding simulation of photofission process.

Acknowledge

This research is being performed using funding received from the DOE Office of Nuclear Energy's Nuclear Energy University Programs. The authors also want to thank the Domestic Nuclear Detection Office (DNDO) Academic Research Initiative (ARI) program for its support.

References

1. T. Gozani, "Active nondestructive assay - principles and applications," NUREG/CR-0602, 1981.
2. M. Gmar et al., "Use of delayed gamma spectra for detection of actinides (U, Pu) by photofission," *Nucl. Instr. Meth. Phys. Res. A*, vol. 422, pp. 841-845, 1999.

3. J. Jones, et al., "Photonuclear-based, nuclear material detection system for cargo containers," *Nucl. Instr. Meth. Phys. Res. B*, vol. 241, pp. 770-776, 2005.
4. B. Micklich et al., "Nuclear materials detection using high-energy γ -rays," *Nucl. Instr. Meth. Phys. Res. B*, vol. 241, pp. 782-786, 2005.
5. D. Norman, et al., "Time-dependent delayed signatures from energetic photon interrogations," *Nucl. Instr. Meth. Phys. Res. B*, vol. 261, pp. 316, 2007.
6. A. Hunt, et al., "Fission signature interferences in active interrogation techniques utilizing high-energy bremsstrahlung," *IEEE Nuclear Science Symposium Conf.*, 2012.
7. F. Carrel, et al., "Identification and differentiation of actinides inside nuclear waste packages by measurement of delayed gammas," *IEEE Trans. Nucl. Sci.*, vol. 57, p. 2862, 2010.
8. H. Rennhofer et al., "Detection of SNM by delayed gamma rays from induced fission," *Nucl. Instr. Meth. Phys. Res. A*, vol. 652, pp. 140-142, 2011.
9. R. Marrs et al., "Fission-product gamma-ray line pairs sensitive to fissile material and neutron energy," *Nucl. Instr. Meth. Phys. Res. A*, vol. 592, pp. 463-471, 2008.
10. R. Runkle, et al., "Rattling nucleons: New developments in active interrogation of special nuclear material," *Nucl. Instr. Meth. Phys. Res. A*, vol. 663, pp. 75-95, 2012.
11. X. Wen et al., "Simulation and measurement of delayed γ -rays after photon-induced fission," *Nucl. Instr. Meth. Phys. Res. A*, vol. 729, pp. 781-787, 2013.
12. T. Gozani, "Fission signatures for nuclear material detection," *IEEE Trans. Nucl. Sci.*, vol. 56, pp. 736 -741, 2009.
13. C. Hollas et al., "Analysis of fissionable material using delayed gamma rays from photofission," LA-UR-86-3363, 1986.
14. D. Beddingfield et al, "Identification of fissile materials from fission product gamma-ray spectra," *Nucl. Instr. Meth. Phys. Res. A*, vol. 417, pp. 405-412, 1998.
15. J. Meason et al., "Photofission of ^{238}U induced by 17.5-MeV monoenergetic gamma rays," *Phys. Rev.* 142, 1966.
16. E. Jacobs et al., "Product yields for the photofission of ^{238}U with 12-, 15-, 20-, 30-, and 70-MeV bremsstrahlung," *Phys. Rev. C*. 19, 1979.

17. E. Jacobs et al., "Product yields for the photofission of ^{235}U with 12-, 15-, 20-, 30-, and 70-MeV bremsstrahlung," *Phys. Rev. C*, vol. 21, 1980.
18. D. Wehe et al., "Observation of ^{238}U photofission products," *IEEE Trans. Nucl. Sci.*, vol. 53, pp. 1430-1434, 2006.
19. F. Carrel, et al., "New experimental results on the cumulative yields from thermal fission of ^{235}U and ^{239}Pu and from photofission of ^{235}U and ^{238}U induced by bremsstrahlung," *IEEE Trans. Nucl. Sci.*, vol. 58, pp. 2064-2072, 2011.
20. X. Wen, et al., "Evaluation of a modified HPGe preamplifier for high-rate spectroscopy measurements in a pulsed photonuclear environment," *Nucl. Tech.*, vol. 194, 2016.
21. E. Norman, et al., "Signatures of fissile materials: high-energy γ -rays following fission," *Nucl. Instr. Meth. Phys. Res. A*, vol. 521, pp. 608-610, 2004.
22. R. Firestone et al., Table of Radioactive Isotopes, database version 2/28/99.

3 Second Manuscript

Simulation and Measurement of Delayed γ -rays after Photon-induced Fission

Xianfei Wen, John G. Kavouras, Dante R. Nakazawa, and Haori Yang

*Nuclear Instruments and Methods in Physics Research Section A: Accelerators,
Spectrometers, Detectors and Associated Equipment*

vol. 729, pp. 781-787, 2013

Simulation and Measurement of Delayed γ -rays After Photon-induced Fission

Xianfei Wen^a, John G. Kavouras^a, Dante R. Nakazawa^b, and Haori Yang^a

^a*Nuclear Engineering Program, University of Utah, Salt Lake City, UT 84112, USA*

^b*Canberra Industries, Meriden, CT 06450, USA*

Abstract

Photon-induced fission has been investigated as a method to detect and identify nuclear materials. Although high-energy delayed-fission γ -rays have been considered as a reliable signature for detection of fissionable materials, interference from γ -rays produced as secondary effects from other photonuclear reactions is inevitable. This effect has been studied in distinguishing fissionable materials from non-fissionable materials based on differential delayed γ -ray yields via both simulation and measurements. The energy spectra of delayed-photofission γ -rays carry isotopic information of the target materials. The feasibility of accurate spectrometry measurements in between intense linear accelerator pulses has been demonstrated using three independent spectroscopy systems. The measured delayed γ -rays spectra were then compared with MCNPX simulation results. Through the comparison, this article intends to show the capabilities of the current version of MCNPX in applications of simulating the photofission process.

Keywords: photofission; active interrogation; MCNPX

3.1 Introduction

In homeland security applications, there is an urgent need to find accurate, efficient, and practical ways to stop the smuggling of special nuclear materials. Non-invasive methods to detect and identify nuclear materials are also of great interest to both domestic and international nuclear safeguards societies. Although most nuclear materials of interest naturally emit neutrons and/or γ -rays, the intensity of such spontaneous radiation is normally low, and the energies of the γ -rays are fairly low in most cases. Furthermore, in security applications, it is prudent to assume that the materials are well shielded to circumvent passive detection. Accurate detection and quantification of well shielded nuclear materials using passive techniques is almost impossible [1]. Active interrogation techniques based on high-energy γ -rays or neutrons have been identified as an effective approach [2]. Such active techniques rely on neutrons or high-energy photons to induce nuclear reactions in the object under inspection. Unique signatures following induced fission are then utilized as the basis for detection and identification of nuclear materials [1-24]. On average, two to three energetic prompt neutrons and approximately eight prompt γ -rays are produced in each fission reaction. These radiations are emitted within 10^{-15} s from the time of fission. The fission products continue to emit another six to seven γ -rays and approximately 0.01 to 0.02 neutrons per fission [22]. Although intensities of prompt radiation signals are much stronger, most active interrogation techniques rely on the delayed signals to avoid interference from the probing radiation. Delayed neutrons emitted by neutron-rich fission products are a well-established, reliable, and unique signature from fissionable materials [4-9]. However, they can be easily shielded by

hydrogenous materials, and their yield is fairly low. In addition to delayed neutrons, delayed γ -rays are emitted during the beta decay of many short-lived fission products. Delayed γ -rays have some advantages over the delayed neutron signature. First, the intensity of high-energy delayed γ -rays ($E_\gamma > 3$ MeV) is about 10 times larger than that of delayed neutrons [3]. Second, high-energy γ -rays are highly penetrating; they typically undergo 10-100 times less attenuation than delayed neutrons in hydrogenous materials [2]. Third, emission of intense high-energy delayed γ -rays is unique for nuclear materials; they are not usually observed after the irradiation of benign materials using low-energy photon source, nor are they produced in significant amounts by neutron activation in surrounding materials when neutron energy is less than 10 MeV. Thus, delayed γ -rays and delayed neutrons can complement each other to achieve the greatest sensitivity and accuracy. In our experiments, it is worth noticing that the high-energy neutrons generated by the very high-energy (e.g. 22MeV) bremsstrahlung x-rays can activate major isotopes like O-16 and minor isotopes present in common materials producing gamma rays with energies and time constants similar to the delayed gamma rays. This effect was limited by carefully designed experimental setup and shielding.

When high-energy photons are used as the interrogating source, photofission reactions are induced uniquely in nuclear materials. Fission fragments are normally produced in their excited energy states and de-excite to lower energy levels by emitting delayed neutrons and/or γ -rays. In contrast, neutrons can be produced in both fissionable and non-fissionable materials through neutrons produced by photonuclear reactions. These

neutrons are moderated and eventually absorbed by surrounding materials. Delayed γ -rays will be emitted during this absorption process as well. Thus, for any measurement technique based on delayed γ -rays detection, it is necessary to distinguish delayed fission γ -rays from those created by other nuclear reactions. Detection of delayed γ -rays with energies larger than 3 MeV has been proposed, investigated and implemented as a method for detection of fissionable materials using neutrons [25]. Furthermore, it is important to note that unique γ -ray energy distributions exist for each fissionable isotope [21-22], which can be used to distinguish between the nuclear materials. Delayed γ -ray energy spectra are rich and complex, but it is possible to resolve individual spectral lines with high resolution detectors. The relative intensities of certain lines vary significantly between nuclear isotopes. Based on spectral line intensities, discrimination ratios on the order of 3 have been reported between ^{235}U , ^{239}Pu and ^{238}U [21-22]. Some of the previous work involving the detection of delayed fission γ -rays focused on a so-called “interlace” inspection cycle, consisting of an irradiation period, followed by a cooling off period of a few seconds to minutes, and a counting period of minutes to hours [12-14], [20]. As a result, the measured delayed γ -ray spectra are normally dominated by fission products with medium to long half-lives lasting tens of seconds to minutes. However, the authors and researchers from Idaho Accelerator Center (IAC) as well as others, e.g. J. Stevenson, have independently demonstrated the capability to measure delayed fission γ -rays in between probing linac pulses [15][26][27]. Regarding delayed fission γ -ray energy spectroscopy, our previous study focused on delayed fission γ -rays with energies below 2 MeV [23]. Multiple fission products were identified based on discrete γ -ray lines in this

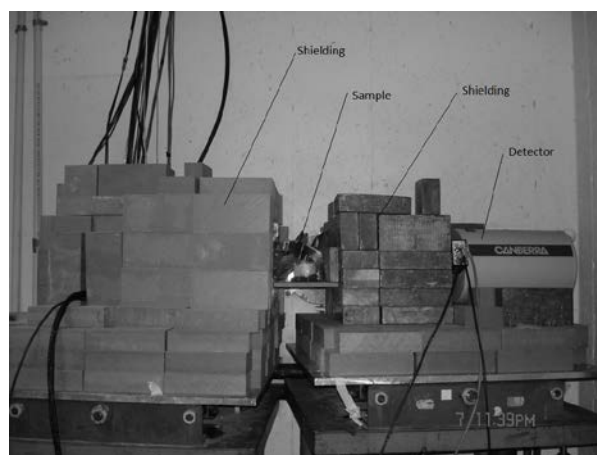
region. Using known fission yield data, fission reaction rate in the sample was predicted. Based on the efficiency-corrected line ratio of the 186 keV and the 1001 keV lines, the sample was confirmed to be a depleted uranium sample [23] [26]. The intensity ratios between delayed γ -ray peaks below 1.5 MeV were thoroughly measured and studied previously [10].

In the work presented here, the authors investigated a method for detection and identification of fissionable materials based on delayed γ -rays after photon-induced fission. Detection and measurement of delayed-fission γ -rays in between linac pulses spectrum were demonstrated as was done in using integrated delayed gamma [27]. Our main objective is to validate the feature of modeling delayed fission γ -rays that was recently added to MCNPX. For this purpose, the measured differential yields and energy spectra of delayed-fission γ -rays were compared with MCNPX simulation results.

3.2 Experimental Setup

The pulsed x-ray beams used in these experiments were produced when high-energy electrons from an electron linac bombard a tungsten radiator. The linac was operated at 15 Hz and the width of each linac pulse was 4 μ s; therefore, the time available for data acquisition between two adjacent pulses was approximately 67 ms. The amount of charge carried by each linac pulse was \sim 150 nC and the electron beam energy was kept at 22 MeV throughout the experiments. The accelerator hall is separated from the experimental cell by a 1.8 m thick concrete wall. Two lead collimators were placed at the ends of the

beam path which passes through this concrete wall. The thickness of these collimators was 15.24 cm and the diameter of the entrance and exit beam opening was 1.27 cm and 3.81 cm, respectively. The first collimator was 61 cm away from the x-ray converter, followed by the second collimator, which was 1.79 m from the first. Within the experimental cell, the targets were positioned ~ 4 m from the x-ray converter directly in the bremsstrahlung beam. At the target position, the bremsstrahlung beam had a diameter of approximately 7.5 cm. The targets consisted of an 18.9 g/cm^2 ^{238}U plate, a 28.8 g/cm^2 lead brick, nine 1 g ^{239}Pu samples, and a 6.0 g/cm^2 ^{232}Th plate. Each detector was positioned perpendicular to the bremsstrahlung beam and shielded with 10.16 cm of lead and 10.16 cm of borated polyethylene. The front of the detector was collimated down to 5.08 cm with lead bricks and the opening was capped with 2.54 cm thick lead to reduce the count rate. The experimental setup is shown below in Figure 3.1.



(a)

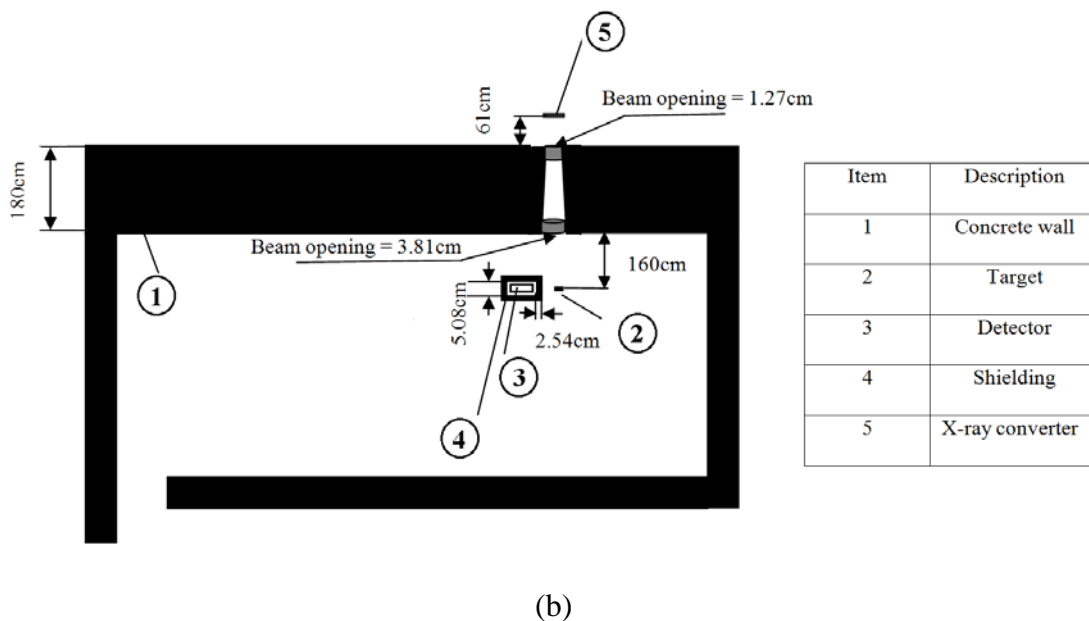


Figure 3.1 (a) A picture of the experimental setup. The left detector assembly is completed, the right one is partially disassembled showing the lead shielding inside. (b) A drawing of the experimental setup.

The γ -ray spectroscopy system used in these experiments is based on two 20% efficient Canberra n-type coaxial high-purity germanium detectors (HPGe, Model number GC2020, the generic size is about 2" by 2"). Three separate signal processing units were used to acquire data: a Canberra LYNX multi-channel analyzer (MCA), a FAST ComTec list mode system and a customized system based on a National Instruments high-speed digitizer. The block diagrams of the three data-acquisition systems are shown in Figure 3.2. The Canberra LYNX MCA was controlled by the Canberra Genie2K software running on a host PC. The data acquisition was set in the 'coincidence mode', which means that the acquisition process was only allowed when the external GATE signal was triggered. In the following experiments, an arbitrary-function generator (Agilent

AFG3021C) was used to produce the GATE signal, triggered by each linac pulse and staying active for 20 ms. Thus, the LYNX MCA was disabled for 20 ms after each linac pulse and started collecting data afterwards until the start of the next pulse. The FAST ComTec list-mode system is an analog data acquisition system which records both energy and time information for each individual γ -ray event.

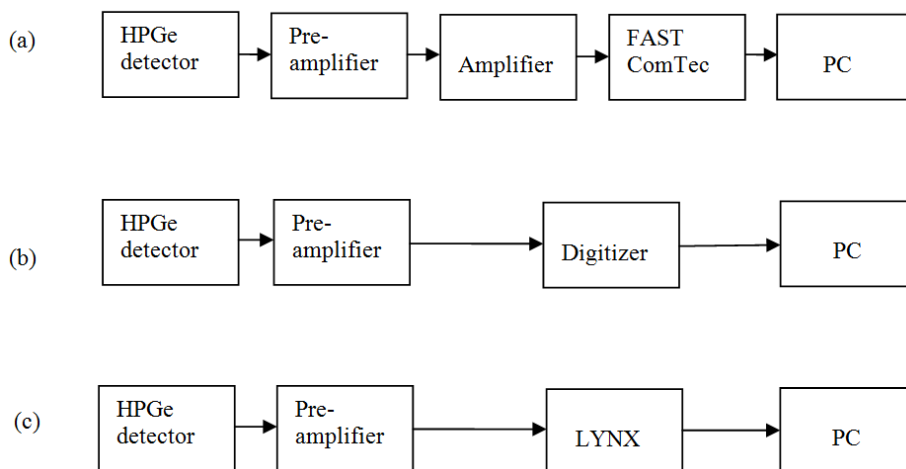


Figure 3.2 The block diagrams of the three data-acquisition systems (a. FAST ComTec list mode system; b. Customized system; c. Canberra LYNX multi-channel analyzer).

The digitizer chosen in this study is a PXIe-5122 module from National Instruments. The key parameters of this digitizer are shown below in Table 3.1. The sampling rate used in the following experiments was 5 Msps. The resolution of the digitizer is 14 bit. A LabVIEW program was developed to stream digitized data onto a hard drive array with full speed at 10 Mb/s. Using this program, one can set operating parameters for the digitizer and control the digitization/recording process. The digitizer is triggered by an external trigger generated by each linac pulse. The length of each data acquisition cycle

was programmed to account for the entire time duration between adjacent linac pulses. Signal processing for the digitized data was performed offline in Matlab® based on trapezoidal filters [28] for optimal balance between throughput rate and resolution and real-time processing. To implement pile-up rejection, two separate signal paths with different shaping parameters were designed. The slow channel was used for accurate energy measurement, while the fast channel was utilized to measure the arrival time for each event. The algorithm was designed such that when a pile-up was detected, the affected pulses were disregarded. This assured a clean spectrum even in ultra-high count rate scenarios ($>10^5$ cps). The output signal from the pre-amplifier of the HPGe detector was passed through these two paths in a parallel manner. Figure 3.3 shows the original signal and the outputs from the fast and slow channels. Using this method, γ -ray energy spectra were reconstructed from the digitized data measured with a calibration source. Using a 0.8- μ s rising edge and 3.2- μ s flat top, the energy spectrum shown in Figure 3.4 was obtained. The same energy spectrum measured with a commercially available MCA (Canberra LYNX) was included for a comparison. It can be observed that the energy resolution achieved using the customized spectrometry system is similar to the results obtained with the commercial MCA system.

Table 3.1 Key parameters of PXIe-5122 digitizer.

Parameter	Value
Form factor	PXI Platform
Resolution	14 bits
Channels	2

Sample rate	100 MHz
Input impedance	50 Ohm, 1 MOhm
On-board memory	256 MB/ch
ENOB	10 bits
Dynamic range	-10 V, 10 V

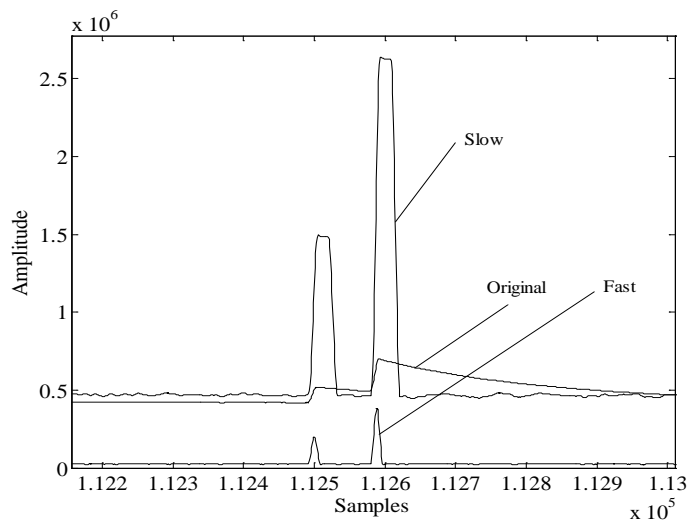


Figure 3.3 Signals from the HPGe detector; the original, fast-, and slow-channel signals are shown.

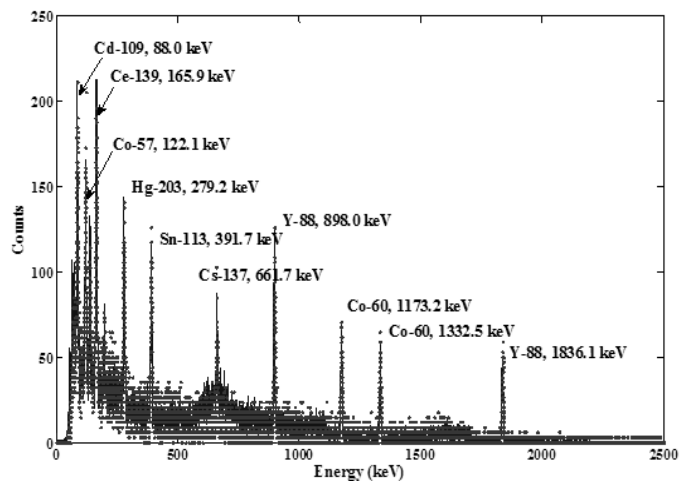


Figure 3.4 Comparison of measured spectra using the customized spectroscopy system (dots) and the commercial MCA (solid line).

In the measurements of differential yields of delayed-fission γ -rays, one of the HPGe detectors was replaced with a 5" by 5" boron loaded liquid scintillation detector, EJ-339A. The key parameters of this boron loaded scintillation detector are shown in Table 3.2 [29]. The EJ-339A was used here as a low resolution gamma ray detector and the presence of boron has no real impact. The output of this detector was a read out using the DAQ system based on a NI PXIe-5122 digitizer as described above.

Table 3.2 Key parameters of the EJ-339A liquid scintillator

Parameter	Value
PMT brand	ETEL 9390KB12
Model number	18028
Boron-10	0.254×10^{22} atoms/cc
Carbon	2.87×10^{22} atoms/cc
Hydrogen	4.98×10^{22} atoms/cc
Density	0.92 g/cc @ 20 °C
Light output	65% anthracene
Decay time	3.7 ns, short component

3.3 Description of the MCNPX Simulation

Having the ability to accurately simulate delayed-fission γ -rays is long-overdue and highly desired for homeland security and nuclear safeguards applications. In this work, it is the authors' intention to demonstrate the capability and limitation of MCNPX 2.7.0 as simulation software that is publicly available. A detailed geometry was created to model

our photofission experiments at IAC, as shown in Figure 3.5. The energy and time of each delayed γ -ray reaching the detector was recorded. However, the pulse-mode bremsstrahlung X-ray source, the platform to support the detector assembly, and background were not included in the simulation.

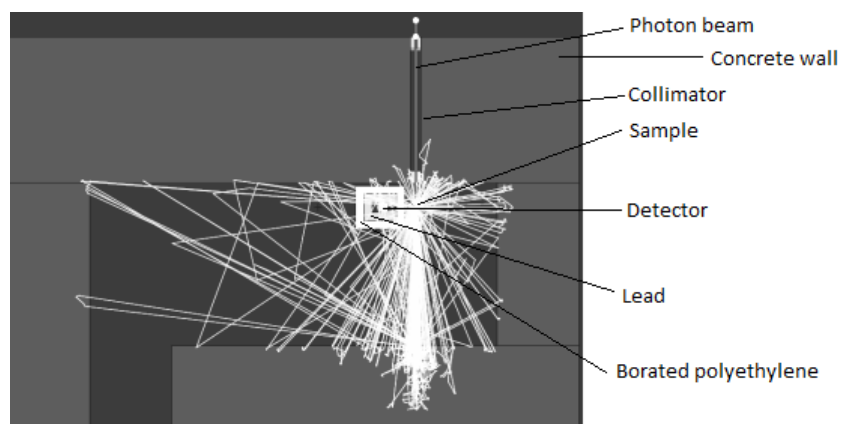


Figure 3.5 The model of the MCNPX simulation.

In 2006, the US nuclear data program released a new photonuclear data library as part of the ENDF/B-VII. Although largely based on the earlier released IAEA photonuclear library, this new data library includes new or improved data for 24 isotopes [30]. The improved actinide data now contains prompt and delayed-fission neutron spectra. Due to the lack of data and theoretical models for photofission, the photofission library used by MCNPX is primarily based on neutron-induced data [31]. The model used by MCNPX assumes that target nuclei will produce fission in the same way, regardless of the type of the incident particle (e.g., a neutron or a photon). To enable the production of photons and neutrons from photofission reactions, the `ispn` entry of the `PHYS:P` card has to be

changed from the default value (ispn=0) to enable photonuclear collision sampling. Also, the fism entry of the PHYS:P card should be set to 1 to ensure that photofission secondaries are sampled only when a photofission event occurs if one prefers analog production of fission neutrons and γ -rays. This is different from the default scenario (fism=0), where high energy photons can produce secondary particles via a photonuclear interaction that is not necessarily from the same reaction. The energies and directions of the secondary particles are averaged over all possible photonuclear interactions (including photofission). This default setting is only correct on average over a large number of interactions, thus its use is not suitable for applications where detail of secondaries production is important, such as coincidence counting. In MCNPX, the physics module requires the ENDF/B-VII photonuclear data library endf7u. The xsdir file for MCNPX installation has to be modified to include this library for MCNPX to access this photonuclear data library. Both the xsdir file and the data library have to be present in the data file directory specified by the environmental variable DATAPATH. Delayed fission γ -rays were recorded using a F4 tally positioned inside the detector cell, where the F4 tally is used to measure flux averaged over a cell. Thus, the detector response is not included in this study. In addition to the settings discussed above, in order to enable photofission interactions and secondary emissions, the DG entry on the ACT card must be set to LINES if individual line-amplitude details are desired. This is crucial to the simulation of delayed-fission γ -ray energy spectra. However, enabling this option makes the simulation significantly slower.

3.4 Results and Discussion

3.4.1 Differential Yields of Delayed γ -rays

Data from the detector was processed with a customized Matlab® script. A pile-up rejection algorithm was also implemented. One important aspect is choosing an appropriate threshold, as demonstrated in Figure 3.6. The amplitude of the threshold should be high enough to avoid double triggering by the overshoot following the major pulse. For example, threshold 2 should be chosen rather than threshold 1 in Figure 3.6. Figure 3.7 shows the differential yields of delayed γ -rays scaled by the product of the total counts and the charge of each pulse as a function of time. For nuclear materials such as DU and ^{232}Th , both neutron-capture γ -rays and delayed-fission γ -rays contribute to the measured signal at early time, less than 20ms after the pulse. On the other hand, there are only contributions from neutron-capture and possibly other reaction γ -rays in the case of non-nuclear materials, such as lead. The liquid scintillator is capable of measuring both neutrons and γ -rays. However, the yield and detection efficiency of photoneutrons and fission neutrons was very low. In addition, since the detector was enclosed with borated polyethylene, the response to thermal neutrons was greatly reduced. It was thus postulated that the output signal comes mainly from γ -rays, which was confirmed in MCNPX simulation later on.

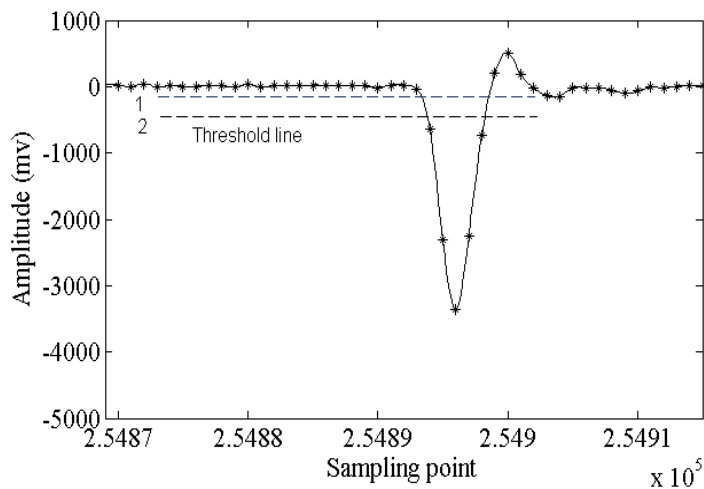


Figure 3.6 Illustration of the threshold line selection. The time width for each sample point is 10 ns.

The differential yields of delayed γ -rays can be utilized to discriminate nuclear materials from non-nuclear materials as shown in Figure 3.7. The counts for the lead sample dropped much faster than the DU and ^{232}Th samples and reached the background level in less than 20 ms after each linac pulse. However, the counts from the DU sample and ^{232}Th sample stayed much higher than that observed in the background long after each linac pulse. The difference in these die-away curves can be explained by the difference in interactions between the interrogation photons and the sample materials. Shortly after each linac pulse, the measured counts from all samples are primarily due to the neutron-capture γ -rays. Fission signatures will always be buried by these much stronger signals. Within the first 5 ms after the turning off a linac pulse, the differential yields of delayed γ -rays from all three samples drop very fast. Afterwards, the delayed γ -ray count rates from the DU and Th samples maintain at a stable significant level until the next linac pulse comes in. However, the delayed γ -ray count rate from the lead sample

drops quickly to the background level. Thus, nuclear materials and non-nuclear materials can be discriminated by the differential yields of delayed γ -rays.

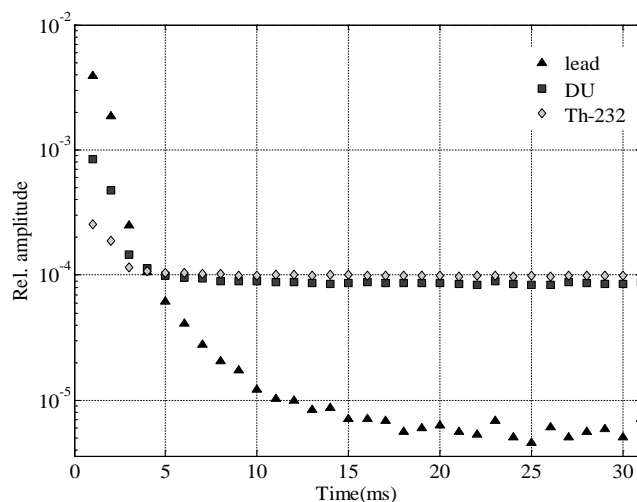


Figure 3.7 The differential yields of delayed γ -rays for DU, ^{232}Th , and lead.

As shown in Figure 3.8, the differential yields of delayed γ -rays from the DU and ^{232}Th samples are similar and agree well with experimental results shown in Figure 3.7. Their value dropped to a stable level several milliseconds after the interrogation pulse. The count rate of delayed γ -rays from the lead sample decreased to a much lower level shortly after the beam was turned off. Data points for the lead sample stopped at about 20 ms as that we didn't take the natural background radiation into account in our MCNPX simulation.

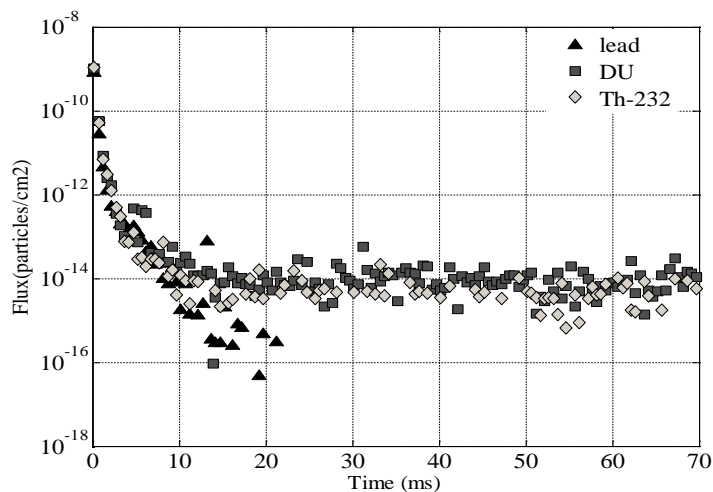


Figure 3.8 Simulated differential yields of delayed γ -rays from the DU, ^{232}Th , and lead samples.

3.4.2 Delayed Fission γ -rays Energy Spectra

Delayed-fission γ -ray spectra from the DU and ^{239}Pu samples were measured with Canberra LYNX MCA and the Fast ComTec list-mode system. DU measurements with both systems were performed simultaneously, lasting 2 hours, with the linac running at 15 Hz. This is equivalent to 1.08×10^5 irradiation cycles and 6156 seconds of counting time. The ^{239}Pu measurement with the Canberra LYNX system lasted 100 minutes, while the measurement with the Fast ComTec system lasted 4 hours. The HPGc detectors and the associated front-end electronics used in these two systems have a much lower throughput rate than the EJ-339A. As shown in Figure 3.9, the system became saturated after an intense linac pulse even though it was well shielded and kept out of the direct beam path. In the following measurements, data from the first several tens of ms after each linac pulse was disregarded (10 ms for DU measurement and 20 ms for ^{239}Pu

measurement). In long measurements, such as those described here, the contribution of the early time delayed gamma rays is still small compared to the dominant seconds and longer life delayed gamma rays, which are built-up from pulse to pulse. Similar results were observed from both systems, as shown in Figure 3.10 and Figure 3.11. Discrete delayed-fission γ -ray lines can be observed throughout the spectra. Due to the small size of the available ^{239}Pu sample, the counting statistics in the high energy region were not suitable for reliable isotope identification.

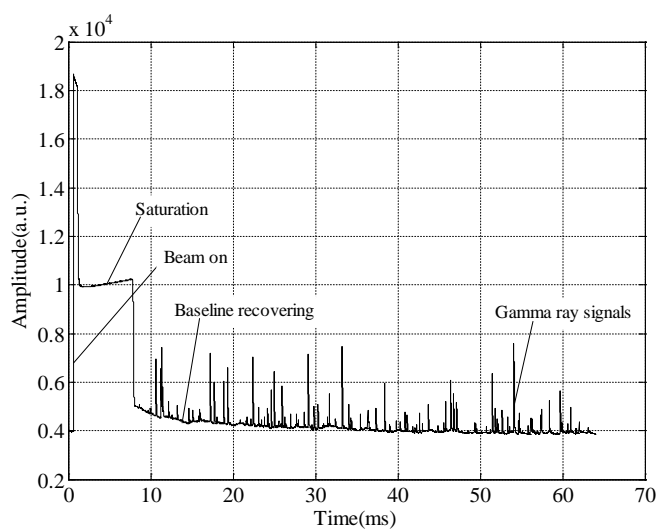


Figure 3.9 The output signal from an HPGc detector between two successive pulses.

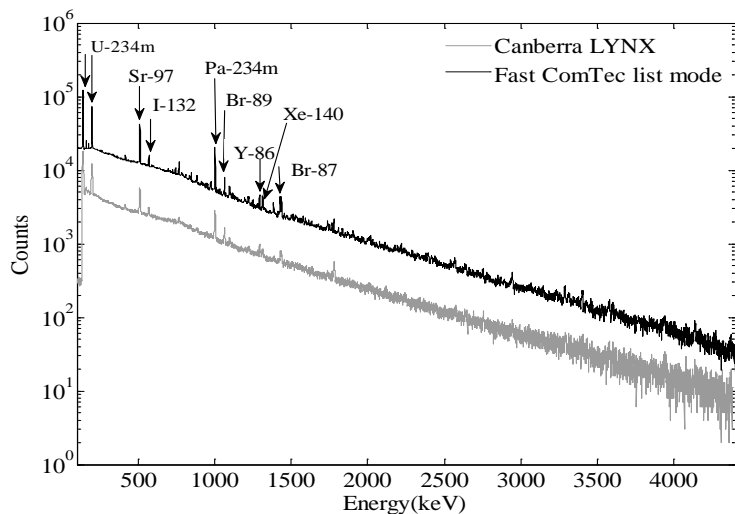


Figure 3.10 Time (>10ms) integrated delayed-fission γ -ray spectra from the DU sample measured with a Canberra LYNX system and a Fast ComTec list mode system.

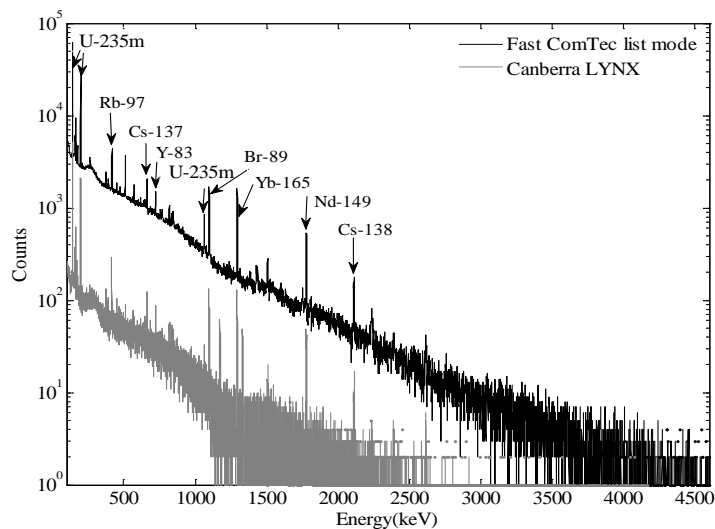


Figure 3.11 Time (>20ms) integrated delayed-fission γ -ray spectra from the ^{239}Pu sample measured with a Canberra LYNX system and a Fast ComTec list mode system.

Using trapezoidal filters as described in the experimental setup section, performance similar to commercial unit was achieved. This system was used to acquire data

simultaneously with the Fast ComTec list-mode system in the ^{232}Th measurements. As shown in Figure 3.12 below, the results from both systems were quite similar. Again, due to the small size of the ^{232}Th sample, counting statistics in the high energy region were poor and isotope identification was not feasible. Nonetheless, this customized DAQ system showed promising capabilities matching the commercial units.

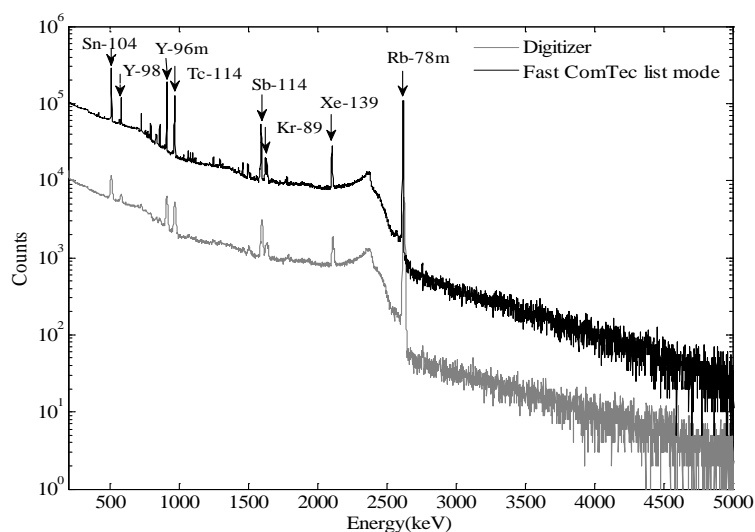


Figure 3.12 Time (>10ms) integrated delayed-fission γ -ray spectra from the ^{232}Th sample measured with a Fast ComTec list mode system and a customized spectroscopy system.

A lead sample was irradiated under the same conditions as the other fissionable materials. The delayed signal from the lead sample was measured with the Fast ComTec list-mode system. A comparison between these results and other fissionable materials is shown below in Figure 3.13. As discussed in the previous section, delayed-fission γ -rays are unique to fissionable materials. Although delayed γ -rays can also be produced in the lead sample due to the production of photoneutrons and subsequent absorption of these

neutrons via the (n, γ) reaction, these neutron-capture γ -rays die away much faster than fission γ -rays. By removing γ -rays recorded within 10 ms of each linac pulse, the interference from neutron-capture reactions can be greatly alleviated. As shown in Figure 3.13, delayed γ -rays with energies above 3 MeV are truly a unique signature for fissionable materials under these counting conditions.

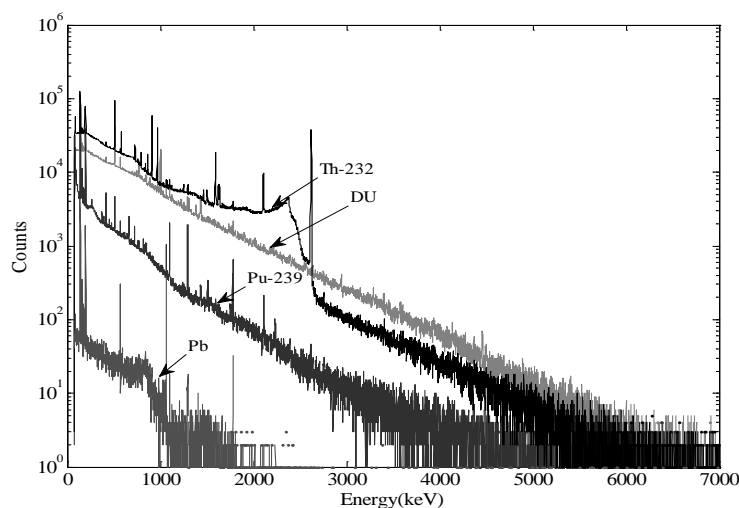


Figure 3.13 Time integrated delayed-fission γ -rays from various samples measured with a Fast ComTec list mode system (Note: data from the first 10 ms after each linac pulse was disregarded).

In Figure 3.14 and Figure 3.15, results in the energy range from 2.5 MeV to 4.2 MeV from MCNPX are compared with the spectra measured from two separate DAQ systems. Multiple peaks, 2570 keV ^{89}Rb , 2640 keV ^{138}Cs , 2942 keV ^{98}Y , 2946 keV ^{106}Tc , 3288 keV ^{97}Y , 3576 keV ^{95}Y , and 3600 keV ^{91}Rb , from delayed-fission γ -rays can be identified in both measured spectra. MCNPX 2.7.0 successfully predicted most of these peaks for DU sample. However, some notable peaks in the measured spectra, 2869 keV ^{136}I , 2941

keV ^{98}Y , and 3228 keV ^{98}Y , are not observed in the experimental measurements. Reedy et al. generated delayed-fission γ -ray spectra using fission yield from ENDF/B-VII.0 and line emission data from ENSDF [15]. Similar discrepancies from measured results were reported. This provides evidence that the limitations of the current simulation package are attributed to the availability and accuracy of photofission data.

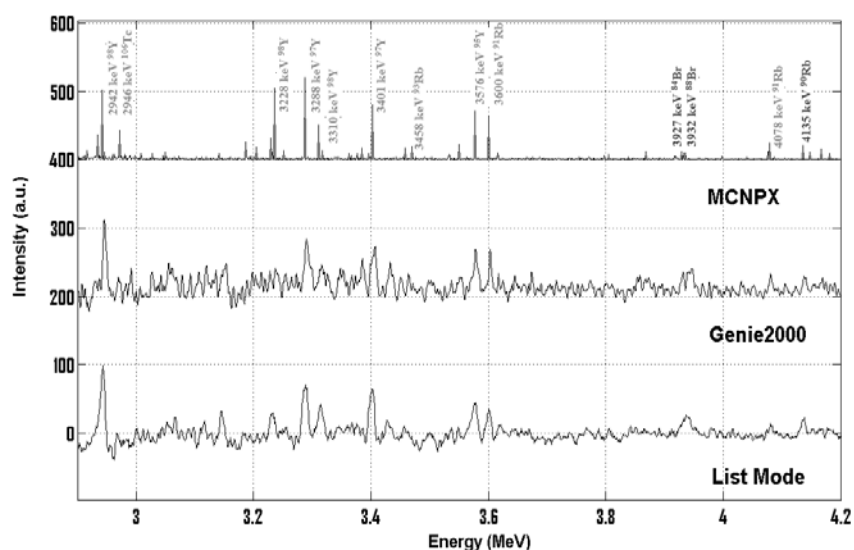


Figure 3.14 Comparison of measured and simulated delayed-fission γ -ray spectra above 3 MeV for DU sample.

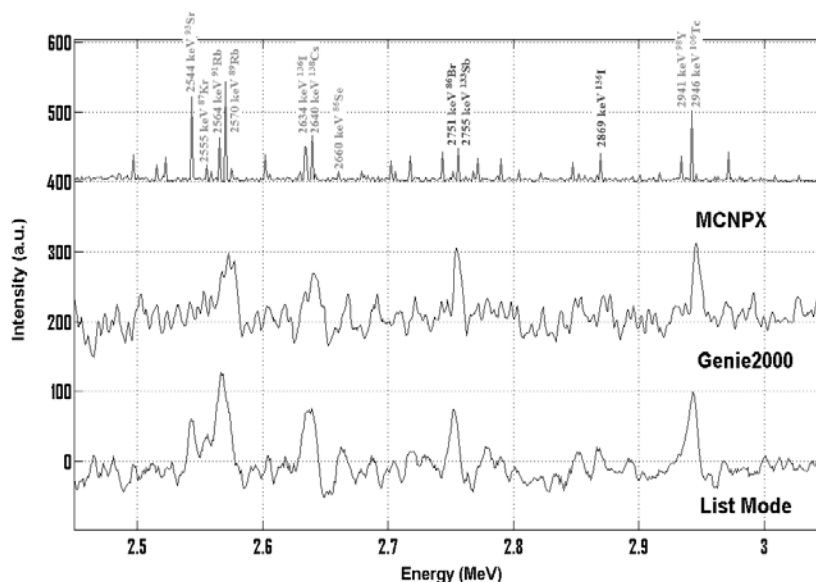


Figure 3.15 Comparison of measured and simulated delayed-fission γ -ray spectra from 2.5 MeV to 3 MeV for DU sample.

3.5 Conclusion

This work demonstrated that high-energy delayed γ -rays can be used as signature signals for detection and identification of nuclear materials. Such γ -rays were successfully measured between linac pulses using three independent acquisition systems. Interference from neutron-capture γ -rays can be greatly alleviated when time discrimination is applied. Although the gross count rate alone is a straightforward way to distinguish fissionable materials from non-fissionable materials, discrete delayed-fission γ -rays, though very weak especially for $>3\text{MeV}$, could help in performing isotopic discrimination. In addition to commercially available systems, a customized DAQ system has been developed based on a high-speed digitizer. This system provided the capability and flexibility to improve data throughput, matching that of the commercial units. Both

the total yield and line emission intensity of delayed fission γ -rays were simulated using MCNPX 2.7.0. Good agreement was observed between simulation and experimental results. However, the simulation did predict some major γ -ray energy lines that were not observed in the experimental measurements due to the limited availability and accuracy of photofission data.

The technology described in this paper can be utilized for potential applications in both homeland security and nuclear safeguards. In homeland security applications, γ -ray detection efficiency has to be greatly improved for high throughput and high sensitivity systems. Since gross counting with time and energy discrimination can produce unique fission signatures, detectors with high efficiency and moderate energy resolution are ideal, such as scintillation detectors. Discrete delayed-fission γ -ray line intensities can be used for isotope identification, which is critical in nuclear safeguard applications. HPGe detectors are still the best option for gamma spectrometry measurements.

Acknowledgement

The authors would like to thank Dr. Alan Hunt from Idaho Accelerator Center for the use of the list-mode data acquisition system. The authors would also like to thank Dr. Hunt for providing and helping with the program to process list-mode data. This research is being performed using funding received from the DOE Office of Nuclear Energy's Nuclear Energy University Programs.

References

1. D. Chichester, et al., "Estimation of the performance of Multiple Active Neutron Interrogation Signatures for Detecting Shielded HEU," *IEEE Nuclear Science Symposium Conf.*, 2012.
2. T. Gozani, "Active Nondestructive Assay - Principles and Applications," NUREG/CR-0602, 1981.
3. A. Hunt, et al., "Fission Signature Interferences in Active Interrogation Techniques Utilizing High-Energy Bremsstrahlung," *IEEE Nuclear Science Symposium Conf.*, 2012.
4. J. Jones, et al., "Photofission-based, nuclear material detection: technology demonstration," Idaho Nat. Lab., Idaho Falls, ID, Rep. 02-01406, Dec. 2002.
5. J. Jones, et al., "Pulsed photonuclear assessment (PPA) technique: CY04 year-end progress report," Idaho Nat. Lab., Idaho Falls, ID, Rep. 05-02583, Feb. 2005.
6. J. Jones, et al., "Photonuclear-based, nuclear material detection system for cargo containers," *Nucl. Instr. Meth. Phys. Res. B*, vol. 241, pp. 770-776, 2005.
7. D. Norman, et al., "Inspection applications with higher electron beam energies," *Nucl. Instr. Meth. Phys. Res. B*, vol. 241, pp. 787-792, 2005.
8. J. Jones, et al., "Detection of shielded nuclear material in a cargo container," *Nucl. Instr. Meth. Phys. Res. A*, vol. 562, pp.1085, 2006.
9. D. Norman, et al., "Time-dependent delayed signatures from energetic photon interrogations," *Nucl. Instr. Meth. Phys. Res. B*, vol. 261, pp. 316, 2007.
10. C. Hollas, D. Close, and C. Moss, "Analysis of fissionable material using delayed gamma rays from photofission," *Nucl. Instr. Meth. Phys. Res. B*, vol. 24, pp. 503-505, 1987.
11. D. Beddingfield and F. Cecil, "Identification of fissile materials from fission product gamma-ray spectra," *Nucl. Instr. Meth. Phys. Res. A*, vol. 417, pp. 405-412, 1998.
12. M. Gmar and J. Capdevila, "Use of delayed gamma spectra for detection of actinides (U, Pu) by photofission," *Nucl. Instr. Meth. Phys. Res. A*, vol. 422, pp. 841-845, 1999.

13. F. Carrel, et al., "Identification of actinides inside nuclear waste packages by measurement of fission delayed gammas," *IEEE Nuclear Science Symposium Conf. Rec.*, pp. 909-913, 2006.
14. F. Carrel, et al., "Identification and differentiation of actinides inside nuclear waste packages by measurement of delayed gammas," *IEEE Trans. Nucl. Sci.*, vol. 57, pp. 2862, 2010.
15. E. Reedy, S. Thompson, and A. Hunt, "The detection of delayed gamma-rays between intense bremsstrahlung pulses for discriminating fissionable from non-fissionable materials," *Nucl. Instr. Meth. Phys. Res. A*, vol. 606, pp. 811-815, 2009.
16. M. Kinlaw and A. Hunt, "Fissionable isotope identification using the time dependence of delayed neutron emission," *Nucl. Instr. Meth. Phys. Res. A*, vol. 562, pp. 1081-1084, 2006.
17. S. Kahane, et al., "Photofission of U-238 with neutron-capture gamma rays," *Phys. Rev. C*, vol. 32, pp. 1944-1955, 1985.
18. D. Dore, et al., "Delayed neutron yields and spectra from photofission of actinides with bremsstrahlung photons below 20 MeV," *J. Phys. Conf. Ser.*, vol. 41, pp. 241, 2006.
19. R. B. Walton, et al., "Delayed Gamma Rays from Photofission of U-238, U-235, and Th-232," *Phys. Rev. B*, vol. 134, pp. 824-832, 1964.
20. M. Gmar, et al., "Assessment of actinide mass embedded in large concrete waste packages by photon interrogation and photofission," *Appl. Radiat. Isot.*, vol. 63, pp. 613, 2005.
21. K. Baumung, et al., "Investigations into nondestructive safeguards techniques," in *Proc. IAEA Symp. Safeguards Tech.*, Karlsruhe, Germany, vol. 2, pp. 192, 1970.
22. R. L. Branblett, et al., "Application of photo-induced reactions to nuclear materials safeguards problems," Gulf General Atomic Inc., San Diego, CA, Rep. GA-9614, 1969.
23. D. Wehe, et al., "Observation of ^{238}U photofission products," *IEEE Trans. Nucl. Sci.*, vol. 53, no. 3, pp. 1430, 2006.
24. H. Yang, D. Wehe, and D. Bartels, "Spectroscopy of high rate events during active interrogation," *Nucl. Instr. Meth. Phys. Res. A*, vol. 598, pp. 779-787, 2009.

25. D. R. Slaughter, et al., "The nuclear car wash: A system to detect nuclear weapons in commercial cargo shipments," *Nucl. Instr. Meth. Phys. Res. A*, vol 579, pp. 349-352, 2007.
26. H. Yang, "Active interrogation methods for detection of special nuclear material," Ph.D. dissertation, Dept. Nucl. Eng. Radiol. Sci., Univ. Michigan, Ann Arbor, MI, 2009.
27. J. Stevenson, et al., "Linac based photofission Inspection system employing novel detection concepts," *Nucl. Instr. Meth. Phys. Res. A*, vol. 652, pp. 124-128, 2011.
28. V. T. Jordanov, et al., "Digital techniques for real-time pulse shaping in radiation measurement," *Nucl. Instr. Meth. Phys. Res. A*, vol. 353, pp. 261-264, 1994.
29. EJ-339A Data sheet, www.eljentechnology.com.
30. J. Verbeke, C. Hagmann, and D. Wright, "Simulation of neutron and gamma ray emission from fission and photofission," Lawrence Livermore Nat. Lab., Livermore, CA, Rep. UCRL-AR-228518, 2010.
31. MCNPX Version 2.7.0 User's Manual, Los Alamos Nat. Lab., Los Alamos, NM, 2011.

4 Third Manuscript

Evaluation of a modified HPGe preamplifier for high-rate spectroscopy measurements in
a pulsed photonuclear environment

Xianfei Wen, Dante Nakazawa, Mat Kastner, Jason Pavlick, Haori Yang

Nuclear Technology

vol. 194, 2016

Evaluation of a modified HPGe preamplifier for high-rate spectroscopy measurements in
a pulsed photonuclear environment

Xianfei Wen¹, Dante Nakazawa², Mat Kastner², Jason Pavlick², Haori Yang^{1*}

¹*School of Nuclear Science and Engineering, Oregon State University, Corvallis, OR
97331, USA*

²*Canberra Industries, Meriden, CT 06450, USA*

Abstract

Pulsed photonuclear techniques are commonly used in homeland security and nuclear safeguards applications to achieve enhanced detection sensitivity. For example, photoneutrons generated by a pulse-mode linac are commonly utilized to produce characteristic capture gamma rays for the detection of nitrogen-rich explosives. Recently, in an effort to develop innovative systems with increased sensitivity to detect diversion and prevent misuse, the authors proposed to assay used nuclear fuel for its plutonium content using photofission technique, in support of nuclear material management in the U.S. fuel cycle. Passive spectroscopy measurements in the presence of intense background from fission products could be very difficult. Focusing on high-energy delayed gamma rays emitted by short-lived products from photofission presents a much more promising solution. However, as discovered in our study, a commercially available standard HPGe preamplifier can be easily saturated for tens of milliseconds after each linac pulse. This greatly reduces the live time of the system especially when the linac repetition rate is high. On the other hand, although significantly reduced by increasing the

lower level threshold, the input count rate can still easily reach 106 counts per second (cps). Developing a gamma spectroscopy system that can handle such high count rate has been a major challenge.

In this work, a commercial HPGe preamplifier was modified to reduce the saturation time and tail time to improve its high-rate performance in a pulsed photonuclear environment. Results of the modifications were evaluated via both simulations and experiments and proven to be effective without significant degradation of energy resolution. The FET and feedback components were first moved to the warm side to enable the modifications. The saturation time of the preamplifier following a linac pulse was greatly reduced by decreasing the value of the feedback resistor. The effect of reducing the tail time of the output signal was also studied. Traditional trapezoidal shaping approach was then employed to study the impact of the modifications on energy resolution.

Keywords: preamplifier; high-rate; digital pulse processing; photofission

*Corresponding author.

Address: School of Nuclear Science and Engineering, Oregon State University, Corvallis,
OR 97331, USA.

E-mail: haori.yang@oregonstate.edu (H. Yang).

4.1 Introduction

Gamma spectroscopy systems with high-rate capability are needed for homeland security and nuclear safeguards applications. For example, during an assay on spent nuclear fuel assemblies, the input gamma ray count rate can reach 10^6 cps or higher even after a few years of cooling. Many efforts are being devoted to develop high-throughput high-resolution gamma spectroscopy systems for such measurements [1-4]. The ADONIS system developed by CEA was designed to balance the trade-off between energy resolution and throughput rate, using a bimodal Kalman smoother [1-2]. The highlight was the introduction of a hidden semi-Markov variable, allowing ultra-high throughput rate with little degradation in energy resolution. A team from Pacific Northwest National Laboratory (PNNL) demonstrated that good energy resolution (~ 8 keV at 662 keV) and high throughput (39%) could be achieved at an input rate as high as 1.03×10^6 cps [3]. To accomplish this, seven time-invariant trapezoidal filters were implemented in parallel. For best energy resolution, the filter with the longest rise time without causing pile-up was used for energy measurement.

On the other hand, to enhance sensitivity, pulsed photonuclear techniques are often utilized. For example, Idaho National Laboratory (INL) developed a nondestructive evaluation (NDE) technique based on photoneutrons to detect nitrogen-rich explosives. Their system utilized a pulsed, high energy (2 to 12 MeV) linac and an HPGe-based gamma-ray spectroscopy system [5-6]. Highly penetrating bremsstrahlung x-rays were produced by the linac at a repetition rate of 47 Hz. Interrogating neutrons were generated

in a photoneutron target (e.g. D_2O). Characteristic gamma rays were emitted upon absorption of interrogating neutrons by the object-of-interest. Gamma spectrometry was then performed between linac pulses. To allow a fast recovery after each accelerator pulse, the transistor reset preamplifier was modified in their detector system. Photonuclear techniques have also been studied for detection and quantification of special nuclear materials. The low intensity of spontaneous emission and the low energies of decay γ -rays make passive nondestructive assay difficult under many circumstances. Photonuclear techniques have been identified as an effective solution [7-12]. Unique signatures following induced fission could be employed as the basis for detection and identification of nuclear materials [13-14].

To support nuclear material management in U.S. fuel cycle, systems with enhanced sensitivity are needed to assay Pu content in spent nuclear fuel. High-resolution gamma spectroscopy is a well-established solution for such isotope identification tasks. However, passive counting is rendered extremely challenging due to the intense radiation background from fission products even after prolonged cooling (gamma rays below 3 MeV, predominately from long-lived isotopes). To provide a viable solution, the authors proposed to utilize photofission technique and perform spectroscopy of high-energy delayed gamma rays from short-lived fission products. This would allow us to reduce background count rates by focusing on the high-energy range. To successfully implement this idea, we need to address two major issues: system recovery from the intense interrogating source and high input count rate in between the interrogating pulses.

Firstly, in our recent study, it was observed that even with several inches of shielding with lead, the spectroscopy system could still be paralyzed for tens of milliseconds after each linac pulse [15]. Valuable information about the sample can be obtained if the system is able to recover faster, mainly from short-lived fission products with half-lives in the range of several tens of milliseconds, such as ^{100}Rb (half-life: 53 ms, fission yield: 3.48×10^{-4} /fission, energy: 130 keV) and ^{102}Sr (half-life: 68 ms, fission yield: 1.73×10^{-4} /fission, energy: 1104 keV) [16]. In addition, when a high linac repetition rate is implemented, a short recovery time could significantly improve the live time of the system. For example, a linac repetition rate of 125 Hz was chosen by a group at INL for detection of shielded nuclear materials in cargo containers [17]. At such a high linac repetition rate, an off-the-self preamplifier would be paralyzed for approximately 70% of the time. Minimizing the saturation time with modifications presented in this study will improve the collection of useful data otherwise lost. Secondly, the incoming rate during an assay on spent nuclear fuel could still easily reach over 10^6 cps. At such high count rate, the exponential tail of the resistive feedback preamplifiers, with time constants on the order of tens of μs , can contribute to significant baseline shift. Besides advanced signal processing techniques [1-4, 18], approaches to reduce the tail time of the preamplifier signal can be beneficial in such high-rate applications, as will be further discussed below.

4.2 Modifications to the Preamplifier

Two Canberra p-type coaxial HPGe detectors with relative efficiency of 40% were used in our study. The model number of the detectors was GC4020. The crystal size was roughly 2.4" OD by 2.3" height. One detector was kept unmodified and served as a reference. Figure 4.1 shows a comparison between the standard and the modified preamplifier. In the modified preamplifier, the FET and feedback components were first moved outside of the cryostat to make the modifications practicable. The FET was placed in a tulip cup heat-sink on the preamplifier board, and the feedback components were soldered to the FET (see left image in Figure 4.1). A protection diode that is usually connected to the FET was also omitted in order to prevent additional warm-side leakage current. A block diagram of the preamplifier is shown in Figure 4.2. A schematic drawing of the preamplifier is given in Figure 4.3. Modification to the feedback resistor, R_f , varied the output signal from the first stage of the preamplifier unit, i.e. the charge-sensitive integrator. The second stage, i.e. the differentiator and Pole/Zero (P/Z) network, had to be modified to achieve perfect pole/zero cancellation. The third stage (i.e. the amplifier), together with the second, determined the amplitude and shape of the final output signal. These modifications and their impact on system performance are further discussed in detail below.

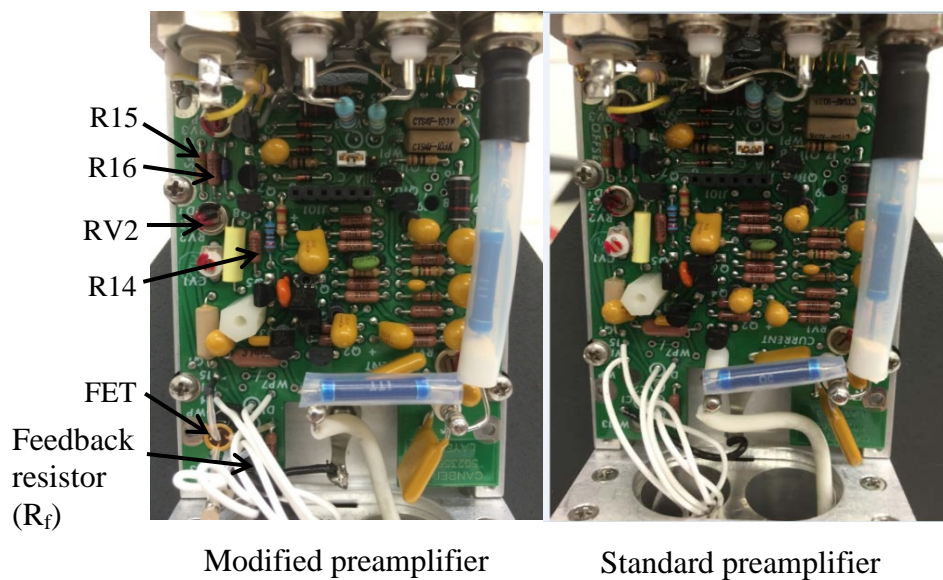


Figure 4.1 Illustration of the components of a standard preamplifier to be modified.

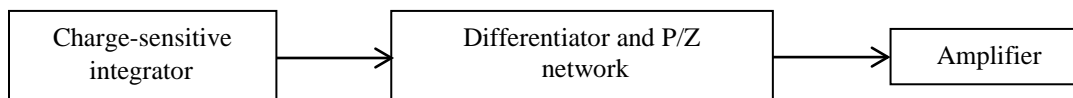


Figure 4.2 A block diagram of the functionality of a typical RC-feedback commercial preamplifier unit.

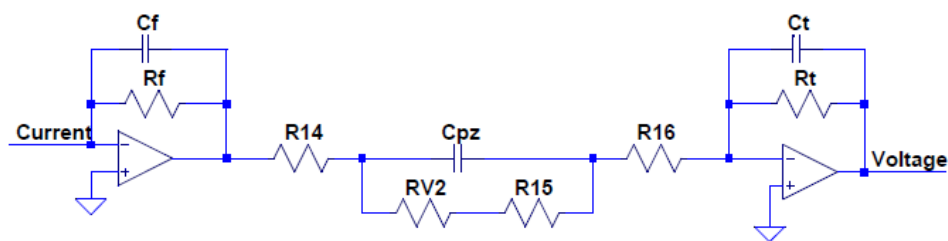


Figure 4.3 A schematic drawing of a preamplifier with RC-feedback.

4.2.1 Modification to the Feedback Resistor

It is well known that the energy rate limit of a RC-feedback preamplifier is a function of the feedback resistor value and the dynamic range of the output voltage from the integrator. The energy rate can be derived from the equation below, provided the value of

$$\text{Energy rate} \left(\frac{\text{MeV}}{\text{s}} \right) \times 10^6 \left(\frac{\text{eV}}{\text{MeV}} \right) \times \frac{1}{W(\text{eV})} \times 1.6 \times 10^{-19} (\text{C}) \times R_f (\Omega) = V(\text{Volt})$$

feedback resistor (R_f), the energy required to create an electron-hole pair (W), and the voltage range (V).

Recently, a group from PNNL demonstrated improved energy rate by changing the output voltage limit from -24 V to -100 V [3]. A different approach was taken in this work, focusing on the feedback components of the charge-sensitive stage. The value of the feedback resistor was reduced from 2 G Ω to 0.5 G Ω . In both photofission experiments and following LTSpice simulations, it was proven that the smaller feedback resistor value substantially reduced the saturation time after each large energy depositions when the linac pulses are delivered to the sample.

This saturation time following each linac pulse was first evaluated during our photofission experiments at the Idaho Accelerator Center (IAC). A schematic drawing of the experimental setup is shown in Figure 4.4, displaying the unmodified and modified detectors. The setup was symmetrical about the beam, so that both detectors were

exposed to the same radiation field. The repetition rate of the linac was set at 10 Hz. Each linac pulse was 4 μ s wide and carried around 86 nC of charge. The bremsstrahlung x-rays exiting from the beam port had a maximum energy of 22 MeV. The beam diameter was about 7.5 cm at the target position. A 3 g plutonium sample (95% ^{239}Pu and 5% ^{240}Pu) was placed on the centerline of the x-ray beam, 47 cm away from the beam port. The HPGe detectors were located 21 cm away from the beam line and shielded with 10 cm lead. The centerlines of the detectors were perpendicular to the beam. The signals from the preamplifiers were digitized with a National Instruments PXIe-5122 digitizer with 14-bit resolution at sampling rate of 30 MSPS. The digitized signals were then transferred to a PC for off-line processing in Matlab. Figure 4.5 shows the measured signals from both the standard and the modified preamplifiers. The measured saturation time of the modified preamplifier following a linac pulse was 2.5 ms, while it took the standard preamplifier much longer to recover (around 5.7 ms).

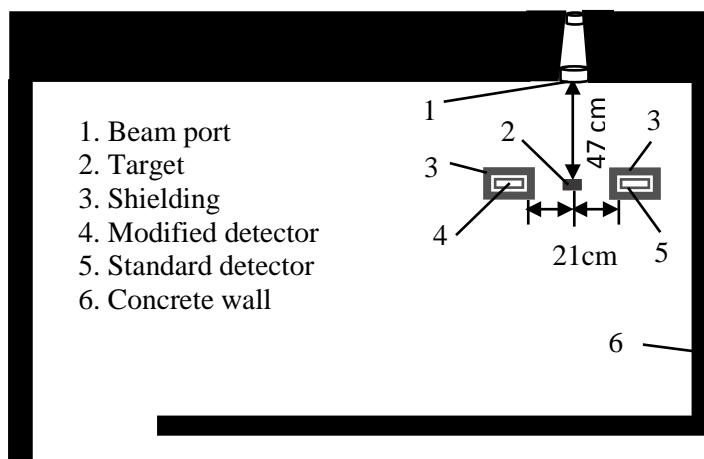


Figure 4.4 A schematic drawing of the experimental setup for testing the effect of feedback resistor on saturation time.

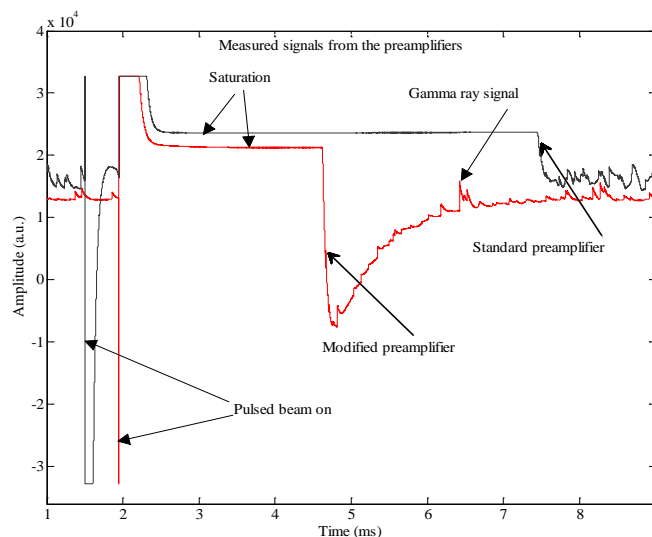


Figure 4.5 Measured signals from the preamplifiers in the photofission environment.

A model of the preamplifier was created in LTSpice and used to study the system performance. In the simulations, a $4 \mu\text{s}$ wide current source of 2.1×10^{-5} Amp starting at time 1 ms was setup to represent the large energy injection observed from the linac pulses seen at IAC. The amplitude of the current source was empirically chosen so that the simulated saturation time of the standard preamplifier was similar to those measured in the experiments. The stop time and maximum time step in the transient simulation mode of LTSpice were set at 20 ms and $10 \mu\text{s}$, respectively. The large undershoot that was observed in the measurements of the modified detector (red curve in Figure 4.5) was reproduced in the simulated output (blue curve in Figure 4.6) with slight modifications to the pole-zero network components. The simulated saturation time of the modified preamplifier is 1.5 ms (see Figure 4.6), which is smaller than the measured value of 2.5 ms. The discrepancy is most likely due to approximations made in the LTSpice model,

such as the characteristics and parameters of components (e.g. the FET), and the simplification of the linac beam as a single current source. However, the comparison between simulation and experimental results of both unmodified and modified detectors yielded valuable qualitative validation that the modifications made could increase signal collection after saturation.

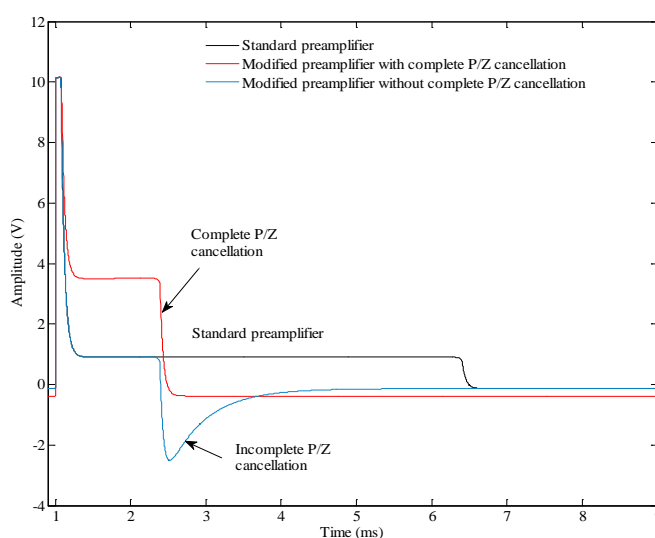


Figure 4.6 Comparison between the simulated signals from the modified preamplifier with complete and incomplete P/Z cancellations.

4.2.2 Modification to the Tail Time

The modification to reduce the tail time of the final output signal and its impact on baseline shift are described in detail below. In this work, the tail time was reduced from 50 μs to 10 μs . A comparison between the signals before and after this modification is illustrated in Figure 4.7. During the measurement, a ^{137}Cs source was placed close to the

detectors to achieve an input count rate of 20 kcps. The NI PXIe-5122 system was used to acquire the signals from the preamplifiers at sampling rate of 50 MSPS. As shown in Figure 4.7, the signal from the modified preamplifier decays much faster than that from the standard preamplifier. For simplicity, the reduction of the tail time was achieved by changing the values of resistors R14 and R16 from 499 Ω to 99 Ω . This approach is easy to implement, however, it dramatically increases the DC gain and reduces the effective input dynamic range. In the future, the same reduction of the tail time can be achieved by reducing the value of the capacitor C_{pz} in the P/Z network, without affecting the DC gain. The effect of the reduced tail time (10 μ s) by changing the capacitor on baseline shift was studied with LTSpice simulations. The stimulus source was a train of current pulses at rate of 5×10^6 cps, each of which simulated the charge produced by gamma ray of 1 MeV. The offset time of the stimulus source was 0.014 ms. The rise time and fall time of each current pulse were both set at 5 ns. The amplitude of a pulse was 511 nA with a duration of 100 ns. The simulation mode in LTSpice was set at transient to perform a time-domain computation. As shown in Figure 4.8, the baseline of the output signal from the standard preamplifier increases at a much higher rate than that from the modified one and reaches the saturation level within 0.046 ms. Instead, the baseline for the modified preamplifier is only shifted to 3.2 V. Significant reduction of baseline shift could be beneficial to many high-rate applications. For example, in spent nuclear fuel assay applications, the input count rate can often reach 10^6 cps or higher. Thus a preamplifier with nominal tail time (i.e. 50 μ s) would be easily saturated. Instead, as a result of the reduced tail time, the modified preamplifier could potentially be used to perform spectroscopy measurement

and provide valuable information about spent fuel assemblies. In addition, the reduction of baseline shift can also be beneficial when a digitizer with small input range is utilized to acquire waveforms from preamplifiers. For example, a NI PXI-5152 digitizer (input range: ± 5 V) can be used to acquire data from the modified preamplifier at input count rate of 5×10^6 cps. However, the digitizer could be saturated due to the large baseline shift observed from the standard preamplifier.

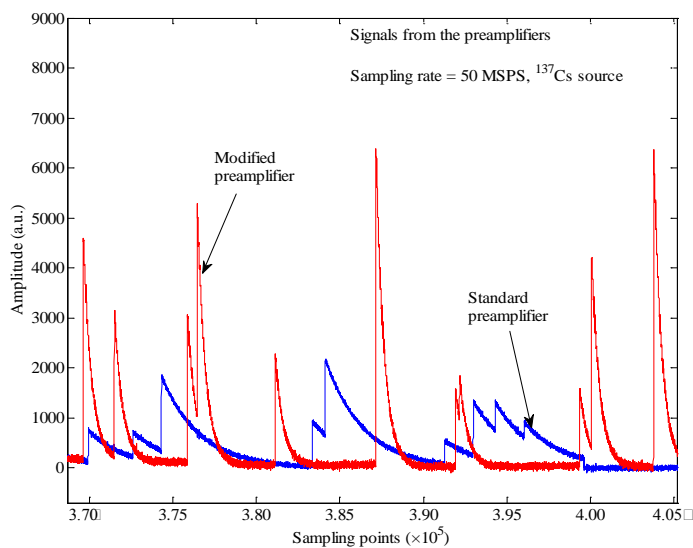


Figure 4.7 Comparison between signal waveforms measured with NI PXIe-5122.

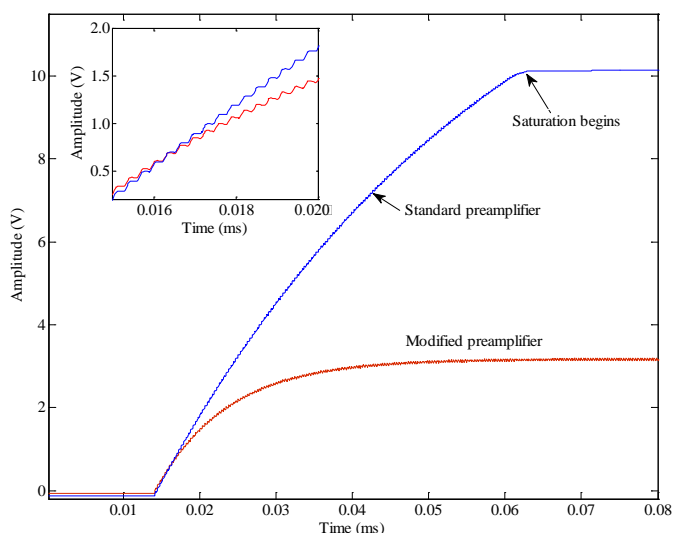


Figure 4.8 The effect of reduced tail time on baseline shift simulated in LTSpice.

4.3 Evaluation of Energy Resolution after the Modifications

The energy resolution of the system after the preamplifier modifications was evaluated using the traditional trapezoidal shaping methods [19-20] in Matlab. In these measurements, the input count rate from a ^{137}Cs source was kept close to 20 kcps by adjusting the source-to-detector distance. The NI PXIe-5122 system was used to acquire the signals with 14-bit resolution at sampling rate of 50 MSPS. The digitized data was transferred to a PC for off-line signal processing. As an illustration of trapezoidal filtering, Figure 4.9 shows the energy signal shaped with a long shaping times (5.6 μs rise time, 0.8 μs flat top time) to perform energy measurement and the time signal with shorter shaping times (0.1 μs , 0 μs) used to detect the time-of-arrival of each event and perform pile-up rejection. To reduce the impact of ballistic deficit on energy resolution, the flat top time of the trapezoidal filter needs to be longer than the charge collection time [21].

To find the appropriate flat top time empirically, the charge collection time for each event was first estimated using the recursive algorithm for digital pulse shaping [19]. The rise and flat top times used in the algorithm were set at $0.11\ \mu\text{s}$ and $0\ \mu\text{s}$, respectively. As shown in the inset of Figure 4.10, the time the fast channel takes to reach its maximum after crossing the threshold is considered an estimation of the charge collection time. The result was used to build the histogram shown in Figure 4.10. Based on this histogram, the flat top time was chosen to be $0.8\ \mu\text{s}$ to ensure complete charge collection regardless of the actual charge drifting process. This value was used in all the energy spectra reconstruction in following discussion. A local minimum collection time around $240\ \text{ns}$ is observed in Figure 4.10. The observation is likely due to the low sampling rate (i.e. 50 MSPS) and the simplified approach to determine the collection time. In the slow channel for energy measurement, different rise times were used respectively for the standard and modified preamplifiers to optimize energy resolution. Figure 4.11 shows the energy resolution obtained using various rise times. As shown in Figure 4.11, the optimal rise times for the standard and modified preamplifiers were $8\ \mu\text{s}$ and $6\ \mu\text{s}$, respectively. The energy spectra reconstructed at the optimal rise times are present in Figure 4.12. There was no significant degradation in resolution ($2.4\ \text{keV}$ vs $2.2\ \text{keV}$ @ $662\ \text{keV}$) as a result of moving the FET to the warm side and reducing the feedback resistor and tail time. The authors believe that the smaller feedback resistor ($0.5\ \text{G}\Omega$ vs $2\ \text{G}\Omega$) exposed in room temperature environment is the main cause of the shift of the optimal rise time. The equation used to explain the shift is presented as follows [22]:

$$\left(\omega_{parallel}\right)^2 \propto \left(I_D + \frac{2kT}{R_f}\right) \times T_s$$

Where I_D is the total detector current, k is the Boltzmann constant, T is the temperature of the feedback resistor, R_f is the value of the feedback resistor, T_s is the rise time in the trapezoidal shaping. As shown in the equation above, extra parallel noise from the feedback resistor needs to be compensated by a short shaping time to obtain the best energy resolution, which leads to the optimal rise time shift.

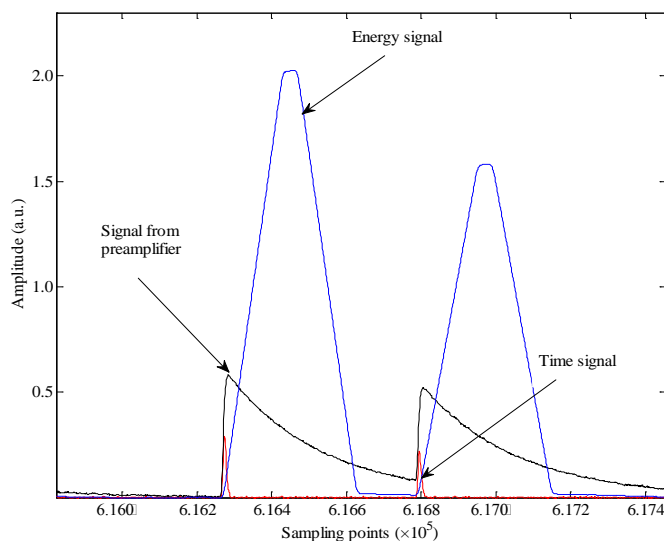


Figure 4.9 Illustration of the time and energy signal shaped in parallel in the trapezoidal filtering.

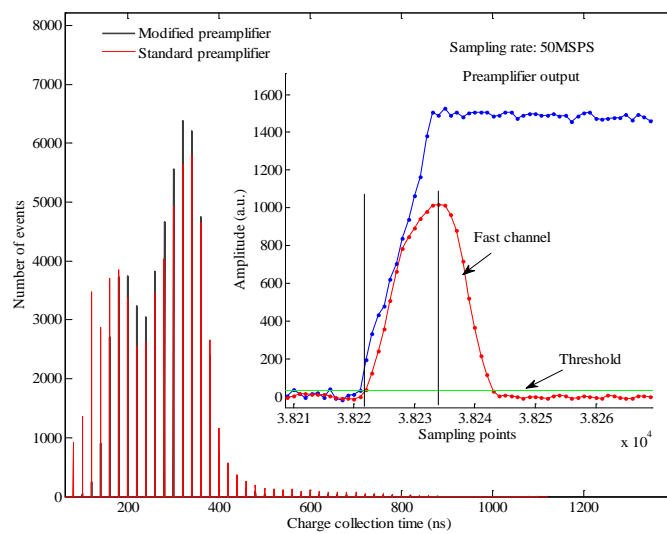


Figure 4.10 Distribution of charge collection time at input count rate of 20 kcps.

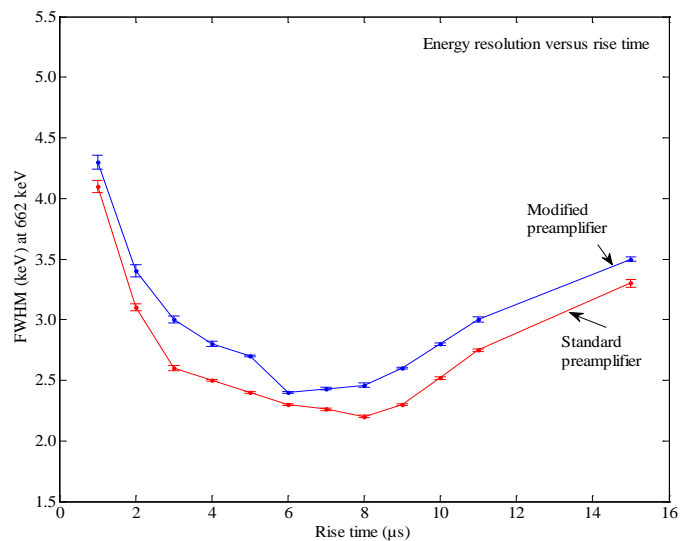


Figure 4.11 Energy resolution versus rise time in the trapezoidal filtering (flat top time was fixed at 0.8 μ s).

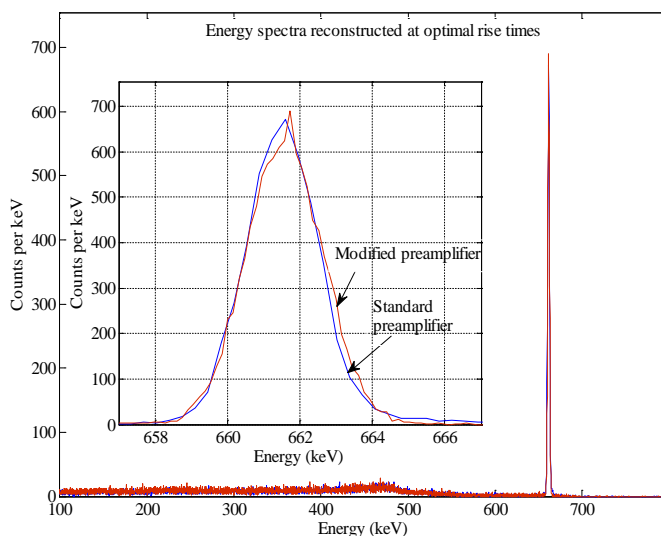


Figure 4.12 Energy spectra reconstructed at optimal rise times (flat top time was fixed at $0.8 \mu\text{s}$).

4.4 Conclusions

In this work, the modification to the feedback resistor of an HPGe preamplifier were proven to be an effective approach to reduce the saturation time after each linac pulse in a pulsed photonuclear environment. Valuable information only available shortly after the irradiation can be obtained if the preamplifier recovers quickly. In addition, this improvement could be beneficial to applications where high linac repetition rate is utilized. The modification to the tail time can significantly decrease baseline shift, which is important for system stability and performance in high rate situations. After the modifications, only a small degradation in energy resolution was observed. Moving the

FET and feedback components back into the cryostat will likely improve the energy resolution.

Acknowledgement

This research is being performed using funding received from the DOE Office of Nuclear Energy's Nuclear Energy University Programs.

References

1. E. Barat et al., "A bimodal Kalman smoother for nuclear spectrometry," *Nucl. Instr. Meth. Phys. Res. A*, vol. 567, pp. 350-352, 2006.
2. E. Barat et al., "ADONIS: A New Concept of X/Gamma Pulse Analyzer," *ANIMMA Conference Record*, N210, 2009.
3. B. VanDevender, et al., "High-purity germanium spectroscopy at rates in excess of 10^6 events/s," *IEEE Trans. Nucl. Sci.*, vol. 61, pp. 2619-2627, 2014.
4. T. Petrovic, et al., "Efficient reduction of piled-up events in gamma-ray spectrometry at high count rates," *IEEE Trans. Nucl. Sci.*, vol. 61, pp. 584-589, 2014.
5. J. Jones, "Detection of pulsed bremsstrahlung-induced prompt neutron capture gamma rays with a HPGe detector," *Proc. SPIE*, 2867, 1997.
6. W. Yoon, et al., "Photonuclear-based Explosive Detection System Optimizations," *AIP Conf. Proc.*, 680, 2003.
7. J. Jones, et al., "Photonuclear-based, nuclear material detection system for cargo containers," *Nucl. Instr. Meth. Phys. Res. B*, vol. 241, pp. 770-776, 2005.
8. C. Brown, et al., "Optimization of S/B in the detection of nuclear fission signatures via different accelerator pulsing modes," *Nucl. Instr. Meth. Phys. Res. A*, vol. 652, pp. 133-136, 2011.

9. E. Reedy, et al., "The detection of delayed gamma-rays between intense bremsstrahlung pulses for discriminating fissionable from non-fissionable materials," *Nucl. Instr. Meth. Phys. Res. A*, vol. 606, pp. 811-815, 2009.
10. D. Norman, et al., "Time-dependent delayed signatures from energetic photon interrogations," *Nucl. Instr. Meth. Phys. Res. B*, vol. 261, pp. 316-320, 2007.
11. F. Carrel, et al., "Identification and differentiation of actinides inside nuclear waste packages by measurement of delayed gammas," *IEEE Trans. Nucl. Sci.*, vol. 57, pp. 2862-2871, 2010.
12. J. Stevenson, et al., "Linac based photofission inspection system employing novel detection concepts," *Nucl. Instr. Meth. Phys. Res. A*, vol. 652, pp. 124-128, 2011.
13. R. Runkle, et al., "Rattling nucleons: New developments in active interrogation of special nuclear material," *Nucl. Instr. Meth. Phys. Res. A*, vol. 663, pp. 75-95, 2012.
14. T. Gozani, "Fission signatures for nuclear material detection," *IEEE Trans. Nucl. Sci.*, vol. 56, pp. 736-741, 2006.
15. X. Wen, et al., "Simulation and measurement of delayed γ -rays after photon-induced fission," *Nucl. Instr. Meth. Phys. Res. A*, vol. 729, pp. 781-787, 2013.
16. T. England, et al., "Evaluation and compilation of fission product yields," LA-UR-94-3106, 1993.
17. J. Jones, et al., "Detection of shielded nuclear material in a cargo container," *Nucl. Instr. Meth. Phys. Res. A*, vol. 562, pp. 1085-1088, 2006.
18. X. Wen, et al., "Study on a digital pulse processing algorithm based on template-matching for high-throughput spectroscopy," *Nucl. Instr. Meth. Phys. Res. A*, vol. 784, pp. 269-273, 2015.
19. V. Jordanov, et al., "Digital techniques for real-time pulse shaping in radiation measurement," *Nucl. Instr. Meth. Phys. Res. A*, vol. 353, pp. 261-264, 1994.
20. V. Jordanov, et al., "Digital synthesis of pulse shapes in real time for high resolution radiation spectroscopy," *Nucl. Instr. Meth. Phys. Res. A*, vol. 345, pp. 337-345, 1994.
21. F. Goulding, et al., "Ballistic deficit correction in semiconductor detector spectrometers," *IEEE Trans. Nucl. Sci.*, vol. 35, pp. 119-124, 1988.

22. G. Gilmore, Practical Gamma-ray Spectrometry, John Wiley & Sons, 2nd Edition, 2008.

5 Fourth Manuscript

Study on a digital pulse processing algorithm based on template-matching for high-throughput spectroscopy

Xianfei Wen, Haori Yang

Nuclear Instruments and Methods in Physics Research Section A: Accelerators, Spectrometers, Detectors and Associated Equipment

vol. 784, pp. 269-273, 2015

Study on a digital pulse processing algorithm based on template-matching for high-throughput spectroscopy

Xianfei Wen^a, Haori Yang^{a*}

^aDepartment of Nuclear Engineering and Radiation Health Physics, Oregon State University, Corvallis, OR 97331, USA

Abstract

A major challenge in utilizing spectroscopy techniques for nuclear safeguards is to perform high-resolution measurements at an ultra-high throughput rate. Traditionally, piled-up pulses are rejected to ensure good energy resolution. To improve throughput rate, high-pass filters are normally implemented to shorten pulses. However, this reduces signal-to-noise ratio and causes degradation in energy resolution. In this work, a pulse pile-up recovery algorithm based on template-matching was proved to be an effective approach to achieve high-throughput gamma ray spectroscopy. Firstly, a discussion of the algorithm was given in detail. Secondly, the algorithm was then successfully utilized to process simulated piled-up pulses from a scintillator detector. Thirdly, the algorithm was implemented to analyze high rate data from a NaI detector, a silicon drift detector and a HPGe detector. The promising results demonstrated the capability of this algorithm to achieve high-throughput rate without significant sacrifice in energy resolution. The performance of the template-matching algorithm was also compared with traditional shaping methods.

Keywords: digital pulse processing; template-matching; high-throughput rate

5.1 Introduction

Innovative systems with increased sensitivity and resolution are in great demand to detect diversion and to prevent misuse in support of nuclear materials management for the U.S. fuel cycle [1-3]. Nuclear fission is the most important multiplicative process involved in non-destructive active interrogation. Among others, unique delayed gamma-ray spectra exist for fissionable isotopes and can be used for isotopic composition measurement [4-16]. A major challenge in utilizing delayed fission gamma rays emitted after active interrogation for safeguards applications is to perform high-resolution spectroscopy measurements at an ultra-high throughput rate [17]. In our recent experimental study at Idaho Accelerator Center, the high-energy x-ray beam with maximum energy of 22 MeV generated by a pulsed linac was used as the photon source. Delayed γ -rays emitted from photon-induced fission reactions inside the samples were measured between adjacent linac pulses with several gamma spectroscopy systems. However, these systems could not work within several milliseconds following each linac pulse although they were well shielded to get rid of irradiation directly from the interrogation source [10]. In addition to modification of front-end electronics to allow rapid recovery from saturation after each linac pulse, innovative pulse analysis algorithms are needed to achieve high-throughput. Using traditional pulse processing algorithms, throughput rate could be significantly impacted when the input rate is high, due to pile-up

rejection. Recently, pulse pile-up recovery based on template-matching has been proved to be an effective approach to achieve high throughput gamma spectroscopy [18-21].

5.2 Discussion of the Algorithm

In a simplified model, the output signal $y(t)$ from a gamma-ray detector is the convolution of the incident gamma ray signal $s(t)$ with the detector response matrix M : $y(t) = s(t) * M$. Thus, if the response matrix can be accurately determined, an estimation of the incident signal can be obtained through a deconvolution process. The incident signal is normally modeled as a train of delta functions, with random time of arrival and amplitude. The detector response is considered to be time-invariant and can be pre-determined. The first step of the algorithm discussed here is to determine the time of arrival for each pulse by the use of a narrow trapezoidal filter [22]. This can greatly reduce the complexity of the problem. Once the time of arrival for each pulse is

determined, the detection process could be re-written as:
$$\begin{bmatrix} y_1 \\ \vdots \\ y_D \end{bmatrix} = \begin{bmatrix} t_{11} & \cdots & t_{1B} \\ \vdots & \ddots & \vdots \\ t_{D1} & \cdots & t_{DB} \end{bmatrix} \begin{bmatrix} s_1 \\ \vdots \\ s_B \end{bmatrix}.$$

Here, s_j ($j = 1, \dots, B$) is a vector containing the amplitude of the B incident pulses. y_i ($i = 1, \dots, D$) is the measured signal at time i . D is the length of the digitized waveform. The elements of the response matrix t_{ij} contain the contribution from the j th pulse to the measurement at the i th time point. Assuming the time-invariant impulse response of the detector was known (i.e. the template), the matrix t_{ij} can then be calculated once the time of arrival for each pulse is determined. Each row of the matrix would just be the impulse response with various amount of delay. Ideally, since y_i is measured and t_{ij} can be

calculated, one could invert the response matrix and mathematically solve for the amplitude of the incident pulses. In fact, this was carried out in our study and gave reasonably good results. However, there are some factors that might push one away from this direct approach. For example, if the dimension of the response matrix t_{ij} is too large (e.g. emission imaging), the calculation involved in direct inversion is prohibitive. In addition, the response matrix might be sparse, which also pose serious challenge to direct inversion. Furthermore, the measured signal y_i could be noisy, preventing an accurate numerical solution. Due to these factors, the response matrix is often nearly singular and the equation above cannot be reliably solved for the amplitude of the incident pulses with direct inversion. In this case, Maximum Likelihood Expectation Maximization (ML-EM) algorithm could be used to provide an estimation of the s_j vector using the well-known

$$\text{equation } s_k^{(n+1)} = s_k^{(n)} \left\{ \frac{1}{\sum_{d=1}^D t_{dk}} \sum_{d=1}^D \left[\frac{y_d}{\sum_{b=1}^B t_{db} x_b^{(n)}} t_{dk} \right] \right\} [23].$$

The algorithm described above was first tested using simulated data. The impulse response function was assumed to be a double exponential function, simulating the anode signal from a PMT coupled with a scintillator detector. The rising edge time constant is determined by the PMT response time (normally between 20 and 80 ns), while the falling edge has the decay constant of the scintillator (e.g. 230 ns for NaI). The amplitude and the time of arrival of each pulse were randomly generated. The simulated waveform was then generated as the superposition of these individual pulses. In pulse processing, the shape (i.e. template) and the time of arrival of each pulse were assumed to be known.

Using the algorithm described above, the amplitude of each pulse can be calculated. As shown in Figure 5.1, if the time of arrival and the template can be accurately determined, the result is very good even when a white noise was added to the simulated anode signal.

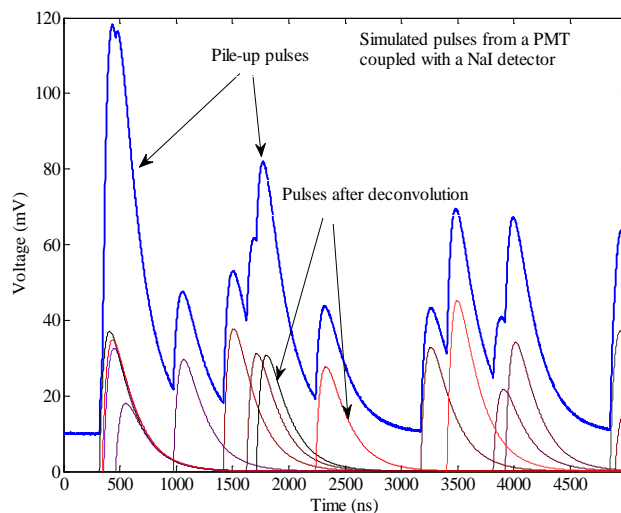


Figure 5.1 The application of the template-matching algorithm to recover simulated piled-up pulses.

5.3 Results and Discussion

The implementation of the template-matching algorithm on high rate NaI data, silicon drift detector data and HPGe data is discussed below. Its performance was also compared with a traditional pulse processing algorithm using trapezoidal filters.

5.3.1 Implementation on Signals from a NaI Detector

Firstly, the algorithm was implemented on signals obtained using a NaI detector. The detector used in these measurements was a Canberra Model 802 detector with a 2" by 2"

crystal. The anode signal was directly digitized at a sampling rate of 100 MSPS using a National Instruments digitizer, model number PXIe-5122. A LabVIEW program was developed to enable streaming of digitized data onto a hard drive array at full speed for off-line processing. The digitized signal and the template are shown in Figure 5.2. Due to the large noise imposed on the anode signal, matching result was not ideal. Also, the determination of the time of arrival was challenging. Because of the fast rising edge, an offset of one or two points could cause a large deviation between the template and the measured data. In this case, the signal measured at very low count rate was used as the template for deconvolution. The performance of the template-matching algorithm was compared with traditional shaping methods. The shaping parameters (i.e. rise time and flat top time) used in the measurement with the Canberra Lynx system were $1\ \mu\text{s}$ and $1\ \mu\text{s}$. At moderate count rate ($\sim 200\ \text{kcp/s}$), the results were comparable, as shown in Figure 5.3.

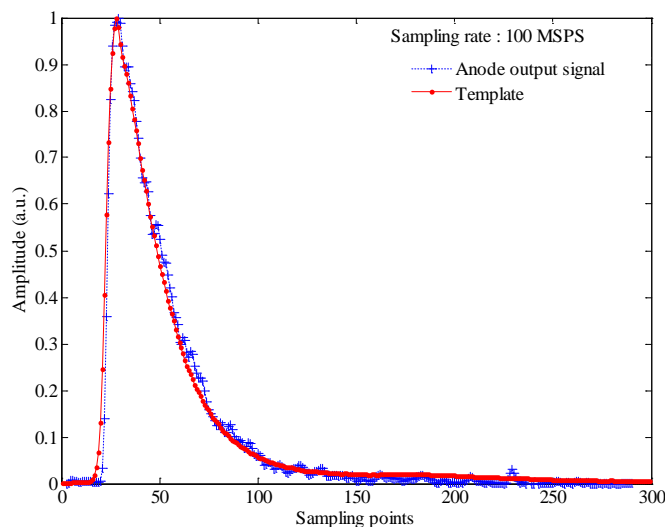


Figure 5.2 The anode output signal and the template.

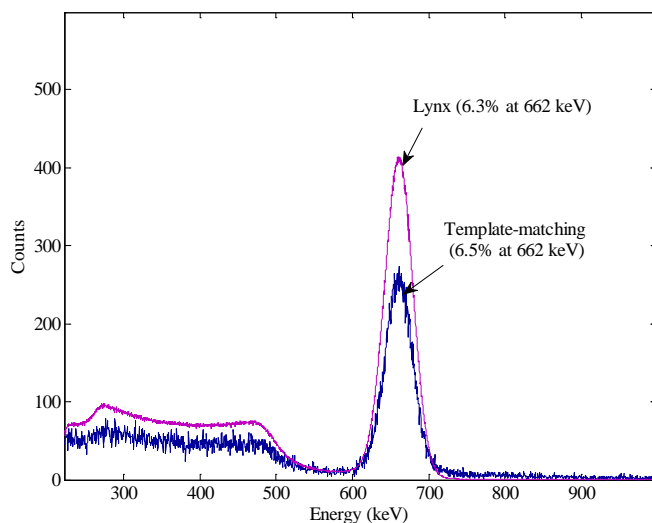


Figure 5.3 Comparison between energy spectra measured with a Canberra Lynx system and reconstructed with the template-matching algorithm.

5.3.2 Implementation on Signals from a Silicon Drift Detector

The performance of the algorithm was also tested on high rate data measured with a silicon drift detector, provided by Southern Innovation. During the measurements, a Mn foil was irradiated with photons generated from an Amptek Mini-X tube to produce characteristic x-rays with energy of 5.89 keV and 6.49 keV. The detector used was a Ketek 30 mm² silicon drift detector [24]. Different input count rate (between 50 kcps and 500 kcps) was produced by tuning the tube current. The 50 kcps data was utilized to create a template by averaging over 200 pulses that did not suffer from pile-up. The energy resolution that the template-matching algorithm achieved at low input count rate (i.e. 50 kcps) was 131 eV at 5.89 keV. Good Gaussian peak shape and reasonable energy resolution could still be obtained even at very high input rate (e.g. 500 kcps), as shown in

Figure 5.4. To compare the performance of the template-matching algorithm with traditional pulse processing using trapezoidal filters, we first adjusted shaping parameters to achieve comparable energy resolution and compared throughput rate at each input rate. As shown in Figure 5.5 a much higher throughput rate (e.g. 467 kcps vs 67 kcps at 500 kcps input rate) was achieved with the template-matching algorithm at very high input rate. The traditional pulse processing algorithm suffered huge decrease in throughput at high input rates due to pile-up rejection. The shaping parameters were then adjusted to achieve similar throughput rate using both algorithms at a certain input rate. Figure 5.6 shows the energy resolution as a function of input rate. As can be observed, using the template matching algorithm, resolution of less than 200 eV at 5.89 keV could be achieved even at 500 kcps. The resolution gradually degraded as input rate increased. This degradation is much more prominent for the traditional processing algorithm due to pile-up. In summary, Figures 5.4-5.6 clearly demonstrated the advantages of the template-match algorithm over traditional approaches: superior throughput with comparable energy resolution; superior energy resolution with comparable throughput.

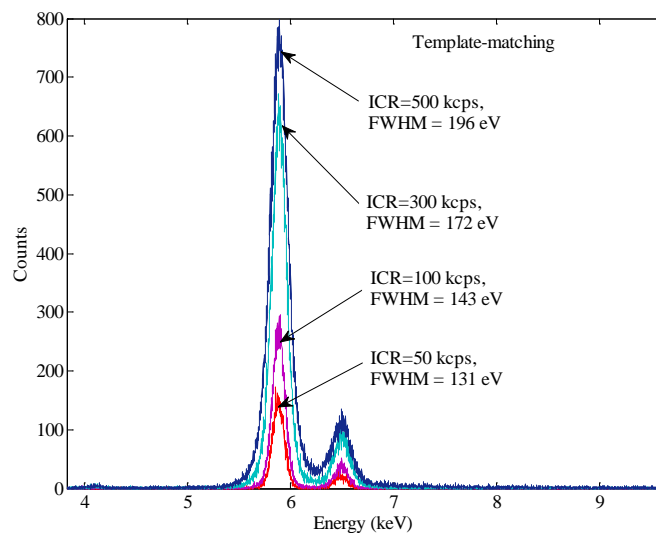


Figure 5.4 Energy spectra at different Input Count Rates (ICR) with the template-matching algorithm.

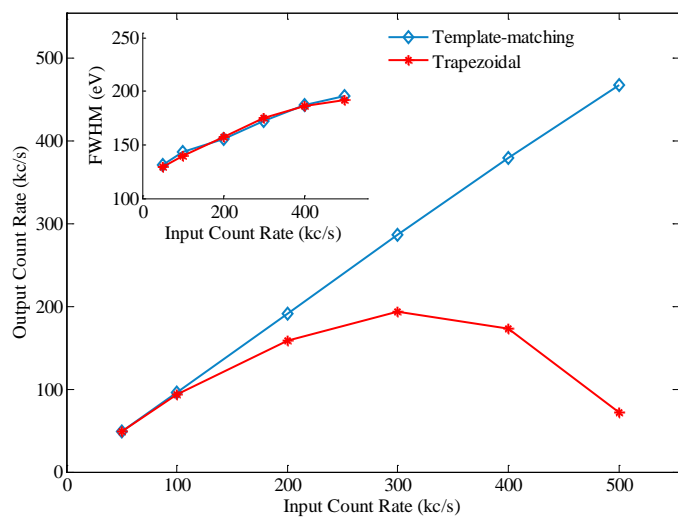


Figure 5.5 Comparison between the template-matching algorithm and the trapezoidal filter (Output Count Rate vs Input Count Rate).

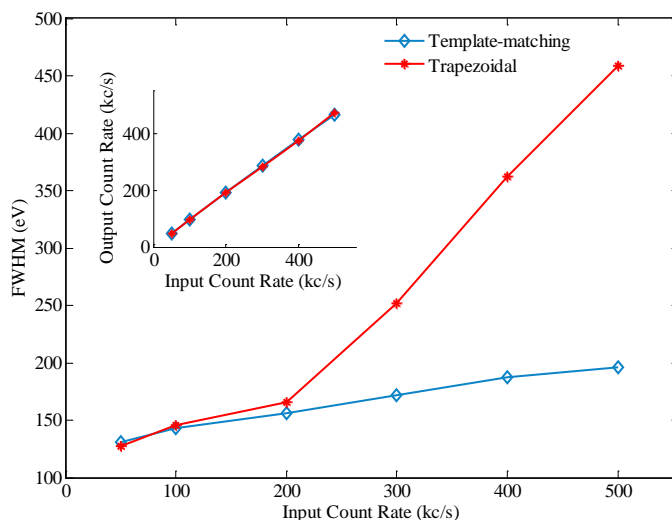


Figure 5.6 Comparison between the template-matching algorithm and the trapezoidal filter (FWHM vs Input Count Rate).

5.3.3 Implementation on Signals from a HPGe Detector

The HPGe detector is the only practical choice that can provide excellent energy resolution in a wide energy range as needed in measuring delayed gamma-ray spectra following active interrogation for nuclear safeguards applications. As discussed above, in such measurements, there are two issues that greatly limit the throughput of a HPGe detector: the long saturation after each linac pulse and the pulse pile-up due to high input rate. Our approaches to address this challenge include modification of the front-end electronics of a HPGe detector to allow fast return from saturation to baseline at high-energy input rate and the development of advanced digital signal processing techniques to improve the throughput rate with only small sacrifice in energy resolution. Here, we discuss the implementation of the template-matching algorithm on signals from a HPGe

detector. It is quite challenging to implement the template-matching algorithm on HPGe signals because of the variation in pulse shape. To be specific, for a pulse from the pre-amplifier, the falling edge is determined by the RC constant of the pre-amplifier (e.g. $\sim 50 \mu\text{s}$). On the other hand, the rising edge varies with the gamma-ray interaction position inside the detector. For simplicity, a generic template was used in current work. Pulses from the pre-amplifier were very well reconstructed at the falling edge, but a significant amount of deviation between the measured and reconstructed signals could be observed at the rising edge, as shown in Figure 5.7. In spite of this large deviation, good energy resolution at input rates up to 200 kcps was achieved, as shown in Figure 5.8. A performance comparison between the template-matching algorithm and the traditional trapezoidal shaping was again performed and summarized in Table 5.1. The results showed the advantage of the template-matching approach despite the fact that a good template is difficult to construct.

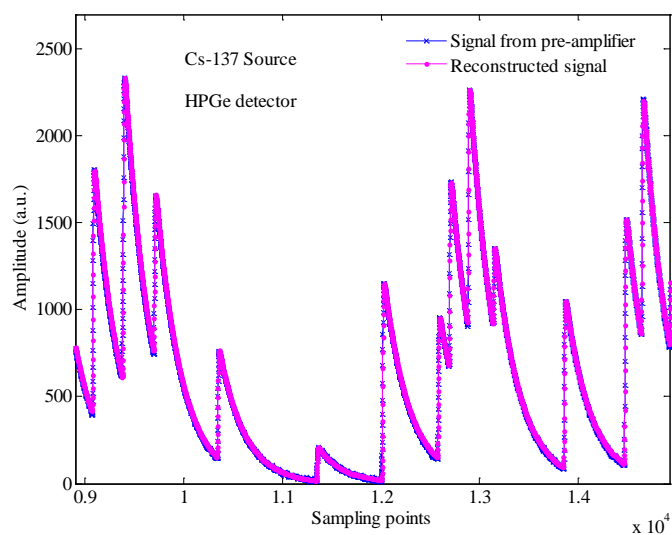


Figure 5.7 Verification of the reconstructed signal from preamplifier.

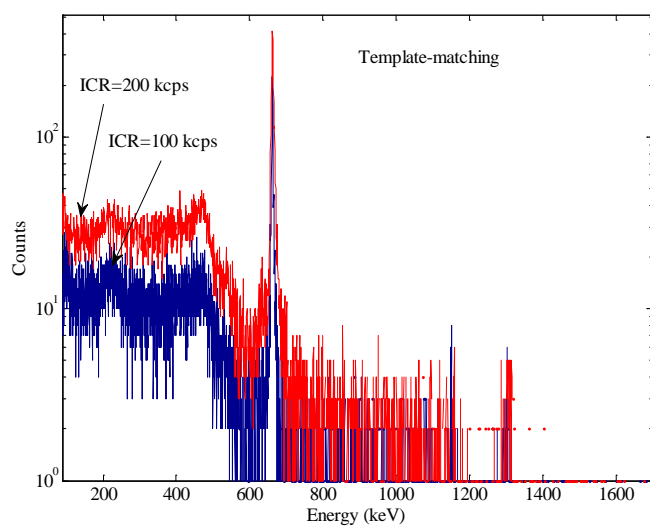


Figure 5.8 Energy spectra reconstructed with the template-matching algorithm.

Table 5.1 Comparison between the template-matching algorithm and the trapezoidal filter (HPGe data).

	Input Count Rate (kc/s)	Output Count Rate (kc/s)	FWHM (keV) at 662 keV
Trapezoidal	100	79.8	2.7
	200	141.0	3.9
Template-matching	100	96.6	2.8
	200	186.8	4.6

5.4 Conclusion

To perform high-resolution spectroscopy measurements at an ultra-high throughput rate is a major challenge in active interrogation techniques for nuclear safeguards application. In this work, the development of advanced digital signal processing technique based on template-matching has been shown as an effective approach to address this issue. The principle behind the algorithm was described in detail. This algorithm was first tested using simulated piled-up pulses from a PMT coupled with a scintillator detector. Using a NaI detector, at moderate count rate (~ 200 kcps), energy resolution comparable to traditional trapezoidal shaping was achieved (6.5 % at 662 keV). With high rate data acquired with a silicon drift detector, the advantages of this new algorithm were demonstrated through comparison with the traditional approach using trapezoidal filters. Superior performance in terms of throughput rate and energy resolution was observed at high input rates. The performance of the template-match

algorithm was then evaluated using signals from a HPGe detector. Despite the difficulty to construct an ideal template for pre-amplifier pulses, energy resolution of 4.6 keV at 662 keV and live time of 93.4% were successfully achieved at input rate of 200 kcps.

Acknowledgement

The authors would like to thank Dr. Paul Scoullar from Southern Innovation for providing the silicon drift detector data. This research is being performed using funding received from the DOE Office of Nuclear Energy's Nuclear Energy University Programs.

References

1. R. Runkle, D. Chichester, S. Thompson, "Rattling nucleons: New developments in active interrogation of special nuclear material," *Nucl. Instr. Meth. Phys. Res. A*, vol. 663, pp. 75-95, 2012.
2. J. Dolan, M. Flaska, S. Pozzi, D. Chichester, "Passive measurements of mixed-oxide fuel for nuclear nonproliferation," *Nucl. Instr. Meth. Phys. Res. A*, vol. 703, pp. 102-108, 2013.
3. B. Goddard, S. Croft, "High-fidelity passive neutron multiplicity measurements and simulations of uranium oxide," *Nucl. Instr. Meth. Phys. Res. A*, vol. 712, pp. 147-156, 2013.
4. E. Norman, et al., "Signatures of fissile materials: high-energy gamma rays following fission," *Nucl. Instr. Meth. Phys. Res. A*, vol. 521, pp. 608-610, 2004.
5. R. Marrs, E. Norman, J. Burke, et al., "Fission-product gamma-ray line pairs sensitive to fissile material and neutron energy", *Nucl. Instr. Meth. Phys. Res. A*, vol. 592, pp. 463-471, 2008.
6. D. Beddingfield, F. Cecil, "Identification of fissile materials from fission product gamma-ray spectra," *Nucl. Instr. Meth. Phys. Res. A*, vol. 417, pp. 405-412, 1998.

7. R. B. Walton, et al., "Delayed Gamma Rays from Photofission of U-238, U-235, and Th-232," *Phys. Rev. B*, vol. 134, pp. 824-832, 1964.
8. S. Kahane, et al., "Photofission of U-238 with neutron-capture gamma rays," *Phys. Rev. C*, vol. 32, pp. 1944-1955, 1985.
9. J. Jones, D. Norman, K. Haskell, et al., "Detection of shielded nuclear material in a cargo container," *Nucl. Instr. Meth. Phys. Res. A*, vol. 562, pp. 1085-1088, 2006.
10. X. Wen, J. Kavouras, D. Nakazawa, H. Yang, "Simulation and measurement of delayed γ -rays after photon-induced fission," *Nucl. Instr. Meth. Phys. Res. A*, vol. 729, pp. 781-787, 2013.
11. C. Hollas, D. Close, C. Moss, "Analysis of fissionable material using delayed gamma rays from photofission," *Nucl. Instr. Meth. Phys. Res. B*, vol. 24, pp. 503-505, 1987.
12. M. Gmar, et al., "Assessment of actinide mass embedded in large concrete waste packages by photon interrogation and photofission," *Appl. Radiat. Isot.*, vol. 63, pp. 613, 2005.
13. F. Carrel, M. Agelou, M. Gmar, et al., "Identification and differentiation of actinides inside nuclear waste packages by measurement of delayed gammas," *IEEE Trans. Nucl. Sci.*, vol. 57, pp. 2862-2871, 2010.
14. E. Reedy, S. Thompson, A. Hunt, "The detection of delayed gamma-rays between intense bremsstrahlung pulses for discriminating fissionable from non-fissionable materials," *Nucl. Instr. Meth. Phys. Res. A*, vol. 606, pp. 811-815, 2009.
15. M. Kinlaw, A. Hunt, "Fissionable isotope identification using the time dependence of delayed neutron emission," *Nucl. Instr. Meth. Phys. Res. A*, vol. 562, pp. 1081-1084, 2006.
16. T. Gozani, "Active Nondestructive Assay - Principles and Applications," NUREG/CR-0602, 1981.
17. H. Yang, D. Wehe, D. Bartels, "Spectroscopy of high rate events during active interrogation," *Nucl. Instr. Meth. Phys. Res. A*, vol. 598, pp. 779-787, 2009.
18. P. Scoullar, R. Evans, "Maximum likelihood estimation techniques for high rate, high throughput digital pulse processing," 2009.
19. P. Scoullar, R. Evans, "Method and apparatus for resolving individual signals in detector output data," Patent NO.: US 7,383,142 B2, 2008.

20. M. Bolic, V. Drndarevic, W. Gueaieb, "Pileup correction algorithms for very-high-count-rate gamma-ray spectrometry with NaI(Tl) detectors," *IEEE Trans. on Instrumentation and Measurement*, vol. 59, 2010.
21. B. Loher, " γ - ray spectroscopy with a LaBr₃:(Ce) scintillation detector at ultra-high count rates," M.S. thesis, 2010.
22. V. Jordanov, G. Knoll, A. Huber, et al., "Digital techniques for real-time pulse shaping in radiation measurement," *Nucl. Instr. Methods Phys. Res. A*, vol. 353, pp. 261-264, 1994.
23. T. Moon, "The expectation - maximization algorithm," *IEEE signal processing magazine*, November 1996.
24. P. Scoullar, D. Scoullar, M. Brown, et al., "Advanced signal processing hardware for high throughput energy dispersive spectroscopy," NSLS Presentation, 2013.

6 General Conclusion

In used nuclear fuel assay, non-destructive techniques to identify and quantify special nuclear materials are in great demand. Although nuclear materials naturally emit characteristic radiation, their intensities and energies are normally low. Furthermore, these γ -rays could be buried in large background and intentionally shielded. Photofission techniques based on measurement of delayed γ -rays have been proven to be an effective approach. However, there were three major challenges to be addressed in the photofission techniques. First, Published data on photofission product yields is rare. Second, simulation of delayed γ -rays from photofission has not been validated. Third, the input γ -rays count rate could reach 10^6 cps. How to perform high-resolution high-throughput spectroscopy measurement at such high input rate is challenging.

In this work, high-energy delayed γ -rays ($E_\gamma > 3$ MeV) were measured in between linac pulses using independent data acquisition systems. A list-mode system was also developed to measure low-energy delayed γ -rays after irradiation. Photofission product yields of ^{238}U and ^{239}Pu were determined based on the delayed γ -ray spectra measured in between linac pulses and after irradiation. These photofission yields could contribute to nuclear data library. They can also provide valuable information for designing assay systems based on photonuclear techniques in homeland security and nuclear safeguards applications, such as used nuclear fuel assay. The measured photofission product yields are present in the first paper. The experimental outcomes were also compared with Monte Carlo simulation results. It was observed that some peak lines were measured in the

experiments, however, they were not predicted by simulation or over-predicted/under-predicted. Also, some lines that were predicted by simulation were not observed in the measurements. The comparison demonstrated the capabilities and limitations of current available simulation package (MCNPX 2.7.0) and provided guidance for system design based on photofission techniques for used nuclear fuel assay. The second paper presents the measured delayed γ -ray energy spectra and the comparison between measurement and simulation results.

Another challenge in the application of photofission techniques to used nuclear fuel assay is to perform spectroscopy measurements with high-resolution high-throughput at ultra-high rate. The two-folded approach was shown to effectively address this challenge. First, the modifications to the HPGe preamplifier improved its high-rate performance in a pulsed photonuclear environment. At high linac repetition rate (e.g. 125 Hz), a standard preamplifier as used in this study would be paralyzed for ~70% of the time. Instead, a maximum live time of 66% can be achieved in theory after modification, due to the much reduced recovery time. Also, the significant reduction of baseline shift could be beneficial to many high-rate applications. For example, in used nuclear fuel assay, the input count rate can often reach 10^6 cps or higher. Thus a preamplifier with nominal tail time (i.e. 50 μ s) would be easily saturated. However, as a result of the reduced tail time, the modified preamplifier could potentially be used to perform spectroscopy measurement and provide valuable information about used fuel assemblies. The work on the modifications is illustrated in the third paper. Second, the advanced digital pulse

processing algorithms including the template-matching method and de-randomization technique were demonstrated to significantly improve throughput rate without large sacrifice in energy resolution at ultra-high input count rate. For example, using the de-randomization technique, energy resolution of 2.5 keV at 662 keV was achieved at input count rate of 100 kcps. The output count rate was also 100 kcps since pile-up correction was not performed. The algorithm was also applied to the 300 kcps HPGe data. Without pile-up rejection or recovery, only slight degradation in energy resolution was observed (3.1 keV vs 2.5 keV @ 662 keV). The development of the advanced pulse processing algorithm (i.e. template matching) is present in the fourth paper. The de-randomization technique is described in Appendix B.

The work present in this dissertation addressed the three major challenges in the application of photofission based active non-destructive techniques for used nuclear fuel assay.

Bibliography

B. VanDevender, et al., "High-purity germanium spectroscopy at rates in excess of 10^6 events/s," *IEEE Trans. Nucl. Sci.*, vol. 61, pp. 2619-2627, 2014.

J. Jones, et al., "Photonuclear-based, nuclear material detection system for cargo containers," *Nucl. Instr. Meth. Phys. Res. B*, vol. 241, pp. 770-776, 2005.

E. Reedy, et al., "The detection of delayed gamma-rays between intense bremsstrahlung pulses for discriminating fissionable from non-fissionable materials," *Nucl. Instr. Meth. Phys. Res. A*, vol. 606, pp. 811-815, 2009.

J. Stevenson, et al., "Linac based photofission inspection system employing novel detection concepts," *Nucl. Instr. Meth. Phys. Res. A*, vol. 652, pp. 124-128, 2011.

D. Norman, et al., "Time-dependent delayed signatures from energetic photon interrogations," *Nucl. Instr. Meth. Phys. Res. B*, vol. 261, pp. 316-320, 2007.

R. Runkle, et al., "Rattling nucleons: New developments in active interrogation of special nuclear material," *Nucl. Instr. Meth. Phys. Res. A*, vol. 663, pp. 75-95, 2012.

X. Wen, et al., "Photofission product yields of ^{238}U and ^{239}Pu with 22-MeV bremsstrahlung," *Nucl. Instr. Meth. Phys. Res. A*, 2016, (in revision).

X. Wen, et al., "Simulation and measurement of delayed γ -rays after photon-induced fission," *Nucl. Instr. Meth. Phys. Res. A*, vol. 729, pp. 781-787, 2013.

X. Wen, et al., "Evaluation of a modified HPGe preamplifier for high-rate spectroscopy measurements in a pulsed photonuclear environment," *Nucl. Tech.*, vol. 194, 2016.

X. Wen, et al., "Study on a digital pulse processing algorithm based on template-matching for high-throughput spectroscopy," *Nucl. Instr. Meth. Phys. Res. A*, vol. 784, pp. 269-273, 2015.

Nuclear nonproliferation, United States Government Accountability Office, 2005.

K. Murakami, "Nuclear safeguards concepts, requirements, and principles applicable to nuclear security," 2012.

K. Davenport, et al., "Assessing progress on nuclear nonproliferation and disarmament," 2013.

- A. Carlson, et al., Nondestructive Evaluation of the VSC-17 Cask, INL/EXT-05-00968, 2006.
- J. Werner, U.S. Spent Nuclear Fuel Storage, 2012.
- T. Gozani, "Fission signatures for nuclear material detection," *IEEE Trans. Nucl. Sci.*, vol. 56, pp. 736-741, 2006.
- K. Jordan, et al., "Detection of ^{235}U in hydrogenous cargo with differential die-away analysis and optimized neutron detectors," *Nucl. Instr. Meth. Phys. Res. A*, vol. 579, pp. 388-390, 2007.
- D. Dore, et al., "Delayed neutron and delayed photon characteristics from photofission of ^{232}Th , $^{235,238}\text{U}$ and ^{237}Np with endpoint bremsstrahlung photons in the giant dipole resonance region," *International Workshop on Nuclear Fission and Fission-Product Spectroscopy*, 2009.
- W. Hage, et al., "Nondestructive fissile material assay by induced fission neutron correlation," *Nucl. Instr. Meth. Phys. Res. A*, vol. 551, pp. 396-419, 2005.
- J. Meason et al., "Photofission of ^{238}U induced by 17.5-MeV monoenergetic gamma rays," *Phys. Rev.* 142, 1966.
- E. Jacobs et al., "Product yields for the photofission of ^{238}U with 12-, 15-, 20-, 30-, and 70-MeV bremsstrahlung," *Phys. Rev. C* 19, 1979.
- E. Jacobs et al., "Product yields for the photofission of ^{235}U with 12-, 15-, 20-, 30-, and 70-MeV bremsstrahlung," *Phys. Rev. C* 21, 1980.
- D. Wehe et al., "Observation of ^{238}U photofission products," *IEEE Trans. Nucl. Sci.*, vol. 53, pp. 1430-1434, 2006.
- F. Carrel, et al., "New experimental results on the cumulative yields from thermal fission of ^{235}U and ^{239}Pu and from photofission of ^{235}U and ^{238}U induced by bremsstrahlung," *IEEE Trans. Nucl. Sci.*, vol. 58, pp. 2064-2072, 2011.
- J. Durkee, et al., "Delayed-gamma simulation using MCNPX," *Nucl. Tech.*, vol. 168, pp. 761-764, 2009.
- J. Durkee, et al., "Delayed-gamma signature calculation for neutron-induced fission and activation using MCNPX. Part II: Simulations," *Progress in Nuclear Energy*, vol. 51, pp. 828-836, 2009.

M. Andrews, et al., "MCNP6 simulations of gamma line emissions from fission products and their comparisons to plutonium and uranium measurements," *Progress in Nuclear Energy*, vol. 79, pp. 87-95, 2015.

D. Pelowitz, et al., "MCNPX 2.7.E extensions," LA-UR-11-01502, 2011.

M. James, "MCNPX 2.7.X - new features being developed," *IEEE/NSS*, Orlando, FL, 2009.

E. Barat, et al., "ADONIS: a new system for high count rate HPGe spectrometry," *IEEE Nuclear Science Symposium Conference Record*, N30-6, 2006.

E. Barat, et al., "A bimodal Kalman smoother for nuclear spectrometry," *Nucl. Instr. Meth. Phys. Res. A*, vol. 567, pp. 350-352, 2006.

E. Barat, et al., "ADONIS: A new concept of x/gamma pulse analyzer," *ANIMMA Conference Record*, N210, 2009.

G. Welch, et al., *An introduction to the Kalman filter*, 2006.

T. Gozani, "Active nondestructive assay - principles and applications," *NUREG/CR-0602*, 1981.

M. Gmar et al., "Use of delayed gamma spectra for detection of actinides (U, Pu) by photofission," *Nucl. Instr. Meth. Phys. Res. A*, vol. 422, pp. 841-845, 1999.

B. Micklich et al., "Nuclear materials detection using high-energy γ -rays," *Nucl. Instr. Meth. Phys. Res. B*, vol. 241, pp. 782-786, 2005.

A. Hunt, et al., "Fission signature interferences in active interrogation techniques utilizing high-energy bremsstrahlung," *IEEE Nuclear Science Symposium Conf.*, 2012.

F. Carrel, et al., "Identification and differentiation of actinides inside nuclear waste packages by measurement of delayed gammas," *IEEE Trans. Nucl. Sci.*, vol. 57, p. 2862, 2010.

H. Rennhofer, et al., "Detection of SNM by delayed gamma rays from induced fission," *Nucl. Instr. Meth. Phys. Res. A*, vol. 652, pp. 140-142, 2011.

R. Marrs, et al., "Fission-product gamma-ray line pairs sensitive to fissile material and neutron energy," *Nucl. Instr. Meth. Phys. Res. A*, vol. 592, pp. 463-471, 2008.

- C. Hollas, et al., "Analysis of fissionable material using delayed gamma rays from photofission," LA-UR-86-3363, 1986.
- D. Beddingfield, et al., "Identification of fissile materials from fission product gamma-ray spectra," *Nucl. Instr. Meth. Phys. Res. A*, vol. 417, pp. 405-412, 1998.
- J. Meason, et al., "Photofission of ^{238}U induced by 17.5-MeV monoenergetic gamma rays," *Phys. Rev.* 142, 1966.
- D. Wehe, et al., "Observation of ^{238}U photofission products," *IEEE Trans. Nucl. Sci.*, vol. 53, pp. 1430-1434, 2006.
- E. Norman, et al., "Signatures of fissile materials: high-energy γ -rays following fission," *Nucl. Instr. Meth. Phys. Res. A*, vol. 521, pp. 608-610, 2004.
- R. Firestone, et al., Table of Radioactive Isotopes, database version 2/28/99.
- D. Chichester, et al., "Estimation of the performance of multiple active neutron interrogation signatures for detecting shielded HEU," *IEEE Nuclear Science Symposium Conf.*, 2012.
- J. Jones, et al., "Photofission-based, nuclear material detection: technology demonstration," Idaho Nat. Lab., Idaho Falls, ID, Rep. 02-01406, Dec. 2002.
- J. Jones, et al., "Pulsed photonuclear assessment (PPA) technique: CY04 year-end progress report," Idaho Nat. Lab., Idaho Falls, ID, Rep. 05-02583, Feb. 2005.
- D. Norman, et al., "Inspection applications with higher electron beam energies," *Nucl. Instr. Meth. Phys. Res. B*, vol. 241, pp. 787-792, 2005.
- M. Kinlaw, et al., "Fissionable isotope identification using the time dependence of delayed neutron emission," *Nucl. Instr. Meth. Phys. Res. A*, vol. 562, pp. 1081-1084, 2006.
- S. Kahane, et al., "Photofission of U-238 with neutron-capture gamma rays," *Phys. Rev. C*, vol. 32, pp. 1944-1955, 1985.
- D. Dore, et al., "Delayed neutron yields and spectra from photofission of actinides with bremsstrahlung photons below 20 MeV," *J. Phys. Conf. Ser.*, vol. 41, pp. 241, 2006.
- R. Walton, et al., "Delayed Gamma Rays from Photofission of U-238, U-235, and Th-232," *Phys. Rev. B*, vol. 134, pp. 824-832, 1964.

M. Gmar, et al., "Assessment of actinide mass embedded in large concrete waste packages by photon interrogation and photofission," *Appl. Radiat. Isot.*, vol. 63, pp. 613, 2005.

K. Baumung, et al., "Investigations into nondestructive safeguards techniques," in *Proc. IAEA Symp. Safeguards Tech.*, Karlsruhe, Germany, vol. 2, pp. 192, 1970.

R. Branblett, et al., "Application of photo-induced reactions to nuclear materials safeguards problems," Gulf General Atomic Inc., San Diego, CA, Rep. GA-9614, 1969.

H. Yang, et al., "Spectroscopy of high rate events during active interrogation," *Nucl. Instr. Meth. Phys. Res. A*, vol. 598, pp. 779-787, 2009.

D. R. Slaughter, et al., "The nuclear car wash: A system to detect nuclear weapons in commercial cargo shipments," *Nucl. Instr. Meth. Phys. Res. A*, vol. 579, pp. 349-352, 2007.

H. Yang, "Active interrogation methods for detection of special nuclear material," Ph.D. dissertation, Dept. Nucl. Eng. Radiol. Sci., Univ. Michigan, Ann Arbor, MI, 2009.

V. T. Jordanov, et al., "Digital techniques for real-time pulse shaping in radiation measurement," *Nucl. Instr. Meth. Phys. Res. A*, vol. 353, pp. 261-264, 1994.

J. Verbeke, et al., "Simulation of neutron and gamma ray emission from fission and photofission," Lawrence Livermore Nat. Lab., Livermore, CA, Rep. UCRL-AR-228518, 2010.

MCNPX Version 2.7.0 User's Manual, Los Alamos Nat. Lab., Los Alamos, NM, 2011.

T. Petrovic, et al., "Efficient reduction of piled-up events in gamma-ray spectrometry at high count rates," *IEEE Trans. Nucl. Sci.*, vol. 61, pp. 584-589, 2014.

J. Jones, "Detection of pulsed bremsstrahlung-induced prompt neutron capture gamma rays with a HPGe detector," *Proc. SPIE*, 2867, 1997.

W. Yoon, et al., "Photonuclear-based Explosive Detection System Optimizations," *AIP Conf. Proc.*, 680, 2003.

C. Brown, et al., "Optimization of S/B in the detection of nuclear fission signatures via different accelerator pulsing modes," *Nucl. Instr. Meth. Phys. Res. A*, vol. 652, pp. 133-136, 2011.

- T. England, et al., "Evaluation and compilation of fission product yields," LA-UR-94-3106, 1993.
- V. Jordanov, et al., "Digital synthesis of pulse shapes in real time for high resolution radiation spectroscopy," *Nucl. Instr. Meth. Phys. Res. A*, vol. 345, pp. 337-345, 1994.
- F. Goulding, et al., "Ballistic deficit correction in semiconductor detector spectrometers," *IEEE Trans. Nucl. Sci.*, vol. 35, pp. 119-124, 1988.
- G. Gilmore, *Practical Gamma-ray Spectrometry*, John Wiley & Sons, 2nd Edition, 2008.
- J. Dolan, et al., "Passive measurements of mixed-oxide fuel for nuclear nonproliferation," *Nucl. Instr. Meth. Phys. Res. A*, vol. 703, pp. 102-108, 2013.
- B. Goddard, et al., "High-fidelity passive neutron multiplicity measurements and simulations of uranium oxide," *Nucl. Instr. Meth. Phys. Res. A*, vol. 712, pp. 147-156, 2013.
- P. Scoullar, et al., "Maximum likelihood estimation techniques for high rate, high throughput digital pulse processing," 2009.
- P. Scoullar, et al., "Method and apparatus for resolving individual signals in detector output data," Patent NO.: US 7,383,142 B2, 2008.
- M. Bolic, et al., "Pileup correction algorithms for very-high-count-rate gamma-ray spectrometry with NaI(Tl) detectors," *IEEE Trans. on Instrumentation and Measurement*, vol. 59, 2010.
- B. Loher, " γ - ray spectroscopy with a LaBr₃:(Ce) scintillation detector at ultra-high count rates," M.S. thesis, 2010.
- T. Moon, "The expectation - maximization algorithm," *IEEE signal processing magazine*, November 1996.
- P. Scoullar, et al., "Advanced signal processing hardware for high throughput energy dispersive spectroscopy," NSLS Presentation, 2013.
- P. Sibczynski, et al., "Decay chains and photofission investigation based on nuclear spectroscopy of highly enriched uranium sample," *Applied Radiation and Isotopes*, vol. 82, pp. 170-174, 2013.
- V. Jordanov, "Deconvolution of pulses from a detector-amplifier configuration," *Nucl. Instr. and Meth. A*, vol. 351, pp. 592-594, 1994.

V. Jordanov, "Digital pulse de-randomization for radiation spectroscopy," patent No.: US 6,369,393 B1, 2002.

V. Jordanov, "Exponential signal synthesis in digital pulse processing," *Nucl. Instr. and Meth. A*, vol. 670, pp. 18-24, 2012.

Appendices

A MCNPX Simulation of Delayed γ -rays from Photofission

In the simulation, the geometry model was a sphere with a diameter of 1 cm surrounded by vacuum. The sphere was filled by ^{238}U of 19.1 g/cm^3 . Importance of neutron and photon within the sphere was set at 1. Neutron and photon were not tracked once they exited the sphere. The bremsstrahlung with endpoint energy of 22 MeV produced in a separate simulation was used as the photon source. The neutron physics card was set as *phys: n 3j -101*. The fourth entry *dnb=-101* on this card was used to produce delayed neutron from fission based on the CINDER90 models. Therefore, the ACE libraries were deprecated in this case. All other entries on the neutron physics card were kept at default values. The photon physics card was set as *phys: p 3j 1 j -102*. Biased photonuclear particle production was enabled by setting the fourth entry (i.e. *ispn*) on this card to 1. To accurately obtain energies of delayed γ -rays, models based on line emission data were selected by setting the sixth entry on the photon physics card to *-102*. In addition to the neutron and photon physics cards, the Activation Control Card (ACT) was also used to control the production of delayed neutrons and photons from fission events. The act card was set as *act fission=all nonfiss=none dn=model dg=lines*. The first entry on this card enabled creation of delayed particles from fission events. Production of delayed neutrons and photons from non-fission events were disabled by setting the second entry to none. The third and fourth entries had the same functionality as the entries of *dnb=-101* and *dgb=-102* on the neutron or photon physics cards. The act card was followed by the lca

card. This card was used to select the Bertini, ISABEL, CEM03, or INCL4 physics model and set parameters used in the Bertini and ISABEL models. The eighth entry on the lca card was set at -2. All other entries on this card were kept at default values. The last section of the input file for the simulation included tally cards. Tally type 1 was used to count delayed γ -rays at the sphere surface. Tally energy card *e1 1 6000i 5* divided the energy range from 1 MeV to 5 MeV into 6k bins. Tally time card *t1 100 1e37 NT* separated the tally into two time bins: $-\infty$ to 100 shakes and 100 to 1×10^{37} shakes (1 shake = 10 ns). The entry *NT* means no total bins will be printed in the output data file. Two additional tally cards (i.e. ft card and fu card) were used. Combination of the *ft1 tag 1* and *fu1 ZZAAA.99999* provided the ability to only count delayed γ -rays from fission in the isotope *ZZAAA*. This could avoid the interference by γ -rays created from non-fission events, such as neutron-capture reactions. To reduce statistical error to an acceptable level, the total number of particle histories run in the simulation was 1×10^8 .

The comparisons between the measured and simulated delayed gamma spectra ranging from 2.6 MeV to 5.0 MeV from photofission of ^{238}U are present in Figures 6.1 and 6.2. As shown in these Figures, the measured peaks were successfully predicted in the simulation. However, one notable peak (2971.0 keV) in the simulation results was not observed in the measured spectra. Table 6.1 shows the comparison between measured and simulated intensities with efficiency corrected of the identified peaks relative to the 3287.6 keV peak. The relative intensities of multiple peaks, 2717.3 keV (^{95}Sr), 2941.3 keV (^{98}Y), 3310.0 keV (^{98}Y), 3383.2 keV (^{90}Rb), 3401.3 keV (^{97}Y), 3534.2 keV (^{90}Rb),

3549.5 keV (^{97}Y), 3576.0 keV (^{95}Y), 3599.7 keV (^{91}Rb), 3932.4 keV (^{88}Br), 4078.3 keV (^{91}Rb), 4135.5 keV (^{90}Rb), 4166.3 keV (^{89}Br), 4180.5 keV (^{87}Br), 4365.9 keV (^{90}Rb), and 4450.2 keV (^{98}Y), obtained from the simulation agree well with those from the measured results. However, large discrepancies exist in many peaks, including 2789.3 keV (^{106}Tc), 2868.9 keV (^{136}I), 2933.1 keV (^{95}Sr), 3317.0 keV ($^{90\text{m}}\text{Rb}$), 3458.2 keV (^{93}Rb), and 3867.6 keV (^{93}Rb). The quantitative comparison provides evidence that the Monte Carlo simulation package MCNPX 2.7.0 has capabilities and limitations in the simulation of photofission process.

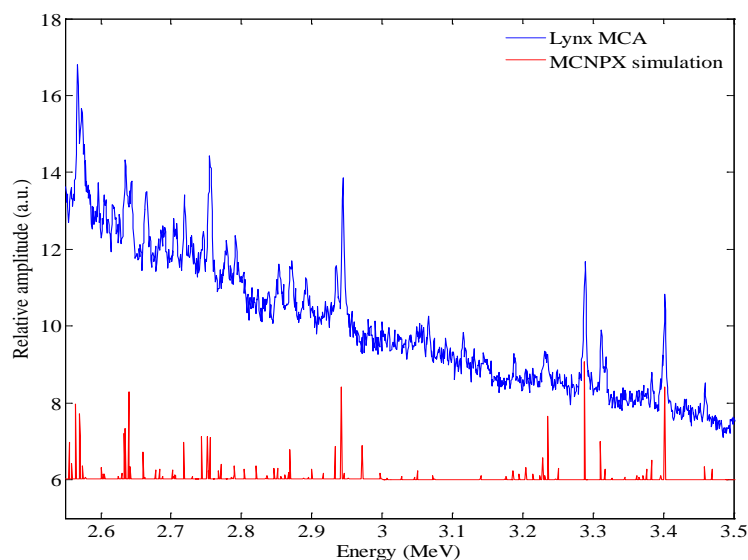


Figure 6.1 Comparison between the measured delayed gamma spectra and simulated results (2.6-3.5 MeV, ^{238}U).

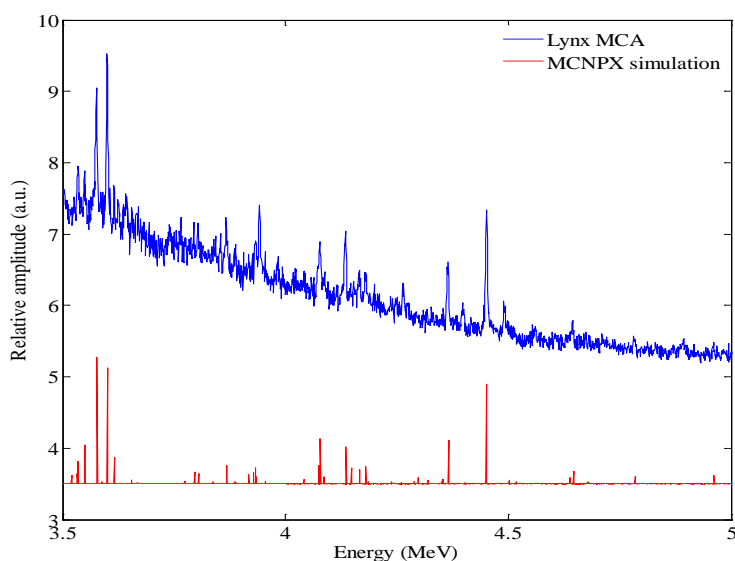


Figure 6.2 Comparison between the measured delayed gamma spectra and simulated results (3.5-5.0 MeV, ^{238}U).

Table 6.1 Efficiency corrected intensities relative to the 3287.6 keV peak.

Isotope	$T_{1/2}$ (seconds)	Energy (keV)	Measured (^{238}U)	Error (%)	Simulated (^{238}U)	Uncertainties (%)
^{95}Sr	23.90	2717.3	0.367	19	0.320	0.6
^{106}Tc	35.6	2789.3	0.585	11	0.165	1.0
^{136}I	83.4	2868.9	0.491	17	0.322	0.7
^{95}Sr	23.9	2933.1	0.375	18	0.282	0.7
^{98}Y	0.548	2941.3	0.997	9	0.784	0.5
^{97}Y	3.75	3287.6	1	6	1	0.4
^{98}Y	0.548	3310.0	0.428	13	0.323	0.6
$^{90\text{m}}\text{Rb}$	258	3317.0	0.213	20	0.088	1.1
^{90}Rb	158	3383.2	0.168	18	0.169	0.8
^{97}Y	3.75	3401.3	0.868	10	0.783	0.5
^{93}Rb	5.84	3458.2	0.170	21	0.113	1.0
^{90}Rb	158	3534.2	0.137	27	0.161	1.0
^{97}Y	3.75	3549.5	0.177	33	0.178	0.8
^{95}Y	618	3576.0	0.491	10	0.576	0.5
^{91}Rb	58.4	3599.7	0.590	10	0.529	0.5

^{93}Rb	5.84	3867.6	0.140	18	0.085	1.1
^{88}Br	16.34	3932.4	0.166	25	0.157	1.2
^{91}Rb	58.4	4078.3	0.235	17	0.206	0.8
^{90}Rb	158	4135.5	0.215	13	0.169	0.8
^{89}Br	4.35	4166.3	0.079	28	0.066	1.3
^{87}Br	55.6	4180.5	0.093	25	0.081	1.2
^{90}Rb	158	4365.9	0.266	13	0.198	0.8
^{98}Y	0.548	4450.2	0.559	9	0.456	0.6

The comparisons between the MCNPX simulation results and the low-energy delayed γ -ray spectra measured from photofission of ^{238}U and ^{239}Pu using the list-mode system and the published delayed γ -ray spectra by P. Sibczynski et al. [1] are shown in Figures 6.3-6.23. It is observed that some peak lines are measured in the measurements, however, they are not predicted by simulation or over-predicted/under-predicted. Also, some lines that are predicted by simulation are not observed in the measurements.

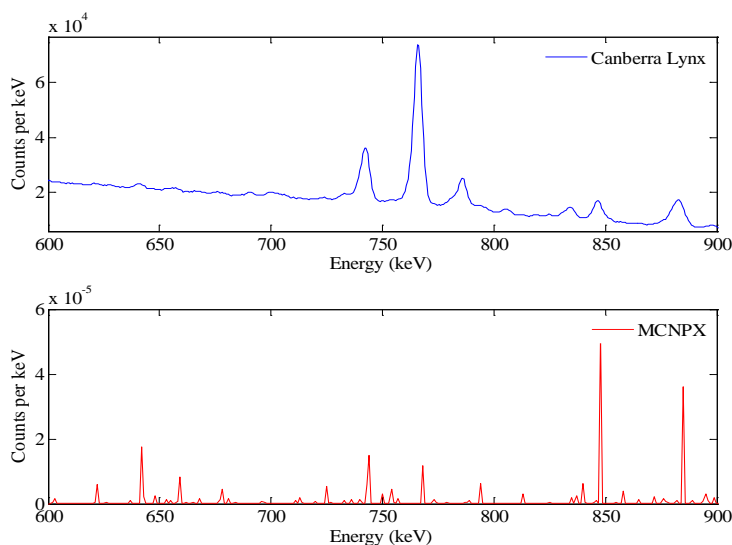


Figure 6.3 Comparison between the delayed γ -ray spectra measured using the list-mode system and simulation results (0.6-0.9 MeV, ^{238}U).

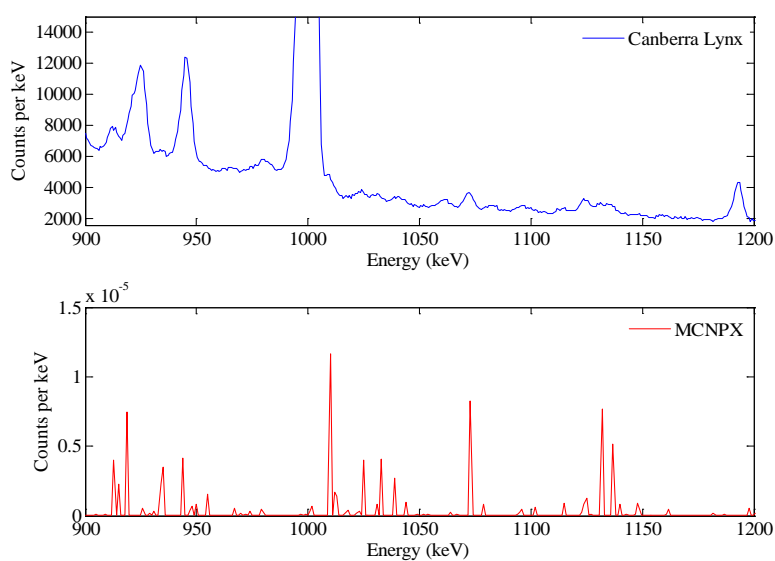


Figure 6.4 Comparison between the delayed γ -ray spectra measured using the list-mode system and simulation results (0.9-1.2 MeV, ^{238}U).

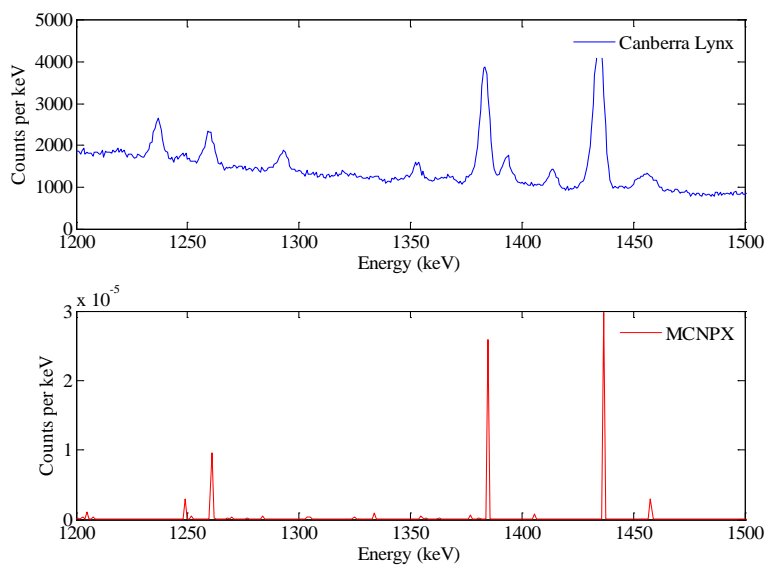


Figure 6.5 Comparison between the delayed γ -ray spectra measured using the list-mode system and simulation results (1.2-1.5 MeV, ^{238}U).

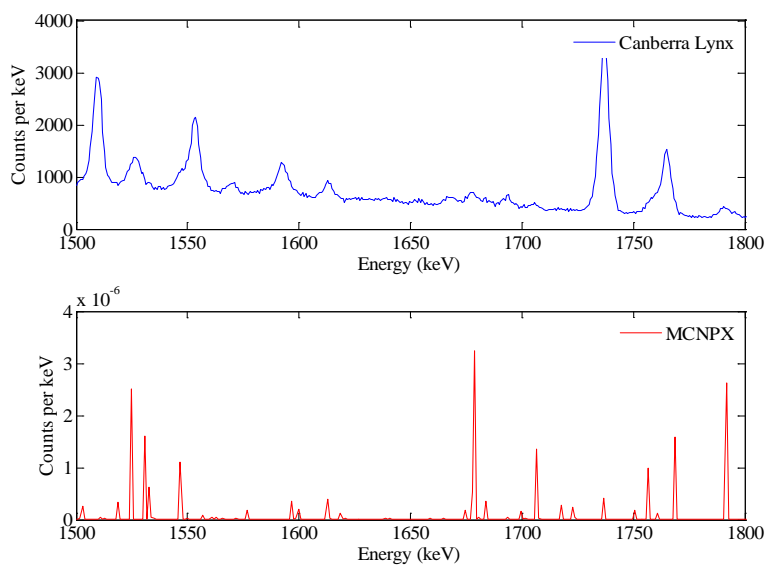


Figure 6.6 Comparison between the delayed γ -ray spectra measured using the list-mode system and simulation results (1.5-1.8 MeV, ^{238}U).

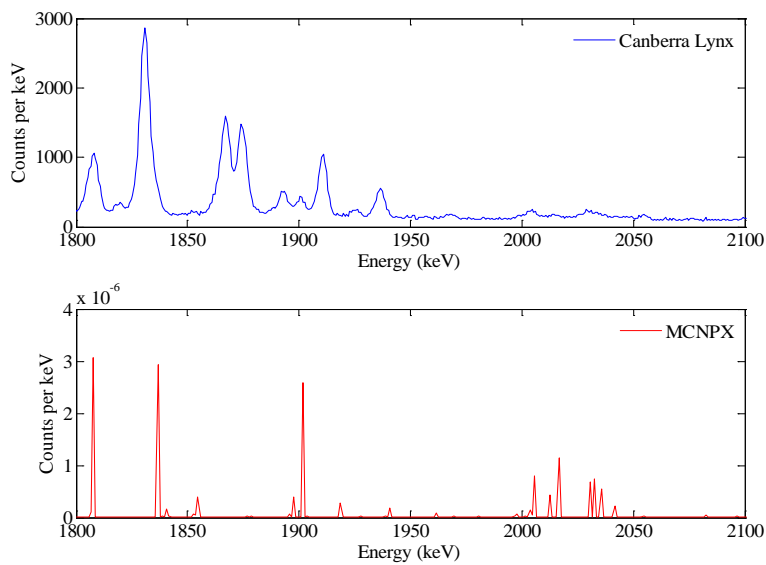


Figure 6.7 Comparison between the delayed γ -ray spectra measured using the list-mode system and simulation results (1.8-2.1 MeV, ^{238}U).

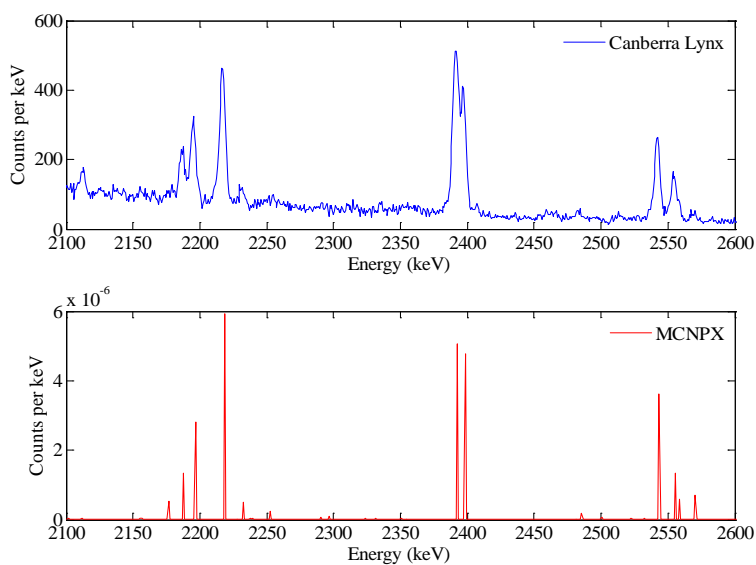


Figure 6.8 Comparison between the delayed γ -ray spectra measured using the list-mode system and simulation results (2.1-2.6 MeV, ^{238}U).

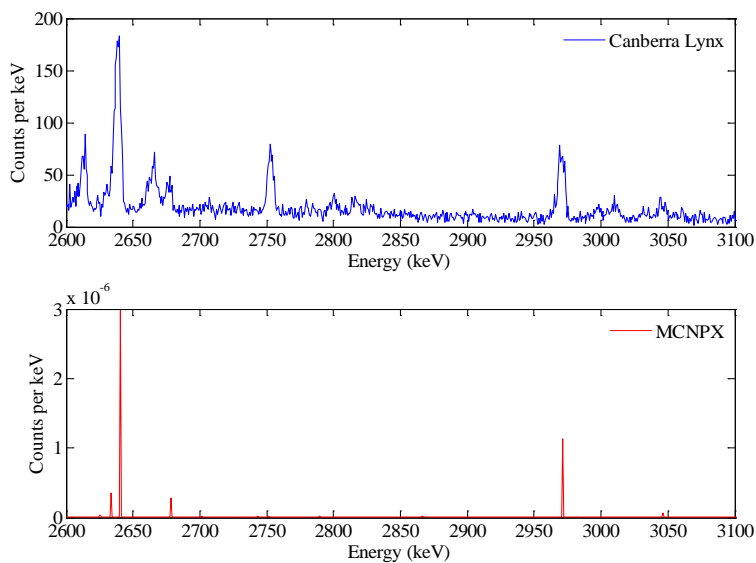


Figure 6.9 Comparison between the delayed γ -ray spectra measured using the list-mode system and simulation results (2.6-3.1 MeV, ^{238}U).

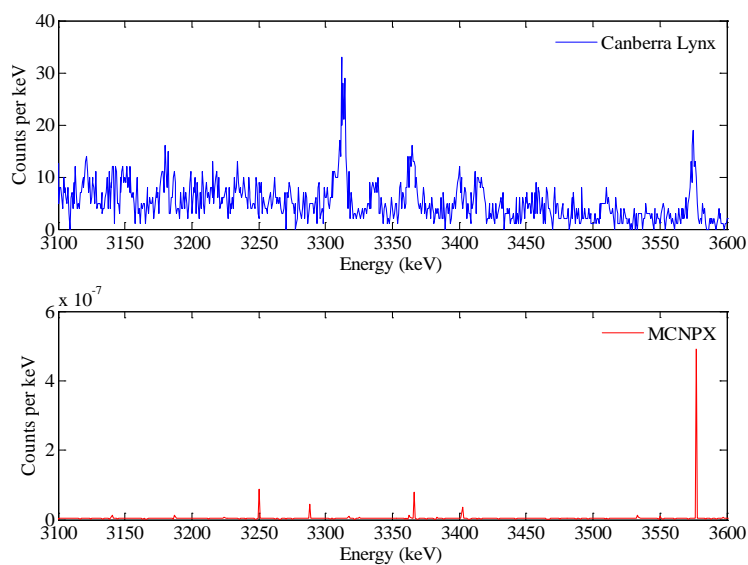


Figure 6.10 Comparison between the delayed γ -ray spectra measured using the list-mode system and simulation results (3.1-3.6 MeV, ^{238}U).

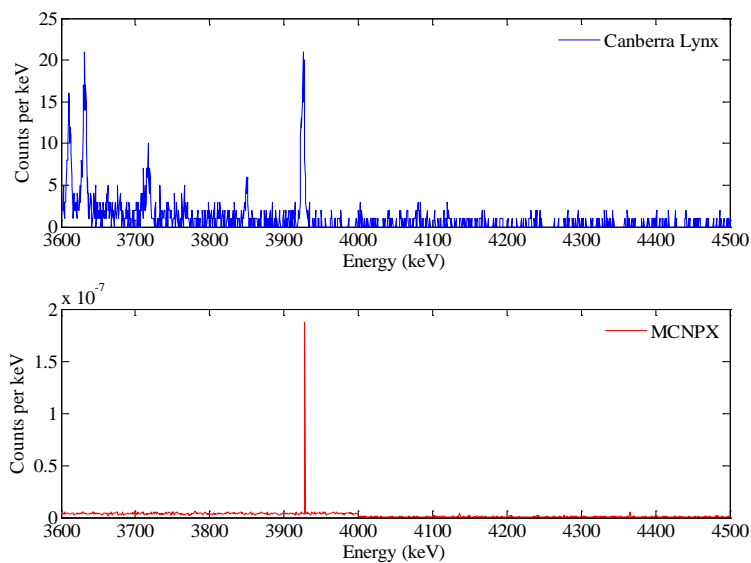


Figure 6.11 Comparison between the delayed γ -ray spectra measured using the list-mode system and simulation results (3.6-4.5 MeV, ^{238}U).

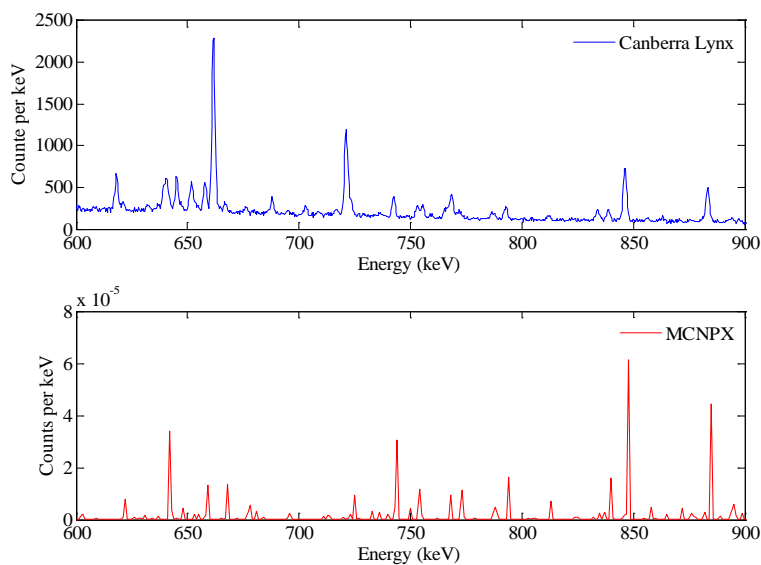


Figure 6.12 Comparison between the delayed γ -ray spectra measured using the list-mode system and simulation results (0.6-0.9 MeV, ^{239}Pu).

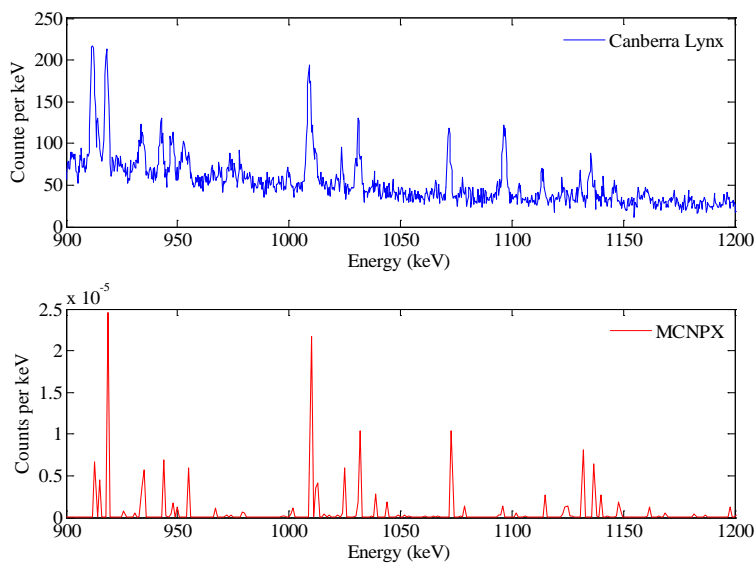


Figure 6.13 Comparison between the delayed γ -ray spectra measured using the list-mode system and simulation results (0.9-1.2 MeV, ^{239}Pu).

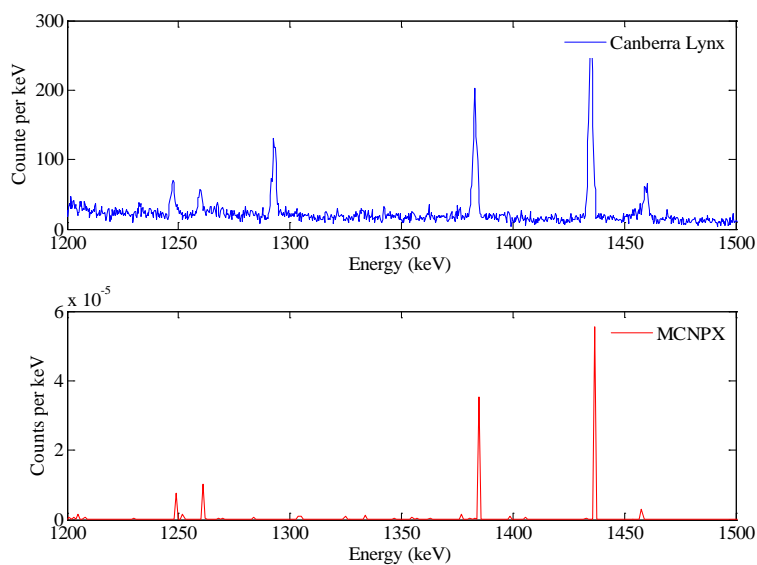


Figure 6.14 Comparison between the delayed γ -ray spectra measured using the list-mode system and simulation results (1.2-1.5 MeV, ^{239}Pu).

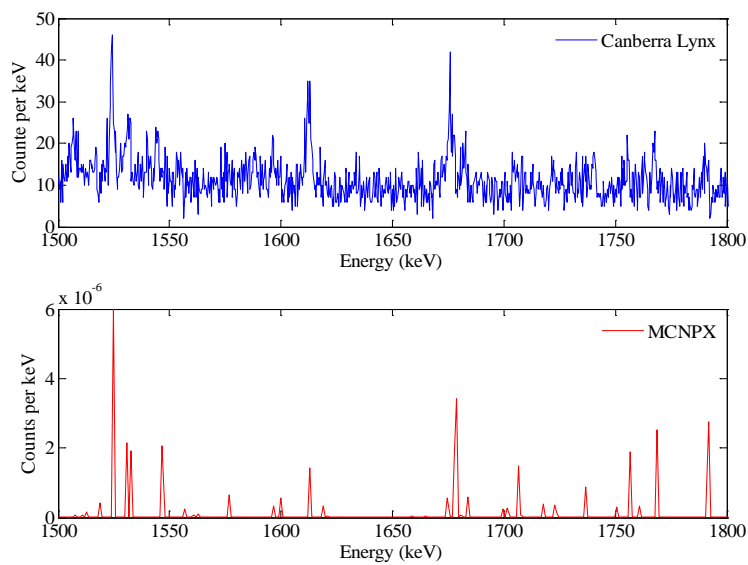


Figure 6.15 Comparison between the delayed γ -ray spectra measured using the list-mode system and simulation results (1.5-1.8 MeV, ^{239}Pu).

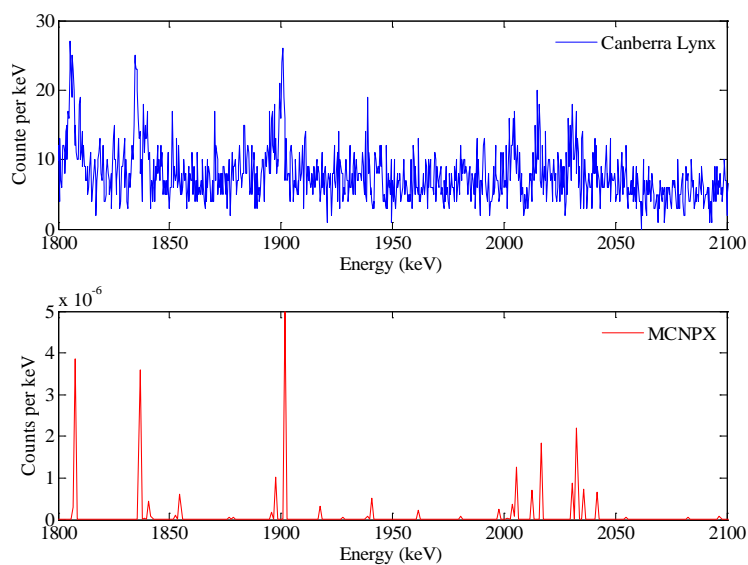


Figure 6.16 Comparison between the delayed γ -ray spectra measured using the list-mode system and simulation results (1.8-2.1 MeV, ^{239}Pu).

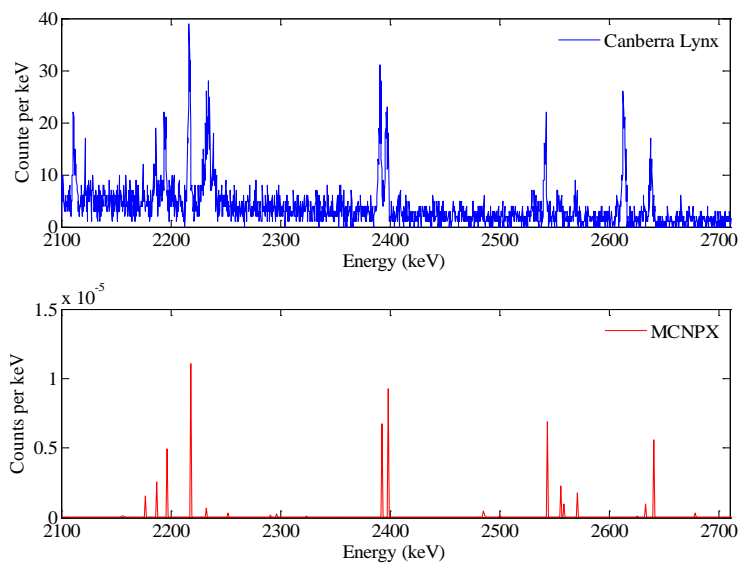


Figure 6.17 Comparison between the delayed γ -ray spectra measured using the list-mode system and simulation results (2.1-2.7 MeV, ^{239}Pu).

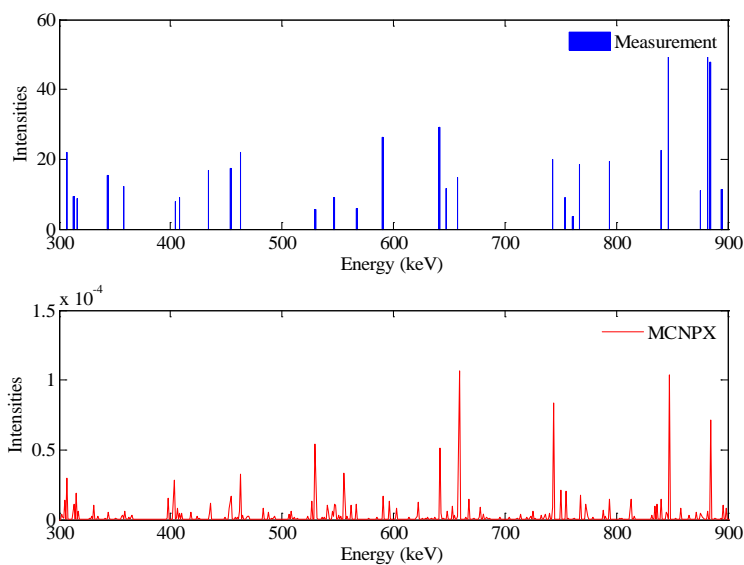


Figure 6.18 Comparison between the delayed γ -ray spectra published by P. Sibczynski et al. and simulation results (0.3-0.9 MeV, HEU).

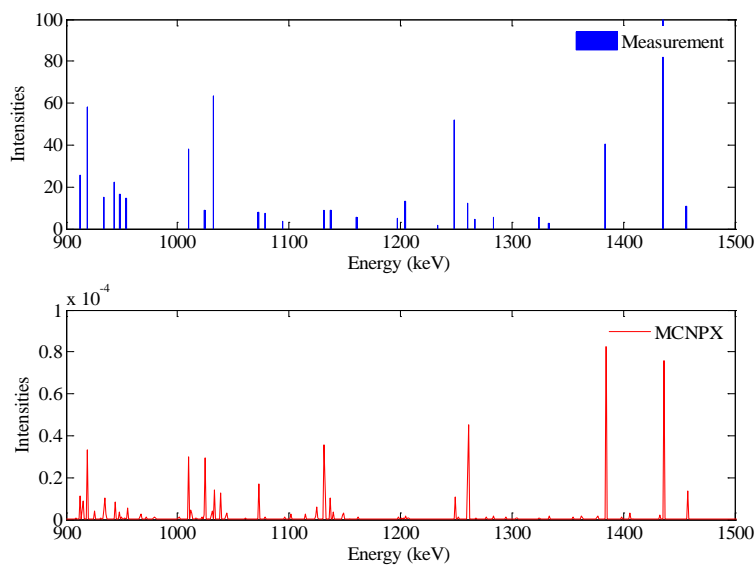


Figure 6.19 Comparison between the delayed γ -ray spectra published by P. Sibczynski et al. and simulation results (0.9-1.5 MeV, HEU).

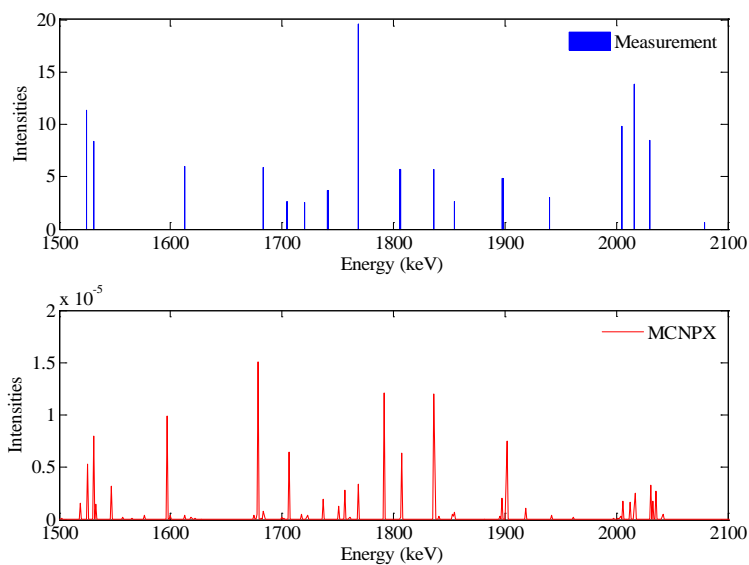


Figure 6.20 Comparison between the delayed γ -ray spectra published by P. Sibczynski et al. and simulation results (1.5-2.1 MeV, HEU).

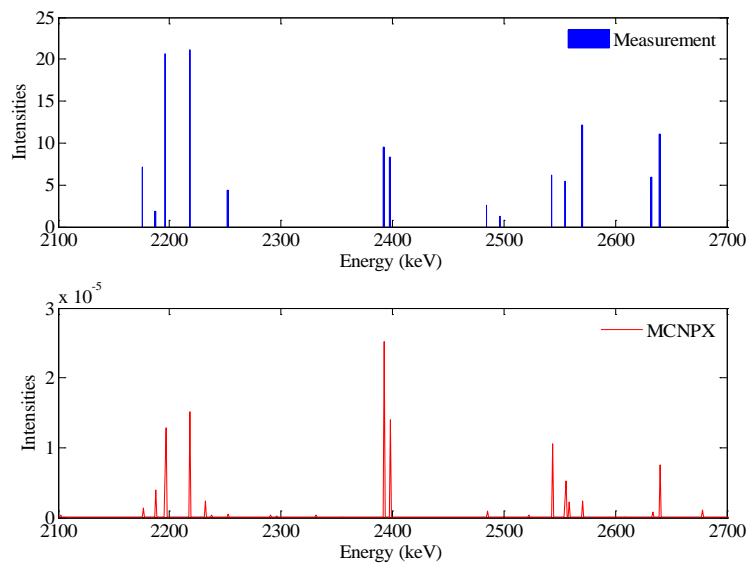


Figure 6.21 Comparison between the delayed γ -ray spectra published by P. Sibczynski et al. and simulation results (2.1-2.7 MeV, HEU).

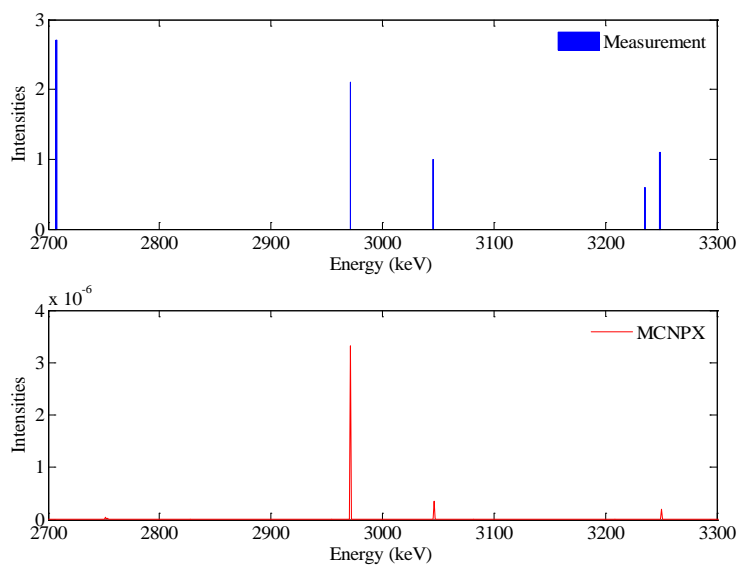


Figure 6.22 Comparison between the delayed γ -ray spectra published by P. Sibczynski et al. and simulation results (2.7-3.3 MeV, HEU).

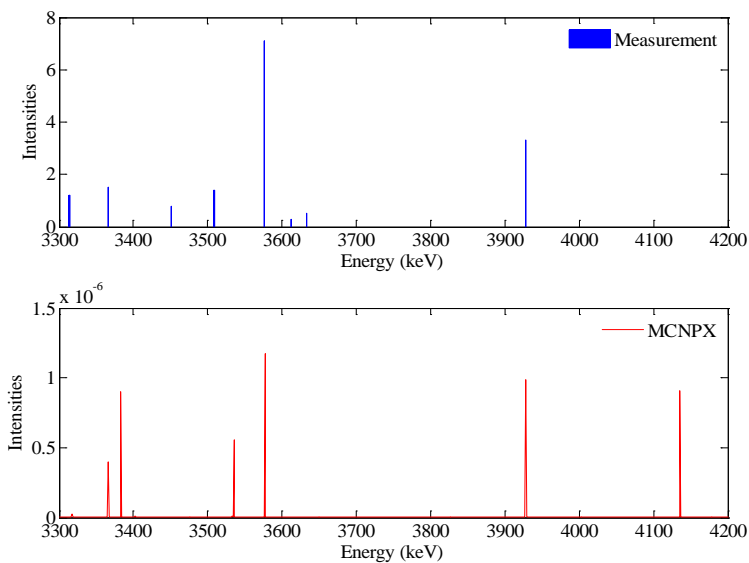


Figure 6.23 Comparison between the delayed γ -ray spectra published by P. Sibczynski et al. and simulation results (3.3-4.2 MeV, HEU).

B De-randomization Technique

1) Deconvolution of HPGe preamplifier pulses

The technique developed by V. Jordanov for deconvolution of pulses from an HPGe preamplifier was used to obtain the current signals [2-3]. A detailed description of the deconvolution method is given below. In common spectroscopy systems the detector-preamplifier configuration is followed by pole-zero cancellation and differentiation circuits. As a result, a pulse with short rise time and exponential tail is produced. The pulse is then amplified to increase signal-to-noise ratio. A block diagram of a typical RC-feedback preamplifier is shown in Figure 6.24. A schematic drawing of the preamplifier is given in Figure 6.25. The configuration can also be present as an ideal current-voltage converter followed by a RC low-pass network, as shown in Figure 6.26. The voltage signal at the output of the current-voltage converter has the same shape as the detector current signal. Therefore, the current signal can be obtained by finding the inverse transfer function of the RC network. In other words, the purpose of the deconvolution is to cancel the effect of the convolution of the current signal with the impulse response of the RC network. In this case, it is obvious that the impulse response of the RC network together with deconvolver should be a delta function. To simplify the derivation of the deconvolution equation the detector current signal is assumed to be a delta function and the amplifiers A1 and A2 are considered ideal elements which do not affect the pulse shape.

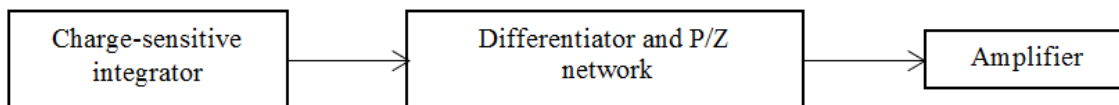


Figure 6.24 A block diagram of the functionality of a typical RC-feedback commercial preamplifier unit.

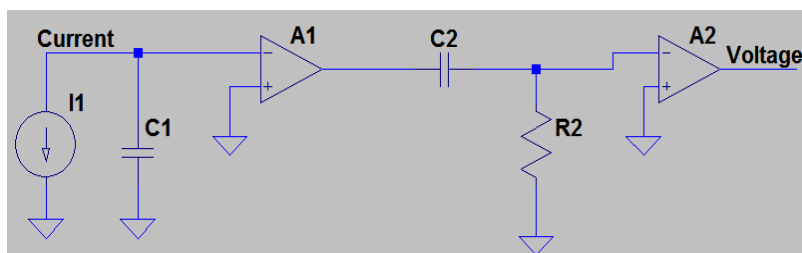


Figure 6.25 A schematic drawing of a preamplifier with RC-feedback.

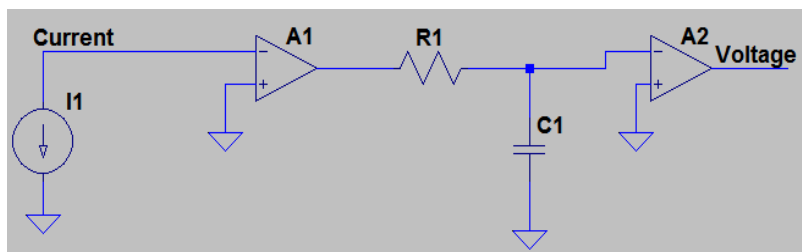


Figure 6.26 An equivalent presentation of the preamplifier.

The impulse response for the capacitor voltage in a RC low-pass network can be found by solving the following differential equation [2]:

$$h_c(t) + \tau \frac{dh_c(t)}{dt} = \delta(t), t \geq 0 \quad (1)$$

The initial condition is $h_c(0) = 0$. Solving the above equation gives $h_c(t) = \frac{1}{\tau} e^{-\frac{t}{\tau}} u(t)$,

where $\tau = RC$ is the time constant of the RC network, $u(t)$ is the step function. Similarly,

the impulse response for the resistor voltage is $h_R(t) = \delta(t) - \frac{1}{\tau} e^{-\frac{t}{\tau}} u(t)$.

The impulse response for the capacitor voltage must satisfy the above equation. Therefore, the relationship between the input and output signals of the desired deconvolver should be expressed as follows:

$$v_{in}(t) + \tau \frac{dv_{in}(t)}{dt} = v_{out}(t) \quad (2)$$

The above equation written in discrete time domain is

$$v_{out}(k) = v_{in}(k) + (v_{in}(k) - v_{in}(k-1)) \times M \quad (3)$$

where k is the sampling point; M is a measure of the decay time constant τ of the preamplifier pulse in the unit of sampling period τ_c ($M = \left(e^{\frac{\tau_c}{\tau}} - 1 \right)^{-1}$). The

deconvolution algorithm can be easily implemented in a digital circuit. The digitized data from a preamplifier is delayed by one clock cycle and stored in a register. The delayed data is subtracted from the prompt data. The result is then multiplied by the equivalent of the decay time constant (i.e. M). Finally, the result of the multiplication is added to the prompt data.

The algorithm was applied to digitized data from a HPGe preamplifier. The preamplifier signal and deconvolved current signal are shown in Figure 6.27. Two major observations can be made from this Figure. First, the signal-to-noise ratio is significantly decreased after the deconvolution because the restoration of the current signal inevitably causes restoration of noise. Second, the deconvolved signal does not exactly match the original current signal due to imperfections of the amplifiers (i.e. A1 and A2). In this case, the deconvolved pulse is a result of the convolution of the current signal with the impulse response of the system which accounts for the imperfections. As shown in Figure 6.27, the signal-to-noise ratio of the deconvolved current signal is greatly increased when passed through the SG filter. The impact of SG filtering on energy resolution is discussed below in detail.

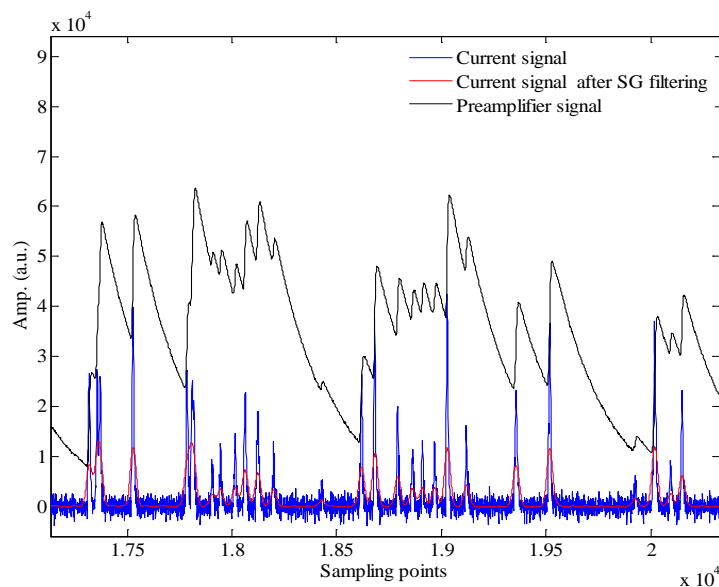


Figure 6.27 The deconvolution of pulses from an HPGe preamplifier.

2) Digital synthesis of exponential signals

The method developed by V. Jordanov to synthesize exponential signals was used here [4]. Exponential signals in discrete time domain are defined as follows:

$$y(n) = \begin{cases} a^n, n \geq 0 \\ 0, otherwise \end{cases} \quad (4)$$

Where a is a constant, n is sampling point. All samples $y(n)$ have constant values if a is equal to 0 or 1. $y(n)$ is a decaying exponential signal if a is greater than 0 but less than 1. If a is greater than 1, $y(n)$ is a growing exponential signal. If a is less than 0, $y(n)$ alternates between positive and negative numbers. For the signal from an HPGe preamplifier, a is greater than 0 but less than 1.

From the equation (4), the ratio of two consecutive values of an exponential signal can be expressed as follows:

$$\frac{y(n+1)}{y(n)} = \frac{a^{n+1}}{a^n} = a, n \geq 0 \quad (5)$$

Using the equation (5), a recursive form for an exponential signal can be expressed as

$$y(n+1) = y(n) \times a \quad (6)$$

The initial condition for the equation (6) is

$$y(n) = 1 \text{ for } n = 0, \quad y(n) = 0 \text{ for } n < 0.$$

The purpose of the exponential signal synthesis is to find a linear time-invariant recursive system which generates an exponential signal in response to an input signal $x(n)$. The recursive form for the system can be present as

$$y(n+1) = y(n) \times a + x(n) \quad (7)$$

From the equation (7), the impulse response of the recursive system is

$$h(n) = h(n-1) \times a + \delta(n), n \geq 0 \quad (8)$$

It is obvious from the equation (8) that the impulse response is an exponential signal, which grows or decays in time depending on the constant a . Figure 6.28 shows the synthesized exponential pulses from the detector current signals using the equation (7). The energy signal shaped from the synthesized pulses using the trapezoidal filter is also shown in Figure 6.28.

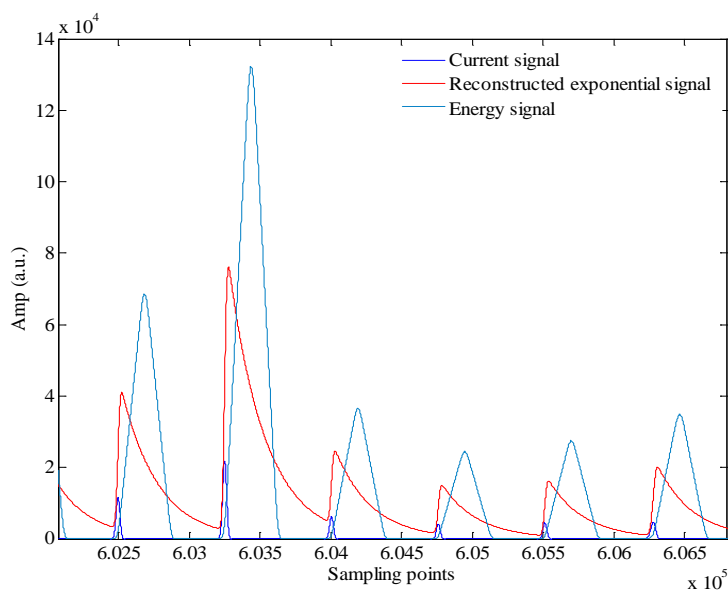


Figure 6.28 Digital synthesis of exponential pulses from the detector current signals.

The recursive algorithm can be easily implemented in digital circuit. It only requires three functional blocks: a delay/register, a multiplier and an adder. The output signal is

delayed by one clock unit and then multiplied by the constant a . The multiplication result is added to the input signal to produce next output signal. The recursive system will produce exponential signals that are either growing or decaying depending on the constant a in response to a unit impulse $\delta(n)$. The growth and decay rates are determined by the magnitude of the multiplication coefficient which is the exponential base of the produced exponential signal. Because the detector current signal is not a delta function, the output signals from the recursive system have a short rise time, as shown in Figure 6.28.

3) Effect of deconvolution and synthesis on energy resolution

It was observed that only small discrepancy exist between the reconstructed exponential pulses and the preamplifier signals. To study the possible impact of the deconvolution and synthesis on energy resolution, the reconstructed pulses were shaped to obtain the energy information using the traditional trapezoidal filtering approach. In the trapezoidal filtering, there were two channels shaped in parallel, i.e. energy and time channels. The energy signal was shaped with a long shaping time to perform energy measurement. The time signal shaped with shorter shaping time was used to detect the time-of-arrival of each event and perform pile-up rejection. If a pulse arrives within $2*L+K$ (L: rise time, K: flat top time) after the previous pulse, both pulse will be rejected to have an energy spectrum with good energy resolution.

To reduce the impact of ballistic deficit on energy resolution, the flat top of the trapezoidal filter needs to be longer than the charge collection time. To find the appropriate flat top time empirically, the charge collection time for each event was first estimated using the recursive algorithm for digital pulse shaping [3]. The above deconvolution method could also be used to make an estimation of the charge collection time. Due to large noise was restored in the deconvolution, a large threshold was required to avoid possible false trigger. Compared to the pulse shaping method to find the charge collection time, the deconvolution method is easy to implement in digital circuit and the resource utilization is small. The disadvantage is that pulses with amplitude comparable to noise level may not be triggered. The small pulses were then not used to obtain the collection time. After obtaining the information about the charge collection time, various rise times in the slow channel for energy measurement were used to find the optimal rise time. Once the optimal shaping time was obtained, the traditional trapezoidal filtering method was used to reconstruct energy spectra and then compare the energy resolutions achieved from shaping the original and reconstructed pulses. It was observed that there was only slight degradation in energy resolution because of the deconvolution of the preamplifier pulses and the synthesis of exponential signals (i.e. 2.3 keV vs 2.5 keV @ 662 keV, the input count rate was 100 kcps).

4) Impact of noise on energy resolution

In the energy spectrum reconstruction from the synthesized exponential pulses, no data was added to the detector current and noise signal. It was found that the assumption that

the noise restored from the deconvolution is not correlated is not correct. When the background noise was used to de-randomize the current signals, very large degradation in energy resolution was observed. This resolution will be even worse at higher input count rate. To overcome this challenge the SG filter was first used to process the deconvolved current signal. As shown in Figure 6.28, the signal-to-noise was significantly improved and the peak location remains after the SG filtering. One disadvantage is that the pulse time domain increases because the SG filtering doesn't change the peak area but reduces the peak amplitude. However, the time is still much smaller compared to normal shaping time used in the traditional trapezoidal filtering (i.e. a few hundred nanoseconds vs ~ten microseconds). This means the pile-up is only limited by the charge collection time. In this case, the throughput rate could be greatly improved, especially at ultra-high count rate.

5) Implementation of the technique on HPGe data

The major steps used in this technique are described here in detail. First, the deconvolution method (Equation 3) is used to obtain the detector current signals from the preamplifier pulses. Because the restoration of the current signal will inevitably cause restoration of noise and it was found that the way to de-randomize the current signal by adding the background noise will significantly affect energy resolution, the SG filter is used to smooth the deconvolved signals before de-randomization. The SG filtering can be easily implemented in Matlab using the function *sgolayfilt(x,k,f)*, where k is the polynomial order, f is the frame size. In this work, the parameters k and f were set at 1

and 9, respectively. The next step is the de-randomization process that is the key to greatly improve throughput rate using this technique.

The basic idea of the de-randomization is that the time interval between the two successive current signals must be equal or large than the $2*L+K$ after the de-randomization, where K and L are the shaping parameters in the traditional trapezoidal filtering. After the de-randomization, the current signals are then used to synthesize exponential pulses using the recursive Equation (7). The last step is to obtain the energy information of each pulse from the exponential signals using the traditional trapezoidal filtering method. The rise time and flat top time in the trapezoidal filtering were set at 9 μs and 0.8 μs , respectively. No pile-up rejection or recovery techniques were used here.

Figures 6.29 and 6.30 show the reconstructed energy spectra from the high-rate HPGe data. The energy resolution was 2.5 keV at 662 keV at input count rate of 100 kcps. The output count rate was also 100 kcps because no pulse was rejected. The result means that throughput rate can be significantly improved without large sacrifice in energy resolution. The algorithm was also applied to the 300 kcps HPGe data. Only slight degradation in energy resolution was observed (i.e. 3.1 keV vs 2.5 keV @ 662 keV). However, pile-up events can also be seen from the Figure 6.30. The pile-up phenomenon occurs only when gamma interacts with the detector within the charge collection process of previous event. Statistical signal processing will be one potential way to recover the pile-up events.

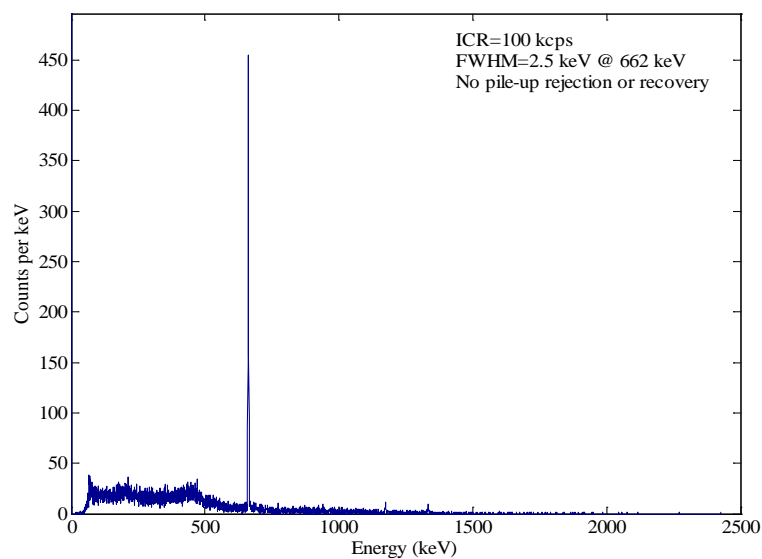


Figure 6.29 Energy spectrum reconstructed using the algorithm based on the de-randomization method (ICR=100 kcps).

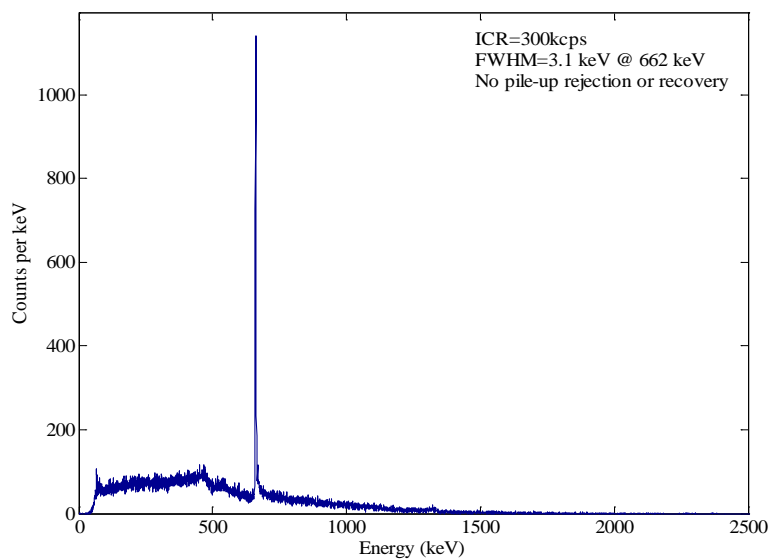


Figure 6.30 Energy spectrum reconstructed using the de-randomization method (ICR=300 kcps).

References

1. P. Sibczynski, et al., "Decay chains and photofission investigation based on nuclear spectroscopy of highly enriched uranium sample," *Applied Radiation and Isotopes*, vol. 82, pp. 170-174, 2013.
2. V. Jordanov, "Deconvolution of pulses from a detector-amplifier configuration," *Nucl. Instr. and Meth. A*, vol. 351, pp. 592-594, 1994.
3. V. Jordanov, "Digital pulse de-randomization for radiation spectroscopy," patent No.: US 6,369,393 B1, 2002.
4. V. Jordanov, "Exponential signal synthesis in digital pulse processing," *Nucl. Instr. and Meth. A*, vol. 670, pp. 18-24, 2012.

C Monte Carlo Simulation Codes

The MCNPX code used in the simulation of delayed γ -rays from photofission of ^{239}Pu .

c Delayed gamma

1 1 -19.8 -1

2 0 1 -2

3 0 2

1 so 0.01

2 so 0.02

mode n p

imp:n 1 1 0

imp:p 1 1 0

m1 94239 -94.7 94240 -5.3

```
phys:p 3j 1 j -102
phys:n 3j -101
act fission=all nonfiss=none dn=model dg=lines
sdef par=p tme=(d11<d22) erg=d3
si11 0 400 1e7
sp11 0 1 0
si22 0 4.14e11
sp22 0 1
si3 a 4.70 5.11 5.52 5.94 6.35 6.76 7.17 &
      7.58 8.0 8.41 8.82 9.23 9.64 10.05 10.47 &
      10.88 11.29 11.70 12.11 12.52 12.94 13.35 &
      13.76 14.17 14.58 15.0 15.41 15.82 16.23 &
      16.64 17.05 17.47 17.88 18.29 18.70 19.11 &
      19.52 19.94 20.35 20.76 21.17 21.58 22.0
sp3 0.0477 0.0411 0.0382 &
      0.033 0.0272 0.024 0.0264 0.0257 0.0207 &
      0.0176 0.0175 0.0165 0.0131 0.015 0.0084 &
      0.012 0.0109 0.0077 0.0071 0.0091 0.009 &
      0.0077 0.0074 0.0064 0.0057 0.0043 0.0039 &
      0.004 0.0041 0.0038 0.0035 0.0018 0.0022 &
      0.0033 0.0012 0.0016 0.0011 0.0017 0.00079 &
      0.001 0.0004 0.0 0.00019
```

```
lca 7j -2
fl:p 1
e1 0.6 4400i 5
t1 5.04e11 1.044e12
ft1 tag 1
fu1 94000.99999
cut:p 1.044e12 0.6
cut:n 1.044e12
nps 1e8
```

The MCNPX code used in the simulation of delayed γ -rays from photofission of ^{238}U .

```
c Delayed gamma
```

```
1 1 -19.1 -1
```

```
2 0 1 -2
```

```
3 0 2
```

```
1 so 0.01
```

```
2 so 0.02
```

```
mode n p
```

```
imp:n 1 1 0
```

```
imp:p 1 1 0
```

```
m1 92238 1
phys:p 3j 1 j -102
phys:n 3j -101
act fission=all nonfiss=none dn=model dg=lines
sdef par=p tme=(d11<d22) erg=d3
si11 0 400 6.6667e6
sp11 0 1 0
si22 0 7.200036e11
sp22 0 1
si3 a 4.70 5.11 5.52 5.94 6.35 6.76 7.17 &
      7.58 8.0 8.41 8.82 9.23 9.64 10.05 10.47 &
      10.88 11.29 11.70 12.11 12.52 12.94 13.35 &
      13.76 14.17 14.58 15.0 15.41 15.82 16.23 &
      16.64 17.05 17.47 17.88 18.29 18.70 19.11 &
      19.52 19.94 20.35 20.76 21.17 21.58 22.0
sp3 0.0477 0.0411 0.0382 &
      0.033 0.0272 0.024 0.0264 0.0257 0.0207 &
      0.0176 0.0175 0.0165 0.0131 0.015 0.0084 &
      0.012 0.0109 0.0077 0.0071 0.0091 0.009 &
      0.0077 0.0074 0.0064 0.0057 0.0043 0.0039 &
      0.004 0.0041 0.0038 0.0035 0.0018 0.0022 &
      0.0033 0.0012 0.0016 0.0011 0.0017 0.00079 &
```

0.001 0.0004 0.0 0.00019

lca 7j -2

f1:p 1

e1 0.6 3900i 4.5

t1 8.1e11 1.89e12

ft1 tag 1

fu1 92238.99999

cut:p 1.89e12 0.6

cut:n 1.89e12

nps 1e8

The MCNPX code used in the simulation of delayed γ -rays from photofission of HEU.

c Delayed gamma

1 1 -19.1 -1

2 0 1 -2

3 0 2

1 so 0.01

2 so 0.02

mode n p

imp:n 1 1 0

imp:p 1 1 0

m1 92235 93 92238 7

phys:p 3j 1 j -102

phys:n 3j -101

act fission=all nonfiss=none dn=model dg=lines

sdef par=p tme=(d11<d22) erg=d3

si11 0 500 2e6

sp11 0 1 0

si22 0 6e10

sp22 0 1

si3 a 4.84 5.12 5.39 5.66 5.94 6.22 6.49 6.76 &

7.04 7.31 7.59 7.86 8.14 8.41 8.69 &

8.96 9.24 9.51 9.78 10.05 10.33 10.61 &

10.88 11.16 11.43 11.71 11.98 12.26 12.53 &

12.80 13.08 13.35 13.62 13.90 14.17 14.45 &

14.73 15.0

sp3 1.828 1.758 1.487 1.350 1.251 1.155 1.037 0.977 &

0.902 0.813 0.720 0.678 0.666 0.587 0.537 &

0.489 0.458 0.393 0.358 0.328 0.358 0.309 &

0.280 0.266 0.204 0.212 0.190 0.172 0.129 &

0.122 0.091 0.082 0.071 0.05 0.034 0.028 &

0.007 0.006

lca 7j -2

fl:p 1

e1 0.3 3900i 4.2

t1 2.4e11 8.88e12

ft1 tag 1

fu1 92000.99999

cut:p 8.88e12 0.3

cut:n 8.88e12

nps 1e8

D Publications and Presentations

Publications

1. Xianfei Wen, Haori Yang, "Photofission product yields of ^{238}U and ^{239}Pu with 22-MeV bremsstrahlung," *Nucl. Instr. Meth. Phys. Res. A*, 2016 (in revision).
2. Xianfei Wen, Dante Nakazawa, Mat Kastner, Jason Pavlick, Haori Yang, "Evaluation of a modified HPGe preamplifier for high-rate spectroscopy measurements in a pulsed photonuclear environment," *Nucl. Tech.*, vol. 194, 2016.
3. Xianfei Wen, Haori Yang, "Study on a digital pulse processing algorithm based on template-matching for high-throughput spectroscopy," *Nucl. Instr. Meth. Phys. Res. A*, vol. 784, pp. 269-273, 2015.
4. Xianfei Wen, John Kavouras, Dante Nakazawa, Haori Yang, "Simulation and measurement of delayed γ -rays after photon-induced fission," *Nucl. Instr. Meth. Phys. Res. A*, vol. 729, pp. 781-787, 2013.
5. John Kavouras, Xianfei Wen, Daren Norman, Dante Nakazawa, Haori Yang, "Pulsed photofission delayed gamma ray detection for nuclear material identification," *IEEE Nuclear Science Symposium Conference Record*, N1-35, 2012.

Presentations

1. Xianfei Wen, Dante Nakazawa, Haori Yang, "Simulation and measurement of cumulative photofission yields of ^{238}U and ^{239}Pu ," *IEEE Nuclear Science Symposium and Medical Imaging Conference*, San Diego, California, 2015.
2. Xianfei Wen, "Measurement and simulation of delayed γ -rays from photofission," *invited talk*, Dartmouth College, Hanover, New Hampshire, 2015.
3. Xianfei Wen, Haori Yang, "Active interrogation technique based on photofission for used nuclear fuel assay," *Oregon State University Engineering Research Expo*, Portland, Oregon, 2015.
4. Xianfei Wen, Dante Nakazawa, Mat Kastner, Haori Yang, "A high-throughput high-resolution gamma spectroscopy system for the measurement of delayed γ -rays after photon-induced fission," *IEEE Nuclear Science Symposium and Medical Imaging Conference*, Seattle, Washington, 2014.
5. Xianfei Wen, Dante Nakazawa, Haori Yang, "Study on a digital pulse processing algorithm based on template-matching for high-throughput spectroscopy," *Symposium on Radiation Measurements and Applications*, Ann Arbor, Michigan, 2014.
6. Xianfei Wen, John Kavouras, Haori Yang, "Active interrogation techniques for special nuclear material detection," *CANBERRA Users' Group Meeting*, Salt Lake City, Utah, 2013.
7. Haori Yang, John Kavouras, Xianfei Wen, Dante Nakazawa, Daren Norman, "Pulsed photofission delayed gamma ray detection for nuclear material identification," *IEEE Nuclear Science Symposium and Medical Imaging Conference*, Anaheim, California, 2012.
8. Can Liao, Xianfei Wen, Haori Yang, "Neutron energy spectrum correction based on capture time," *AIChE Annual Meeting*, Pittsburgh, Pennsylvania, 2012.